Universität Hamburg
DER FORSCHUNG | DER LEHRE | DER BILDUNG

MASTER'S THESIS

Investigation of a pre-stressed concrete structure using passive image interferometry

Franziska Mehrkens

Supervisors:
Prof. Dr. Céline Hadziioannou
PD Dr. rer. nat. Ernst Niederleithinger

University of Hamburg
Institute of Geophysics
February 2020

Investigation of a pre-stressed concrete structure using passive image interferometry

Abstract

Prestressed concrete structures like bridges lose their initial prestress over time. The aim of the thesis is to find out if passive image interferometry is suitable to detect damage in these structures created by prestress reductions.
A measurement was carried out on a prestressed concrete structure with a built-in pretensioning system. While the prestressing force was reduced step wise, 23 geophones measured the ambient noise field. The results of the experiment showed a maximum decrease in seismic velocity by -7.81%. When a prestress of 203 kN was reached, the velocity did not further decrease. This behavior could be an indicator for a state of the structure where it should not be loaded further in order to prevent its collapse. Because the structure's eigenfrequencies had to be used for the investigation, a velocity bias must be removed. For further studies it is suggested to avoid using those frequencies due to their strong variation.
Overall, it was possible to monitor the prestress changes and the subsequent formation of cracks by using the passive image interferometry and in particular the stretching method.

In addition to the velocity change due to damage, environmental influences like temperature deviations can also lead to velocity variation. This effect has to be reduced when the aim is to examine the structural health of a structure. For that reason, another part of the thesis is to estimate a velocity variation rate per degree Centigrade.
The determined velocity variation rate is between $-0.134\,\frac{\%}{°C}$ and $-0.087\,\frac{\%}{°C}$. While the first value was estimated for the entire period of two months, the second one included just four weeks after a reattachment of the sensors. The temperature and velocity data showed a low correlation due to several factors. These includes distance and differences in thermal diffusion, for example. Nevertheless, the values fit to other studies carried out before on other concrete structures.

Contents

List of Figures v

List of Tables viii

1 Introduction 1

2 Theory 3
2.1 Seismic interferometry . . . 3
2.2 Passive image interferometry . . . 4
2.3 Stretching method . . . 6

3 Measurement setup 9
3.1 BLEIB structure . . . 9
3.2 Setup & instruments . . . 12
3.3 Data acquisition . . . 12

4 Release of prestressing force - passive data 17
4.1 Spectral analysis . . . 17
4.2 Preprocessing . . . 19
4.3 Cross-correlation . . . 21
4.4 Frequency bands . . . 22
4.5 Stretching method . . . 23
4.5.1 Time window length estimation . . . 25
4.6 Results . . . 26

5 Release of prestressing force - active data 31
5.1 Raw data . . . 31
5.2 Processing . . . 34

6 Influence of temperature 37
6.1 Processing of data . . . 37
6.2 Results . . . 38
6.3 Temperature reduction . . . 39

7 Discussion 43
7.1 Comparison between active and passive results . . . 43
7.2 Synthetic test . . . 44
7.3 Removal of the velocity bias . . . 47
7.4 Comparison of temperature results with previous studies . . . 50

8 Conclusion and outlook 53

Appendices 54

A Measurement schedule 19th of March 2019 55

B Natural frequency trend **56**

C Time windows used for stretching method **57**

D Stretching results of the long term measurements **62**

Bibliography **63**

Acknowledgments **67**

List of Figures

2.1 Basic 1D example for seismic interferometry. a) Locations of source and receivers. b) Record at receiver x_A. c) Record at receiver x_B. d) Cross-correlation of record b) and c) which represents the Green's function. [adapted from Wapenaar et al. [2010]] 3

2.2 Isotropic noise source distribution with resulting cross-correlation function. The cross-correlation function shows time-symmetric peaks on the causal as well as on the acausal part. [adapted from Wapenaar et al. [2010]] 5

2.3 Principle of the stretching method. An original signal (black curve) is stretched (blue curve) and compressed (red curve) by a factor ε to find the best fit to a reference signal. 7

3.1 BLEIB reference structure which was used as the measurement object. [adapted from Mierschke [2018]] 9

3.2 Geometry of the structure (scale 1:100). 10

3.3 Cross-section in the middle of the structure (scale 1:5). 11

3.4 Anchorage of the steel bars (scale 1:5). 11

3.5 Measurement setup (left) and used 4.5 Hz-geophones (right). 12

3.6 Sketch of the measurement setup. The red triangles indicate the locations of the geophones, the blue triangle indicates the position where the hammer-blow was performed. 13

3.7 Temperature data in Baruth. One data set (blue curve) was measured in a height of 2 m, the other one (black curve) was measured in a depth of 5 cm. Both data sets were correlated with the velocity changes in order to find the most suitable one for further processing. 15

4.1 Spectrogram of a raw signal recorded at the beginning of the experiment. a) Whole frequency range, b) spectrogram zoomed in between $0 - 30$ Hz. Most of the energy can be found below 25 Hz. 17

4.2 Amplitude spectrum of a raw signal recorded at the beginning of the experiment. a) Whole frequency range, b) spectrum zoomed in between $0 - 30$ Hz. Three significant peaks can be seen which indicate the eigenfrequencies of the structure. 18

4.3 Trend of the first natural frequency lying around 3.8 Hz. While the prestress was reduced, the natural frequency moved towards lower values. . . 19

4.4 Amplitude spectrum of a noise record filtered between 1 - 25 Hz. All of the three eigenfrequencies can still be identified. 20

4.5 Signal a) before and b) after the one-bit normalization. The explosion on the neighboring testing field is marked by the red box. After the normalization was applied, it cannot be identified anymore. 21

4.6 Example of a cross-correlation function. Receiver 4 was cross-correlated with receiver 8. The signal decreased to a stable noise level. 22

4.7 CCFs between receiver 4 and 8 for a prestressing force of 462 kN and 1 kN. a) Waveform, b) amplitude spectrum. The waveforms are clearly different due to the strong variation of the included frequency content. . . 23

4.8 Investigated frequency bands from receiver 3 and 23 for a prestressing force of 462 kN. All of the functions show a maximum in the causal part which can be related to the position of the strongest noise source. 24
4.9 Window size estimation. Here, the stretching method was applied on the CCF between sensor 4 and 8 measured at a prestressing force of 300 kN. The frequency band from $4.5 - 8$ Hz was used. The cross-correlation coefficient as well as the relative velocity change varied strongly due to cycle skipping. 27
4.10 Estimated time windows for all frequency bands. The red lines indicate the start and end times exemplary shown for the signal at 462 kN for the receiver pair 4/8. 28
4.11 Results of the applied stretching method on the passive noise measurements. The relative velocity change is shown as well as the cross correlation-coefficients for all three frequency bands. In general, the velocity decreased when the prestressing force was reduced. 30
4.12 Relative velocity change and cross-correlation coefficients along the structure with an inter distance of 2 m between the receivers ($1 - 4.5$ Hz). A decrease in velocity change can be seen at the middle pillar's position. . . 30
5.1 Time-distance plot of a hammer blow induced raw signal for a prestressing force of 462 kN. When comparing the waveform, differences between the records for some sensors can be found. 32
5.2 a) Spectrogram and b) amplitude spectrum of a hammer blow induced raw signal for a prestressing force of 462 kN. The hammer blow can be clearly identified at a time of 24 s. 33
5.3 Example of a cross-correlation function estimated from active measurements. Receiver 4 was cross-correlated with receiver 8. The function clearly decreased to a stable noise level. 34
5.4 Results of the applied stretching method on the active measurements. The relative velocity change is shown as well as the cross correlation-coefficients for all three frequency bands. In general, the same trend as for the passive measurements can be seen. 35
6.1 Travel time variations and belonging cross-correlation coefficients (1-4.5 Hz). Two periods (27/03 - 01/04 and 24/04 - 27/04) with low cross-correlation coefficients can be identified. 38
6.2 Drop of the cross-correlation coefficients (1-4.5 Hz). A connection with the precipitation (blue curve, measured in Baruth) is conceivable. 39
6.3 Travel time variations $\frac{dt}{t}$ for frequencies between 1 and 4.5 Hz and the soil temperatures measured in Baruth. These data sets were used to determine a mean velocity variation rate per degree Centigrade. 41
6.4 Results of the reduction of the temperature effect using the frequency band from 1 to 4.5 Hz and the soil temperatures measured in Baruth. a) Calculated residuals, b) Comparison of the travel time variations before and after the reduction, c) Result of the linear regression (red curve). . . . 42
7.1 Comparison of the stretching results using passive measurements (dashed lines) and active measurements (solid lines). The order of magnitude is the same for all frequency bands. 44

7.2 Standard deviation of the stretching results estimated by using the passive noise measurements. The lowest frequency band shows the smallest deviations. 45
7.3 Stretching results of the passive measurements when using a threshold CC>0.7. The course of the frequency band from 4.5 to 8 Hz approached the lower band. 45
7.4 Stretching results of the synthetic test, representing a prestress reduction. The original signal was compared with the shifted one but showing velocity changes (blue curve). The original signal was also compared with the signal that was both shifted and stretched, giving an apparent velocity change (green curve). These values did not match the actual velocity changes (red curve). 46
7.5 Removal of the bias. The actual velocity changes (red curve) are approximated by subtracting the relative frequency changes $\frac{df}{f}$ from the apparent velocity changes (solid black curve). 48
7.6 Corrected stretching results by subtracting the relative frequency shift. The general course did not change whereby the values are clearly higher. . 48
7.7 Standard deviation of the stretching results after the bias removal. The higher frequencies still shows the largest deviations, while the lowest frequency band is the most stable one. 49
7.8 Relative velocity change along the structure after the bias removal. The pillar's location can be easily identified. Both structure halves behave similar. 50
7.9 Temporal variations of the first eigenfrequency. After the reattachment on the 27th of April, the eigenfrequency stays more stable. 52
B.1 Trend of the second natural frequency at 6.05 Hz (left) and the third natural frequency at 15.5 Hz (right) with decreasing prestressing force. 56
D.1 Travel time variations and belonging cross-correlation coefficients (4.5 − 8 Hz). 62
D.2 Travel time variations and belonging cross-correlation coefficients (12 − 16 Hz). 62

List of Tables

3.1 Material properties of the structure's components. 11
4.1 Variation of the natural frequencies. All of them strongly decreased when reducing the prestressing force. 18
4.2 Relative velocity changes and belonging cross-correlation coefficients of the passive measurements. All frequency bands showed the same trend. . 29
6.1 Correlation between the particular frequency bands and the temperature data sets. 41
6.2 Results of the reduction of the temperature effect using time intervals of one week. The chosen frequencies were between 1 and 4.5 Hz while the temperature was measured in 5 cm depth. 41
7.1 Corrected stretching results by subtracting three quarters of the relative frequency shift. The correlation coefficients are slightly higher because a threshold of $CC > 0.7$ was used. Because of the bias removal, the velocity changes are clearly higher compared to the apparent velocities before. . . 49
A.1 Measurement schedule on the 19th of March 2019. 55
C.1 Used time windows for the stretching method. 57

1 Introduction

Bridges are an essential part of every country's infrastructure. According to statistics published by the Federal Highway Research Institute (BaSt) in 2019, around 70% of bridges on federal highways in Germany are made of prestressed concrete [BaSt, September 2019].
Prestressed concrete is characterized by the fact that steel is embedded in concrete. The steel is tensioned and attached to the ends of the bridge before the concrete has set. When this anchorage is released, it exerts a compressible force on the concrete. This acting force leads to a significant reduction of tensile stresses. They can be caused by external loads such as cars crossing the bridge. The advantage of prestressed concrete is that the steel prevents the concrete from cracking despite its low tensile strength.
However, the applied prestress reduces over time since shrinkage and creep can occur [Rajagoplan, 2003]. While the bridge is still exposed to external loads, flexural cracks may begin to form. These do not necessarily have to be visible but they destabilize the structure [Sritharan and Fenwick, 1995].
Structural health monitoring (SHM) aims to detect those damages in all kinds of structures in an automated and effective way. Therefore, structures are permanently observed by attaching sensors to it. These should continuously record the dynamic response of the structure. This response shall be used to detect changes in the structural properties [Fassois and Kopsaftopoulos, 2013].
Because the formation of cracks also affects the seismic velocity inside the structure, seismological methods can be adapted for SHM. Studies have shown before that coda wave interferometry represents a suitable tool to detect relative velocity changes (e.g. Larose et al. [2006]). Due to its dependency on active sources like hammer-blow surveys or induced vibrations, the method of passive image interferometry was invented. Here, ambient seismic noise which can be permanently recorded, serves as source [Liu et al., 2010].

Most of the investigated concrete structures are exposed to environmental conditions such as temperature variations, rain and solar radiation. Accordingly, changes in the seismic velocity cannot be directly assigned to damages, e.g. the building of cracks. To detect real damages, influences caused by temperature have to be removed from the estimated velocity changes. This can be done by determining a velocity variation rate per degree [Salvermoser, 2014].

The aim of this thesis is to find out if damages caused by a reduction of prestress can be detected by using the method of passive image interferometry. In order to achieve this, a measurement was carried out on a prestressed concrete structure, similar to a two span bridge.
The investigation can be divided into two parts: First, the prestressing force was reduced stepwise while recording the ambient noise field. Additionally, an active measurement was done to confirm the estimated velocity changes. The second part of the experiment consists of a long term measurement over two months. This data shall be used to estimate the previously mentioned relation between temperature and velocity changes.

The theory on which the investigation is based on is given in chapter 2. The idea of seismic interferometry and passive image interferometry is presented separately. In order to finally determine values for the relative velocity change, the so-called 'Stretching method' was applied.
The following chapter 3 gives information about the measurement object, located on the test site of the Federal Institute for Materials Research and Testing, and the data acquisition. Afterwards, the obtained passive and active recordings were processed in several steps which form the main part of the thesis (see chapter 4 and 5).
Chapter 6 then deals with the processing and the results of the long term data set, estimating a relation between temperature and relative velocity changes.
In the discussion (see chapter 7) the results determined from the active and passive measurements are compared with each other. Due to the variation of the frequency content, a velocity bias had to be removed from the results. Additionally, the estimated velocity variation rate per degree is examined for correctness using other relations from previous studies.
The thesis ends with an overall conclusion to determine whether the stated aim was achieved or not (chapter 8). Lastly, a brief outlook is provided on additional related areas to this research topic that would be worth investigating further.

2 Theory

2.1 Seismic interferometry

The Green's function is fundamental in seismology. It includes all information of a medium that the seismic waves travel through [Shearer, 2009].
Wapenaar et al. [2010] showed that it is possible to retrieve the Green's function between two seismic stations by cross-correlating their signals. This technique is called 'seismic interferometry' or 'Green's' function retrieval'. The following explanation of the underlying theory is based on his given derivation.
Assume an impulsive source located at position x_S emitting a plane wave and two receivers at positions x_A and x_B which record the rightward propagating signal. The one-dimensional setup can be seen in Fig. 2.1 a). At this point it is important to mention that both ray paths have the distance between x_S and x_A in common. Later on, this leads to a cancellation of the travel time along this path in the cross-correlation.

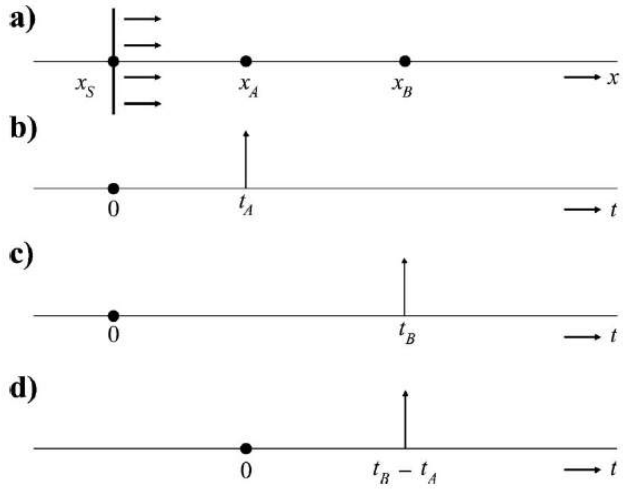

Figure 2.1: Basic 1D example for seismic interferometry. a) Locations of source and receivers. b) Record at receiver x_A. c) Record at receiver x_B. d) Cross-correlation of record b) and c) which represents the Green's function. [adapted from Wapenaar et al. [2010]]

The recorded signal at x_A can be denoted as $G(x_A,x_S,t)$, where G is the Green's function (Fig. 2.1 b)). The first argument in $G(x_A,x_S,t)$ corresponds to the receiver position, the second argument corresponds to the source position. The third argument represents the time t. Accordingly, the record at x_B is given as $G(x_B,x_S,t)$ (Fig. 2.1 c)). Because we are dealing with an impulsive source, the Green's functions are impulses at $t_A = \frac{x_A - x_S}{c}$ and $t_B = \frac{x_B - x_S}{c}$ with a constant propagation velocity c in a lossless medium. Therefore, they can be written as $G(x_A,x_S,t) = \delta(t - t_A)$ and $G(x_B,x_S,t) = \delta(t - t_B)$, respectively.
This relation can be used for the cross-correlation of the signals:

$$
\begin{aligned}
G(x_B,x_S,t) * G(x_A,x_S,-t) &= \int G(x_B,x_S,t+t')\, G(x_A,x_S,t')\, dt' \\
&= \int \delta(t+t'-t_B)\, \delta(t'-t_A)\, dt' \\
&= \delta(t-(t_B-t_A)) \\
&= \delta(t-\frac{x_B-x_A}{c}) \\
&= G(x_B,x_A,t)
\end{aligned}
\tag{1}
$$

The resulting Green's function $G(x_B,x_A,t)$ can be interpreted as a signal recorded at position x_B as if there was a source located at x_A. In conclusion, a virtual source has been created. Neither the source position x_S nor the velocity c need to be known. The cross-correlation is mapped in Fig. 2.1 d). It is an impulse at $t = t_B - t_A$.
The theory holds true for any source function. Because of this, the source does not need to be an impulse. If a noise source is considered at position x_S the equation

$$G(x_B,x_S,t) * G(x_A,x_S,-t) = G(x_B,x_A,t) \tag{2}$$

changes to

$$u(x_B,x_S,t) * u(x_A,x_S,-t) = G(x_B,x_A,t) * S_N(t) \tag{3}$$

, where $u(x_A,x_S,-t)$ is the record at x_A, $u(x_B,x_S,t)$ is the record at x_B and $S_N(t)$ is the autocorrelation of the noise. The cross-correlation contains a maximum at time t which is equal to the travel time between the receivers. By dividing the distance between the receivers by t it is possible to determine the propagation velocity c.

According to Wapenaar et al. [2010], one condition to retrieve the Green's function in actual field measurements is an isotropic source distribution around the receivers (Fig. 2.2). Additionally, the sources have to be uncorrelated. If that is the case, a cross-correlation leads to a time-symmetric response like the one on the right-hand side in Fig. 2.2. Since the sources are now not only on the left side, a clear peak can be identified in both the causal and the acausal part. The thicker dashed lines indicate the Fresnel zones. Only sources within these zones contribute to the resulting cross-correlation function due to their finite-frequency content. Signals that are emitted from noise sources outside the Fresnel zones interfere destructively.

2.2 Passive image interferometry

The passive image interferometry (PII) is a method based on coda wave interferometry (CWI). It applies the technique of CWI on ambient noise cross-correlation functions [Liu et al., 2010]. The main idea behind it is to find weak changes in the elastic properties of a medium by using coda waves. These are going to be compared before and after a perturbation happened at the place of interest [Snieder, 2006].

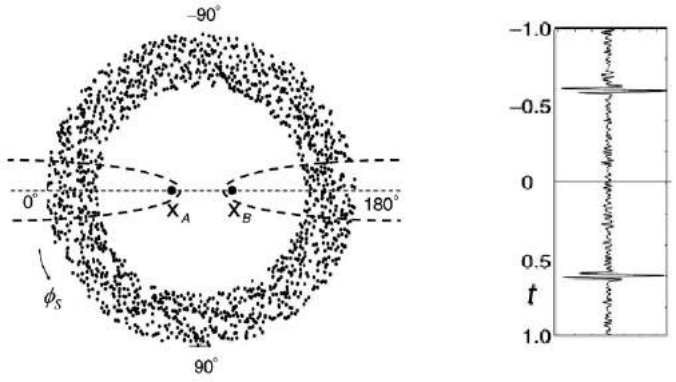

Figure 2.2: Isotropic noise source distribution with resulting cross-correlation function. The cross-correlation function shows time-symmetric peaks on the causal as well as on the acausal part. [adapted from Wapenaar et al. [2010]]

The so-called 'coda' is the part of a seismogram after the direct waves have arrived. Coda waves can be interpreted as a superposition of waves that are randomly scattered on heterogeneities [Herraiz and Espinosa, 1987]. Due to this, coda waves are predestined for CWI. Instead of just traveling directly through a medium they scan it multiple times. Therefore, they are highly sensitive to small changes in the elastic properties. These changes can arise, for example, from temperature influences or long-term exposure. Because they are too small, they cannot be seen by differences in the direct arrival times. Coda waves accumulate velocity changes on their way, making them visible [Snieder, 2006].

The properties of coda waves were first used by Aki and Chouet [1975]. While they took the temporal decay of the coda's amplitude into account, Snieder [2002] developed a new application of coda waves by using their arrival times. He presented the method of CWI:
The coda of a perturbed and an unperturbed wave field is compared by correlation. The maximum correlation coefficient indicates the mean travel time perturbation dt. Based on a spatially homogeneous relative velocity change $\frac{dv}{v}$, a linear relation between dt and the unperturbed travel time t is given [Snieder, 2006]:

$$dt = -t \cdot \frac{dv}{v} \Leftrightarrow -\frac{dt}{t} = \frac{dv}{v} \tag{4}$$

CWI has already been used to keep an eye on volcanoes [Haney et al., 2009] or fault zones [Li et al., 2016] and also for structural health monitoring [Stähler et al., 2011]. A big disadvantage of CWI is the dependence on active sources or the occurrence of earthquakes. The consequence of this is a poor resolution in time and space. Passive image interferometry solves this problem of not being able to continuously monitor the subsurface by using ambient seismic noise [Liu et al., 2010]. For example, changes in seismic velocity over time up to 0.1% have been detected using PII. Therefore, just one or two seismic stations which permanently record are needed [Sens-Schönfelder and Wegler, 2006].

Nevertheless, PII is not flawless. Compared to CWI, the correlation signals are more complex than the coda of active signals [Liu et al., 2010]. To handle this, the records need to be long enough. In addition, the noise field has to be uniformly distributed around the receivers so that the correlation function converges to the impulse response of the medium, the Green's function [Sens-Schönfelder and Wegler, 2006].
However, Hadziioannou et al. [2009] shows that it is possible to apply PII to correlation functions which do not represent the Green's function. Conditions which need to hold are stability of the calculated cross-correlation functions and stability of the noise field.
In order to finally get velocity changes from the previously calculated cross-correlation function, the so-called 'stretching method' is used.

2.3 Stretching method

The stretching method [Sens-Schönfelder and Wegler, 2006], [Lobkis and Weaver, 2003] is generally a technique of PII to estimate small velocity changes in a medium. It is based on the comparison of two different signals by cross-correlating them. Because we are dealing with noise measurements, cross-correlation functions are used. Nevertheless, the term 'signal' is still retained for further explanation.

It is assumed that a signal $h'(t)$ differs from a reference signal $h(t)$ just by dilation. This changed signal can then be described as

$$h'(t) = h(t(1+\varepsilon)) \tag{5}$$

The factor ε is the so-called 'stretching coefficient'. It corresponds to the relative velocity change which is homogeneous in space, so that the following holds:

$$\varepsilon = \frac{dv}{v} = -\frac{dt}{t} \tag{6}$$

With the help of various selected values for ε, the signal $h'(t)$ is compressed and stretched. Figure 2.3 shows this principle exemplary. The black curve shows the unchanged signal. By using equation 5, the original signal is dilated. A negative ε leads to a stretching of the waveform which can be seen by the blue curve. It refers to a negative velocity change, i.e. a decrease in velocity. Conversely, a positive ε leads to a compression (red curve) and consequently refers to an increase in velocity.

Following the compression and stretching, the signals are compared by cross-correlation for their similarity to the reference signal $h(t)$. Therefore, a time window $t \pm \frac{T}{2}$ is chosen.

$$CC(\varepsilon) = \frac{\int_{t-\frac{T}{2}}^{t+\frac{T}{2}} h'(t(1+\varepsilon))\, h(t)\, dt}{\sqrt{\int_{t-\frac{T}{2}}^{t+\frac{T}{2}} h'^2(t(1+\varepsilon))\, dt \cdot \int_{t-\frac{T}{2}}^{t+\frac{T}{2}} h'^2(t)\, dt}} \tag{7}$$

The highest resulting cross-correlation coefficient CC corresponds to the best fit between $h(t)$ and $h'(t)$. The belonging factor ε gives the appropriate relative velocity change in the medium, according to equation 6.

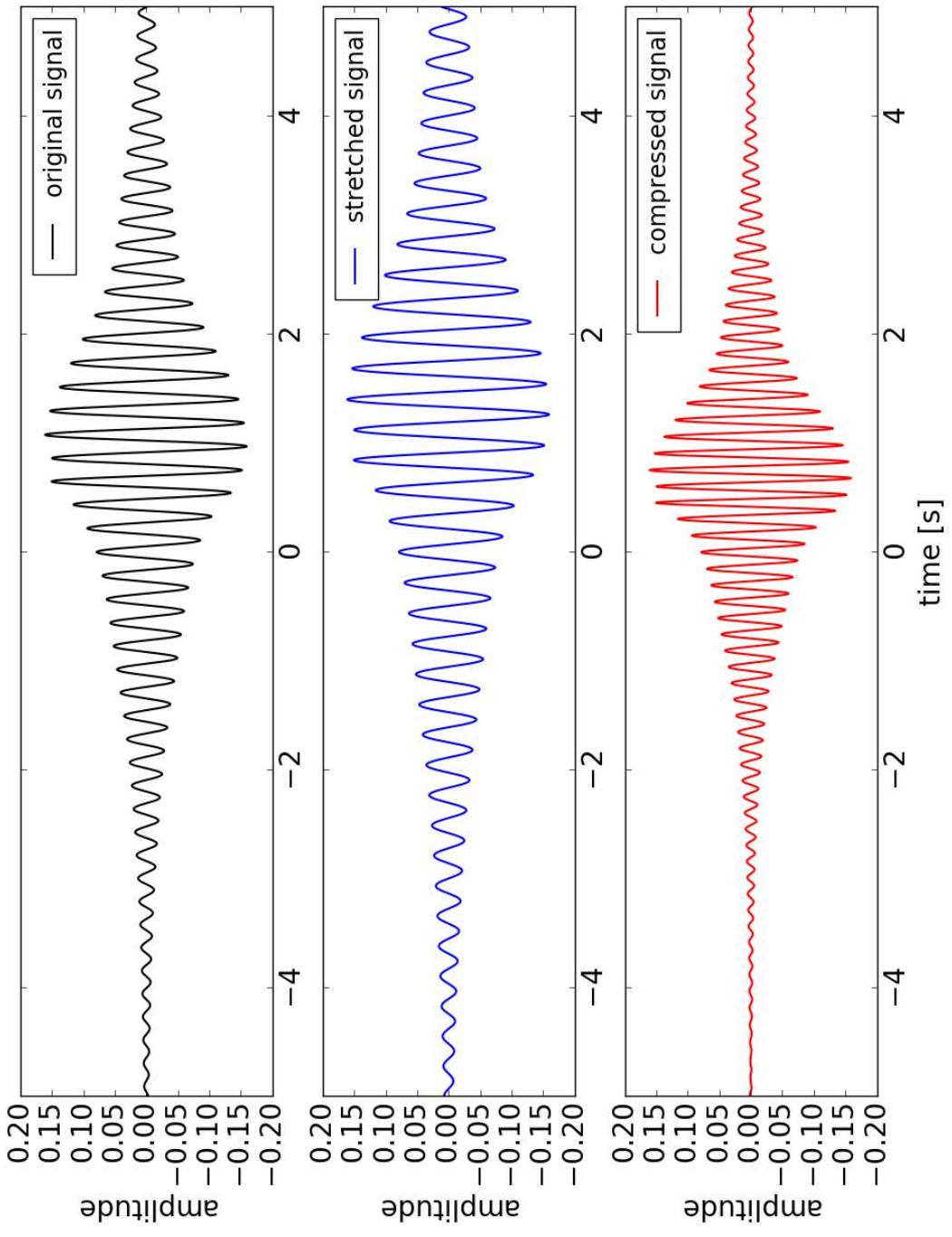

Figure 2.3: Principle of the stretching method. An original signal (black curve) is stretched (blue curve) and compressed (red curve) by a factor ε to find the best fit to a reference signal.

3 Measurement setup

3.1 BLEIB structure

The passive data was recorded in Horstwalde near Berlin, on the test site of the BAM (Federal Institute for Materials Research and Testing). This area hosts the BLEIB reference structure, which serves as the measurement object (Fig. 3.1). It was originally built for the BLEIB project which can be translated as 'assessment, life cycle prognostics and rehabilitation of bridges'.

Figure 3.1: BLEIB reference structure which was used as the measurement object. [adapted from Mierschke [2018]]

In general, the heavily reinforced structure consists of a prestressed concrete beam, lying on three bearings. It corresponds to a two-span bridge (Fig. 3.2). The beam itself is 24.4 m long and 0.9 m wide and its geometrical shape can be described as an inversed 'U'. The cross-section is shown in Fig. 3.3 to get a better impression of the geometry. The superstructure is made out of concrete of the compressive strength class C45/55 with a density of around $2000 - 2600\,\frac{\mathrm{kg}}{\mathrm{m}^3}$ and an elasticity modulus of $36000\,\frac{\mathrm{N}}{\mathrm{mm}^2}$. Other components of the structure such as abutment or piers are made out of concrete of different compressive strength classes. Their material properties can be found in table 3.1.
The structure is particularly suitable for the investigation due to a built-in pre-tensioning system. The prestress is exerted on the beam by two steel bars with a diameter of 7 cm which are located within two casing tubes and anchored at the respective ends (Fig. 3.4). Each can apply a maximum prestressing force of 600 kN. However, the initial state when the measurement started was around 462 kN. By using a hydraulic pump, the prestressing force can be varied.
In addition to the steel bars, different sensors are permanently installed on the inside, although these were not used for the measurement. Two movable loads on top of the beam were also not part of this investigation. Each of them weighs about 2000 kg. They were stored on top of the middle and left pier.
Another important feature of the structure are the existing cracks in the inside. These were intentionally added as part of previous measurements in order to get a damaged medium. In 2018 most of them were vertically aligned, located on the bottom and top of the structure with a crack width of around 0.1 mm to 0.2 mm [Mierschke, 2018].

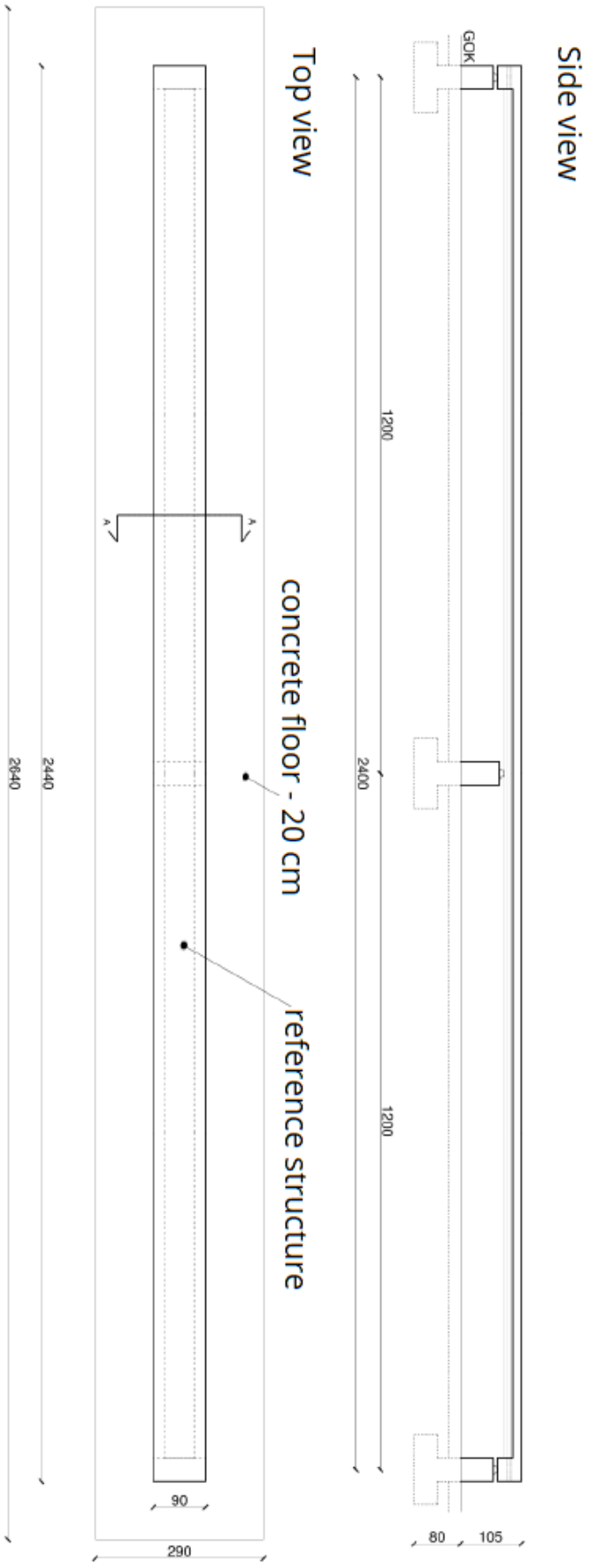

Figure 3.2: Geometry of the structure (scale 1:100).

could add units..

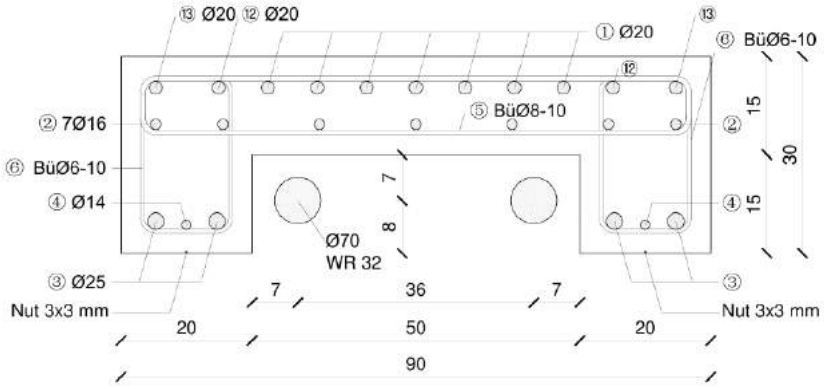

Figure 3.3: Cross-section in the middle of the structure (scale 1:5).

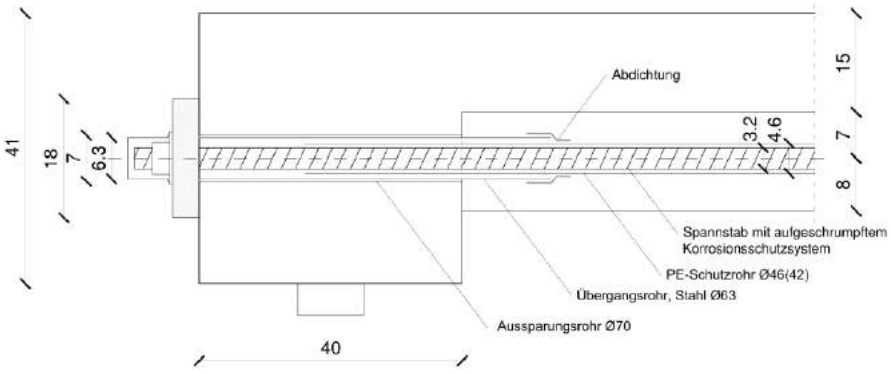

Figure 3.4: Anchorage of the steel bars (scale 1:5).

component	compressive strength class	elasticity modulus E $[\frac{N}{mm^2}]$	exposure classes	max. grain size D	reinforcing steel	prestressing steel
beam	C45/55	36000	XC4, XF3	8	B500B	St 950/1050
abutment	C25/30	31000	XC4,XF1	16	B500B	-
piers	C25/30	31000	XC4,XF1	16	B500B	-
footing	C25/30	31000	XC4,XF1	16	B500B	-
blinding	C8/10	-	X0	32	-	-

Table 3.1: Material properties of the structure's components.

Figure 3.5: Measurement setup (left) and used 4.5 Hz-geophones (right).

3.2 Setup & instruments

The ambient noise field was recorded by 24 vertically oriented geophones with a corner frequency of 4.5 Hz (Fig. 3.5). All of them were linearly attached to the surface of the structure. Since the bridge is located outside, the sensors were also exposed to environmental influences such as wind or rain during the measurement. Therefore, the sensors were fastened with plaster to get a good coupling.
In order to sample the entire beam and be able to spatially assign the results later on, an equal inter-distance of one meter between each geophone was chosen. A sketch of the complete measurement setup can be seen in Fig. 3.6. The red triangles indicate the respective position of the sensors. Because one of the movable loads rested on top of the middle pier, there was a space problem. Due to this, sensor 12 was placed onto the concrete floor. As the waves arriving here cannot provide any information about the medium to be examined, they were not taken into account for further processing.

The records were stored in the SEG-2 format into files with a length of one minute. Because one geophone corresponds to one trace, every file consists of a total of 24 traces. Due to the storage time required by the software, there were small data gaps of 3 to 4 seconds between each file. However, this did not lead to a problem in the following processing.
250 Hz was chosen as the sampling frequency. According to the Nyquist-theorem, this leads to a maximum resolvable frequency of 125 Hz. The resulting frequency range should be sufficient due to the remote location of the structure where wind and low cultural noise are expected as the main sources.

3.3 Data acquisition

The recorded signals can be divided into three different data sets: the passive one, the active one and a long term data set.

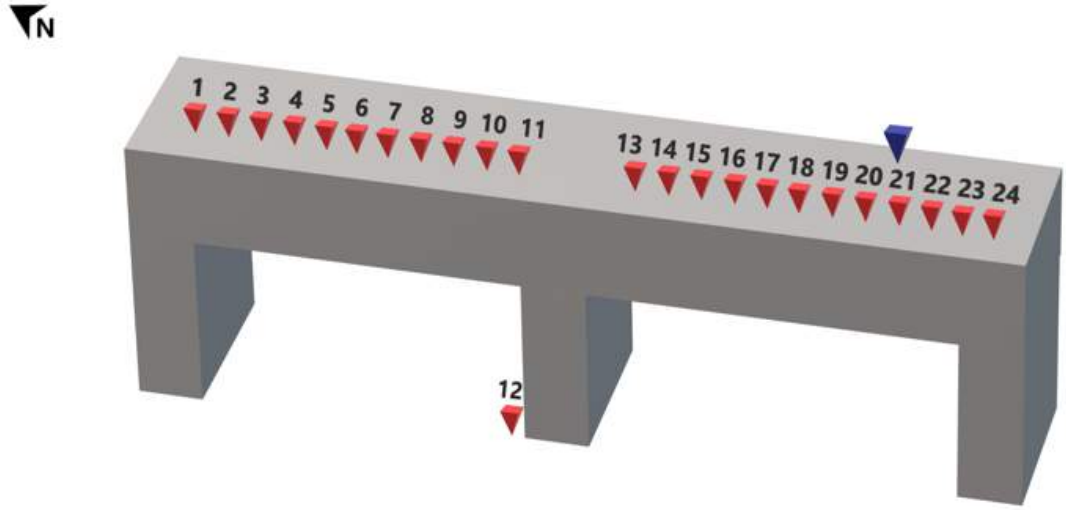

Figure 3.6: Sketch of the measurement setup. The red triangles indicate the locations of the geophones, the blue triangle indicates the position where the hammer-blow was performed.

The ambient noise and the active measurements were carried out on the 19th of March in 2019. They were used to examine the influence of varying prestressing force on the relative velocity change. Therefore, the prestressing force was decreased stepwise. Because the initial prestress was 462 kN for each steel bar, the first reduction was only about 61 kN each. Afterwards, the release was done in steps of around 100 kN. This resulted in the following six considered prestresses: 462 kN, 401 kN, 300 kN, 203 kN, 101 kN and 1 kN. Deviations of approximately ± 1.5 kN could be observed during the individual measurements. These were induced by solar radiation and the resulting thermal expansion of the structure. However, these small deviations should not influence the overall trend of the relative velocity change because of their small size compared to the changing interval.
The ambient noise field was recorded for 20 minutes for each of the six applied prestressing forces, including the initial one. Before reducing the prestress after each measurement, a hammer-blow survey was carried out. This data set was used later on to confirm the results estimated by the passive records.
A hammer was blown ten times onto the bridge between sensor 20 and 21. A pause of one minute was introduced between each blow to let the waves travel unaffected through the medium. The exact source position can be seen in Fig. 3.6. The active signals were measured by using the mounted geophones.
The measurement schedule is provided in appendix A.1, showing the exact timing of each measurement step.

After the end of the measurement and the almost complete release of the prestressing force, it was reset to a value of approximately 454 kN. The sensors were left on site for further two months, measuring the ambient seismic noise from the 19th of March until the 25th of June in 2019. During this time, a long term data set was recorded. It was used to estimate a relation between relative velocity changes in the structure and the air temperature.

As the temperatures were not measured inside the structure, a data set provided from the German weather service (DWD) had to be used. The nearest meteorological station was Baruth which is about nine kilometers from the test site. Absolute air temperatures with a resolution of one hour could be downloaded. They were measured at a height of two metres from the ground. Due to thermal diffusion, temperature takes some time to influence the seismic velocity inside the structure. Therefore, another data set was also downloaded. This one was measured 5 cm below ground. Because the temperature influences the soil only slowly, this data set probably fits better. Both temperature sets were compared with the noise data to find the best correlation and thus, the most appropriate velocity variation rate per degree.
The utilized temperature sets can be seen in Fig. 3.7. Both curves show a daily trend whereas no clear time shift is observable. Generally, the temperatures measured 5 cm below ground are lower than the ones measured at a height of 2 m.

was this determined visually, or with e.g. correlation?

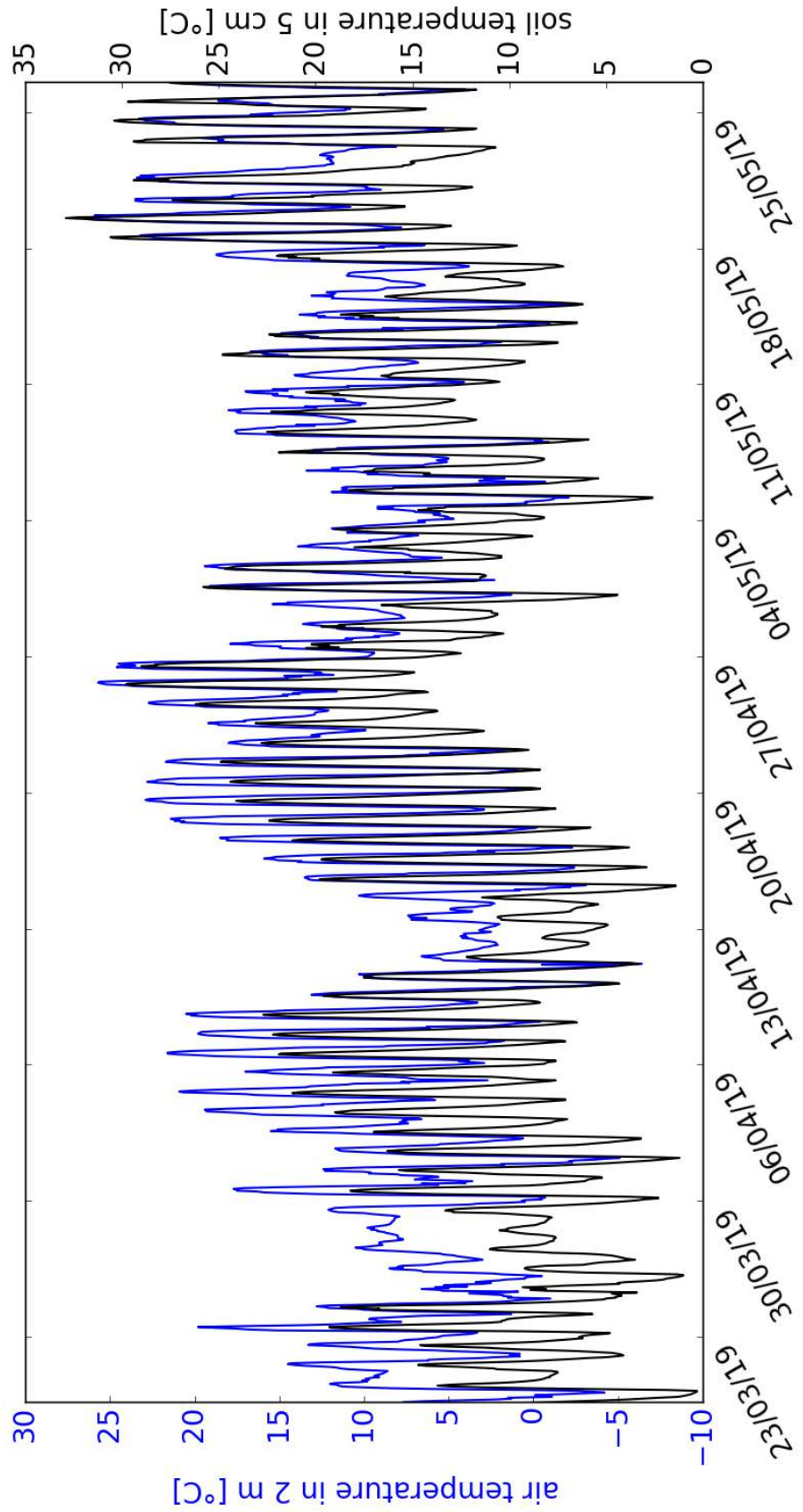

Figure 3.7: Temperature data in Baruth. One data set (blue curve) was measured in a height of 2 m, the other one (black curve) was measured in a depth of 5 cm. Both data sets were correlated with the velocity changes in order to find the most suitable one for further processing.

4 Release of prestressing force - passive data

4.1 Spectral analysis

To get a first impression of the raw signals, their frequency content was analysed. Figure 4.1 a) shows the calculated spectrogram at the beginning of the experiment. In general, the energy decreases with increasing frequency. Most of it lies in a frequency band between 1 and 25 Hz where several continuous peaks are visible. Another distinct horizontal line is striking around 50 Hz which can be attributed to the frequency of the electronic current. To get a better idea of the frequency content the spectrogram was zoomed in between 0 and 30 Hz where high energy could be observed (Fig. 4.1 b)). It shows that three certain frequencies were recorded throughout time indicated by the constant horizontal lines.

To estimate the corresponding frequencies more accurately, the spectrum was calculated (Fig. 4.2 a)). It reveals the same aspects noticed before in the spectrogram (Fig. 4.1 a)). Additionally, all of the three peaks can be seen clearly as local maxima, lying around 4 Hz, 6 Hz and 16 Hz (Fig. 4.2 b)). In a previous study, the first two maxima were identified as the natural frequencies of the structure. There, values of 3.91 Hz and 5.98 Hz are given [Mierschke, 2018]. Due to the stability of the maximum at 15.5 Hz it can be assumed that it is also a higher order eigenfrequency.

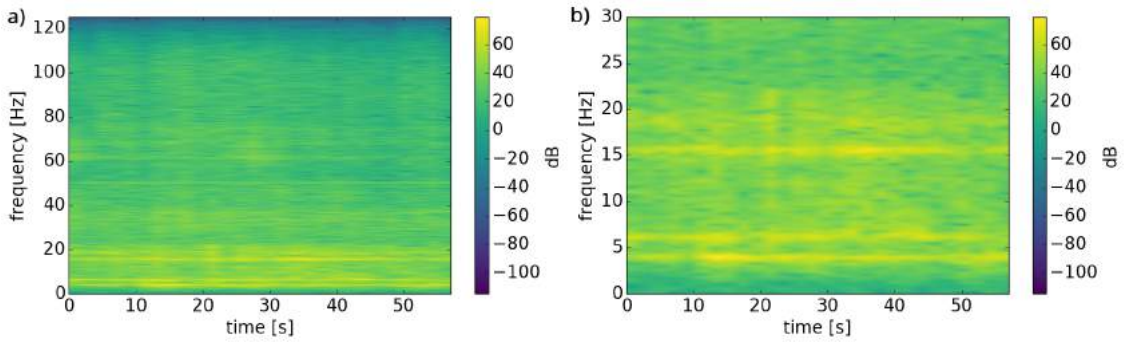

Figure 4.1: Spectrogram of a raw signal recorded at the beginning of the experiment. a) Whole frequency range, b) spectrogram zoomed in between $0 - 30$ Hz. Most of the energy can be found below 25 Hz.

Because the prestressing force was changed to great extent during the experiment the natural frequencies were expected to vary also. By reducing the prestress, the stiffness of the structure also changed which led to a variation in the structure's eigenfrequencies [Al-Ghalib and Mohammad, 2018]. Modal parameters were used before in structural health monitoring to detect damages [Kim et al., 2019].

The behavior of the first eigenfrequency according to the prestress loss can be seen in Fig. 4.3. The temporal evolution of a narrow section of the amplitude spectrum is shown which contains the eigenfrequency to be considered. For every timestep, the spectrum is normalized to its maximum value for reasons of identification. Generally, the eigenfrequency moves towards lower values as the prestressing force is reduced with time.

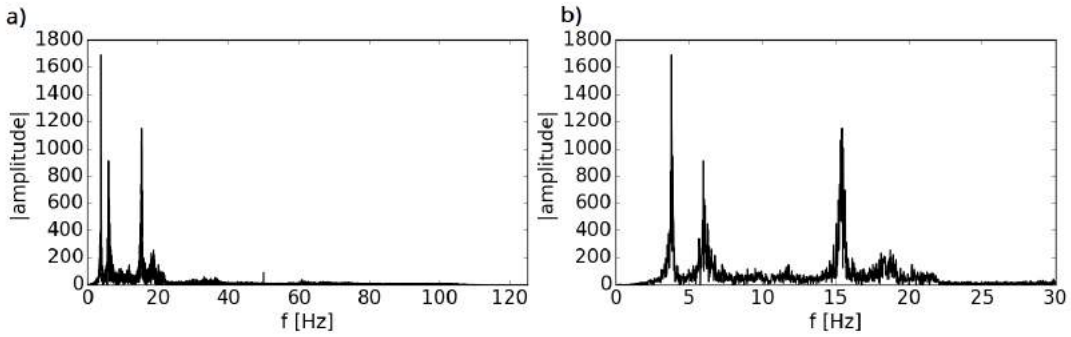

Figure 4.2: Amplitude spectrum of a raw signal recorded at the beginning of the experiment. a) Whole frequency range, b) spectrum zoomed in between $0 - 30\,\text{Hz}$. Three significant peaks can be seen which indicate the eigenfrequencies of the structure.

Starting around 3.8 Hz with a load of 462 kN it ends with a value of 3 Hz. The release of the prestressing force by 461 kN therefore led to a reduction of the considered natural frequency by 0.8 Hz ($\approx 21\,\%$).
The course of the frequency shift is striking. For the first three reductions in the prestressing force it jumps towards lower values. As soon as a prestress of 203 kN is reached, a smooth course can be seen. However, this behavior can be well explained by taking the relation between the natural frequency and the reduction in the structure's stiffness into account. At high prestressing forces (i.e. high stiffness) the curve drops off quickly which cannot be completely resolved due to the selected rate of change ($\approx 100\,\text{kN}$). After using smaller prestressing forces, the curve approaches a certain frequency asymptotically. This observation fits well with a study of Breccolotti [2018] in which the results of several previous studies in this research field are compared.

The eigenfrequencies of higher modes were also investigated, showing the same trend (see appendix B.1). The decrease of the frequencies in detail can be gathered for all modes from table 4.1 which gives the percentage reduction and the associated frequencies.

prestressing force [kN]	first mode		second mode		third mode	
	decrease [%]	frequency [Hz]	decrease [%]	frequency [Hz]	decrease [%]	frequency [Hz]
462	0	3.84	0	6.05	0	15.49
401	4.69	3.66	4.13	5.80	2.52	15.10
300	14.06	3.30	12.07	5.32	8.72	14.14
203	19.53	3.09	15.04	5.14	14.85	13.19
101	20.57	3.05	17.36	5.00	16.98	12.86
1	21.09	3.03	21.65	4.74	19.56	12.46

Table 4.1: Variation of the natural frequencies. All of them strongly decreased when reducing the prestressing force.

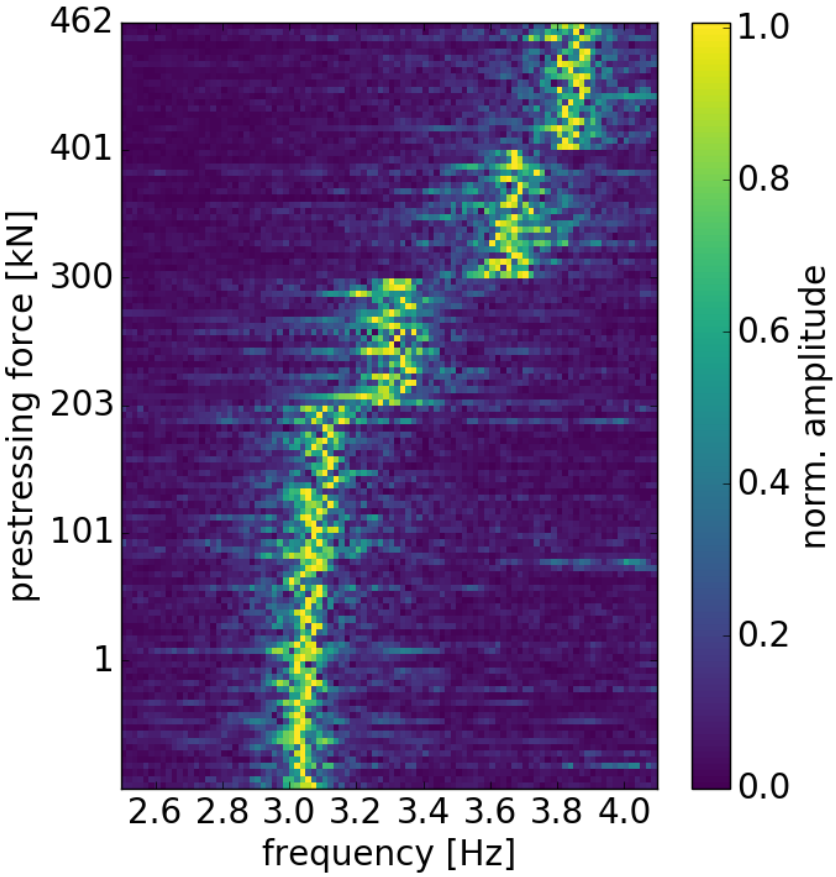

Figure 4.3: Trend of the first natural frequency lying around 3.8 Hz. While the prestress was reduced, the natural frequency moved towards lower values.

4.2 Preprocessing

Before calculating the cross-correlation functions, the raw dataset had to be preprocessed. Therefore, several steps were performed.

First of all, the records were detrended. A linear trend and the mean value were removed to avoid possible influences from instrument drift. For this purpose, the ObsPy function 'detrend' was used.
The next step was the filtering. The spectral analysis in section 4.1 showed that most of the energy lies below 25 Hz. Because of this knowledge, the dataset was filtered with an upper limit of 25 Hz to include all peaks of the amplitude spectrum (Fig. 4.2). 1 Hz was chosen as the lower boundary due to the low sensitivity of the sensors for lower frequencies. In addition, a higher boundary would possibly affect the peak around 3 Hz. The filtering was performed by using a butterworth bandpass filter with four corners. To avoid a resulting phase shift it was applied once forwards and once backwards. Figure 4.4 shows the resulting filtered amplitude spectrum for the initial state with an acting prestressing force of 462 kN. Similar to the unfiltered spectrum, three clear peaks near 4 Hz, 6 Hz and 16 Hz are visible.

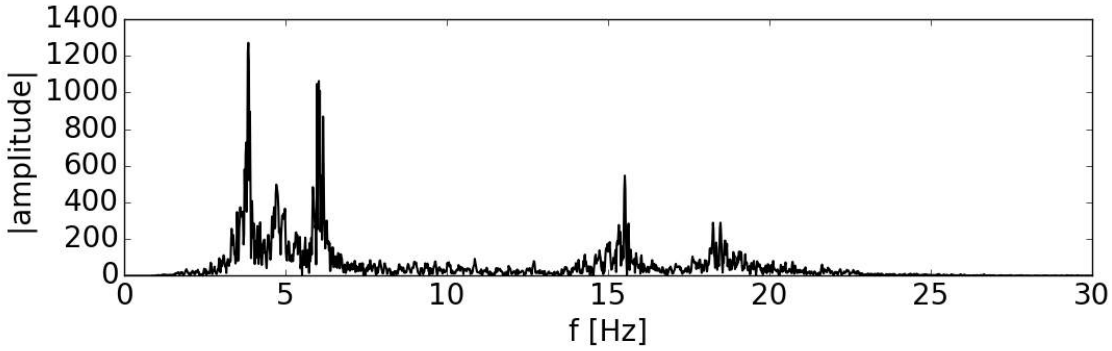

Figure 4.4: Amplitude spectrum of a noise record filtered between 1 - 25 Hz. All of the three eigenfrequencies can still be identified.

To prevent the signals from artifacts caused by the filter process, the data was tapered afterwards. A taper of 5% was suitable. It was applied to the data using again an ObsPy function named 'taper'.

Due to the fact that an explosion was triggered on the neighboring field for testing reasons during the measurement, the dataset was finally subjected to normalization. The so-called 'one-bit normalization' was applied on the signals in time-domain. This method was successfully used before in other studies to suppress non-stationary events like earthquakes or even explosions from noise measurements (e.g. Shapiro and Campillo [2004]).
Figure 4.5 gives an impression of how the normalization works. Figure 4.5 a) shows the processed signal before the normalization. The mentioned explosion is clearly visible around 32 s with a high amplitude. After the normalization (Fig. 4.5 b)) it cannot be identified anymore.
The method assigns +1 or -1 to every sample according to the sign of its amplitude. A positive value is replaced by +1 while a negative value is replaced by -1 [Bensen et al., 2007]. Although the waveform is configured, Cupillard et al. [2011] gives theoretical proof that a one-bit correlation returns the Greens function just as a raw correlation does. In addition, it increases the signal-to-noise ratio and is therefore a typical approach in CWI nowadays [Larose et al., 2004].

After the one-bit normalization was applied the preprocessing of the data is complete and the cross-correlation functions can be calculated.

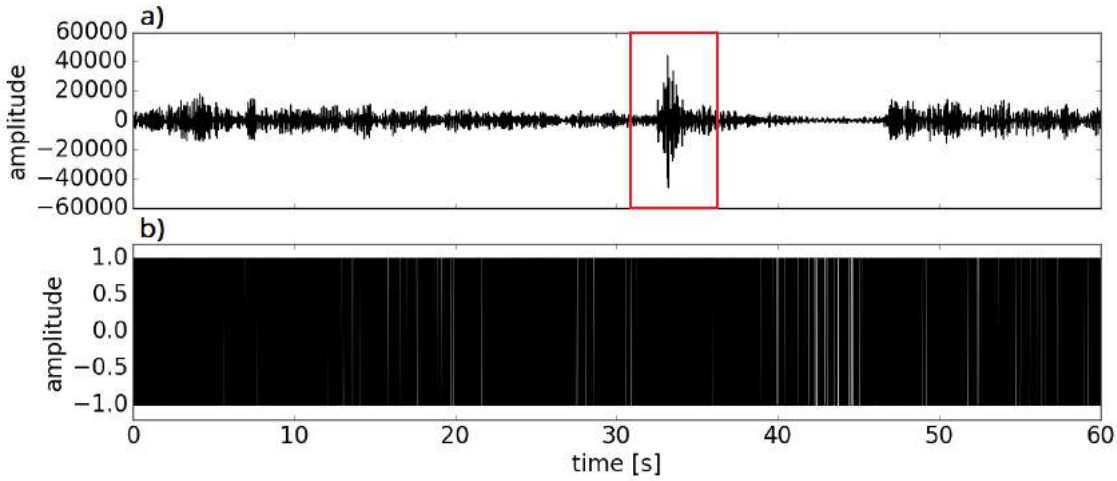

Figure 4.5: Signal a) before and b) after the one-bit normalization. The explosion on the neighboring testing field is marked by the red box. After the normalization was applied, it cannot be identified anymore.

4.3 Cross-correlation

To compare the signals measured with different prestressing forces acting on the structure and to estimate the relative velocity change, cross-correlation functions (CCFs) for each step need to be calculated.

During the experiment 23 sensors recorded the ambient seismic noise. All of the traces were cross-correlated with each other, resulting in 253 possible receiver combinations. Autocorrelations, i.e. cross-correlating a signal with itself, were not taken into account.
For every 1 min-file these 253 cross-correlation functions were calculated, using the ObsPy function 'xcorr'. This function returns not only the highest cross-correlation coefficient and its index but also the complete cross-correlation function. 5000 samples were chosen as shift length. A smaller amount would have led to shorter CCFs whereby a stable noise level could not be identified. Signal could still be observed until the end of the function. This problem would become particularly important for low frequencies with higher wavelengths. The selected shift length of 5000 samples generated CCFs with a time interval of ± 40 s.
To increase the signal-to-noise ratio, all cross-correlation functions belonging to the same receiver pair combination were stacked, resulting in CCFs sampling 20 minutes. Afterwards, the mean was removed separately for each combination to avoid a trend due to the stacking process. In order to be able to visually compare the functions, they were then normalized based on the numbers of files which were stacked, i.e. 20. Finally, we ended up with 253 CCFs per acting prestressing force.
Figure 4.6 shows exemplary a CCF between receiver 4 and 8. The signal part is clearly visible and the function decreases. This suggests that records of 20 minutes are sufficient to apply the stretching method.

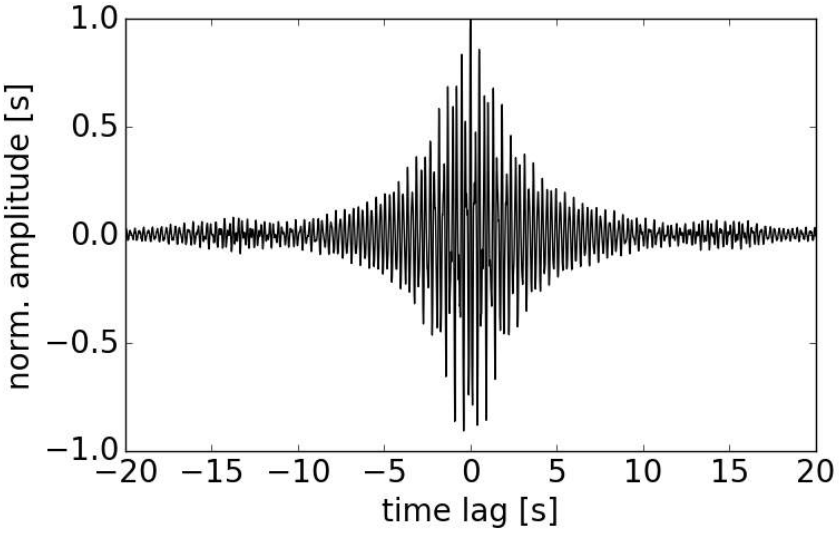

Figure 4.6: Example of a cross-correlation function. Receiver 4 was cross-correlated with receiver 8. The signal decreased to a stable noise level.

4.4 Frequency bands

A visual inspection of the CCFs for the same receiver pairs but different prestressing force showed huge differences in the waveform (Fig. 4.7). The variation of the frequencies and the long frequency range of 24 Hz led to a problem. When applying the stretching method, very low cross-correlation coefficients around 0.2 arose. Because the cross-correlation coefficients are a reliability feature, the estimated relative velocity changes would not be trustworthy.
To avoid this, the idea came up to look at three short frequency bands individually. Salvermoser [2014] showed this approach successfully before with frequency bands between $0.2 - 2$ Hz, $2 - 8$ Hz and $8 - 24$ Hz. He justified his choice by different acting noise sources like wind and cars. The testing area in Horstwalde is located in a forest so most of the noise is caused by wind or humans working in the area. Therefore, the noise level is rather low and depends on the day.
Instead of the source mechanism, the frequency spectrum was considered to select appropriate frequency bands. In Fig. 4.7 b) the local maxima are clearly separated. Therefore, bands were chosen in which there is only one maximum each. However, the variation of the eigenfrequencies by changing the prestressing force was taken into account. Frequency bands between $1 - 4.5$ Hz, $4.5 - 8$ Hz and $8 - 25$ Hz met the stated conditions.
Figure 4.8 shows exemplary the CCFs for each band. The first two bands from 1 Hz to 4.5 Hz and from 4.5 Hz to 8 Hz mostly have the same properties. Both waveforms smoothly decrease while the signals continue to exist after long periods of elapsed time. The third band also decreases, however it shows a more chaotic course. After 6 s the signal changes into noise but another signal window can be found, starting around 10 s.
All three bands have in common that the maximum is slightly moved towards the causal part. This observation gives an idea of the location where the strongest noise came from. The CCFs were calculated by shifting the signal from a more southern receiver against a northern receiver, i.e. a sensor with a higher number was shifted against a sensor with

namely?
give more detailed explanation

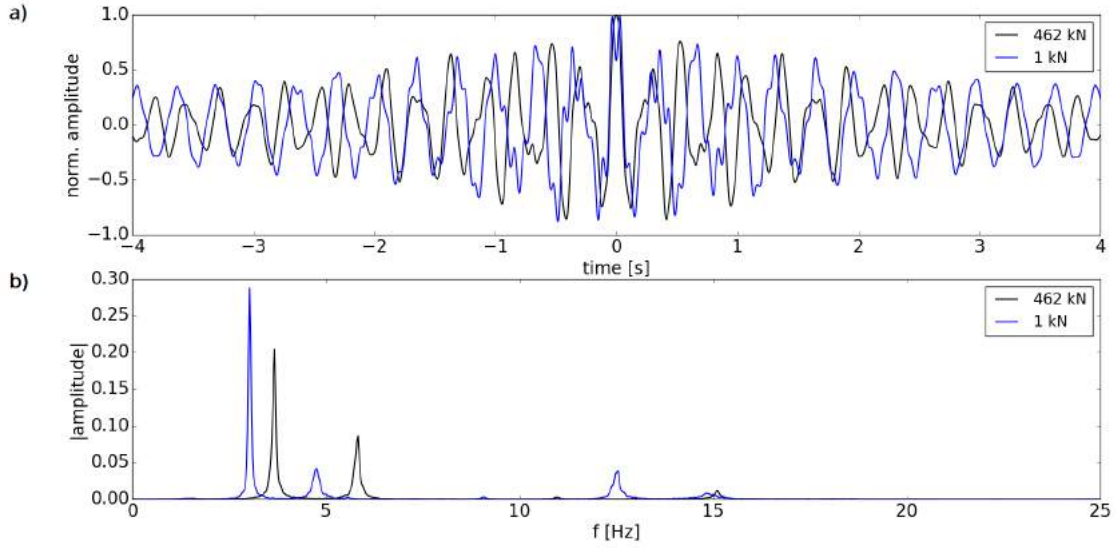

Figure 4.7: CCFs between receiver 4 and 8 for a prestressing force of 462 kN and 1 kN. a) Waveform, b) amplitude spectrum. The waveforms are clearly different due to the strong variation of the included frequency content.

a lower number. Because of this approach it can be concluded that the strongest noise source was located south of the structure. The shift of the maximum towards the causal part can be seen for all measurements during the experiments, independently of prestressing force or receiver pair.
A visual comparison between the waveforms extracted from different prestressing forces but same frequency bands showed significantly lower differences. It was therefore expected that the following stretching method will now provide a higher correlation, and because of this more reliable results for the relative velocity change.

4.5 Stretching method

To get the relative velocity changes $\frac{dv}{v}$, the stretching method had to be applied on the previously calculated CCFs. A python script written by Céline Hadziioannou and improved by Sarah Hable and Johannes Salvermoser was used. It processed the data as follows:
First, a time vector is produced, limited by a given start and end time. Details about the estimation of these two parameters can be found in the following section 4.5.1. Afterwards, the cross-correlation between the actual signal and the reference signal is computed. It is done for every stretching coefficient in the selected time window. Subsequently, the highest correlation is returned which gives the best fit between a stretched or even compressed signal and the reference signal. The relative velocity change can then be extracted from the belonging stretching coefficient ε as shown in equation 6.

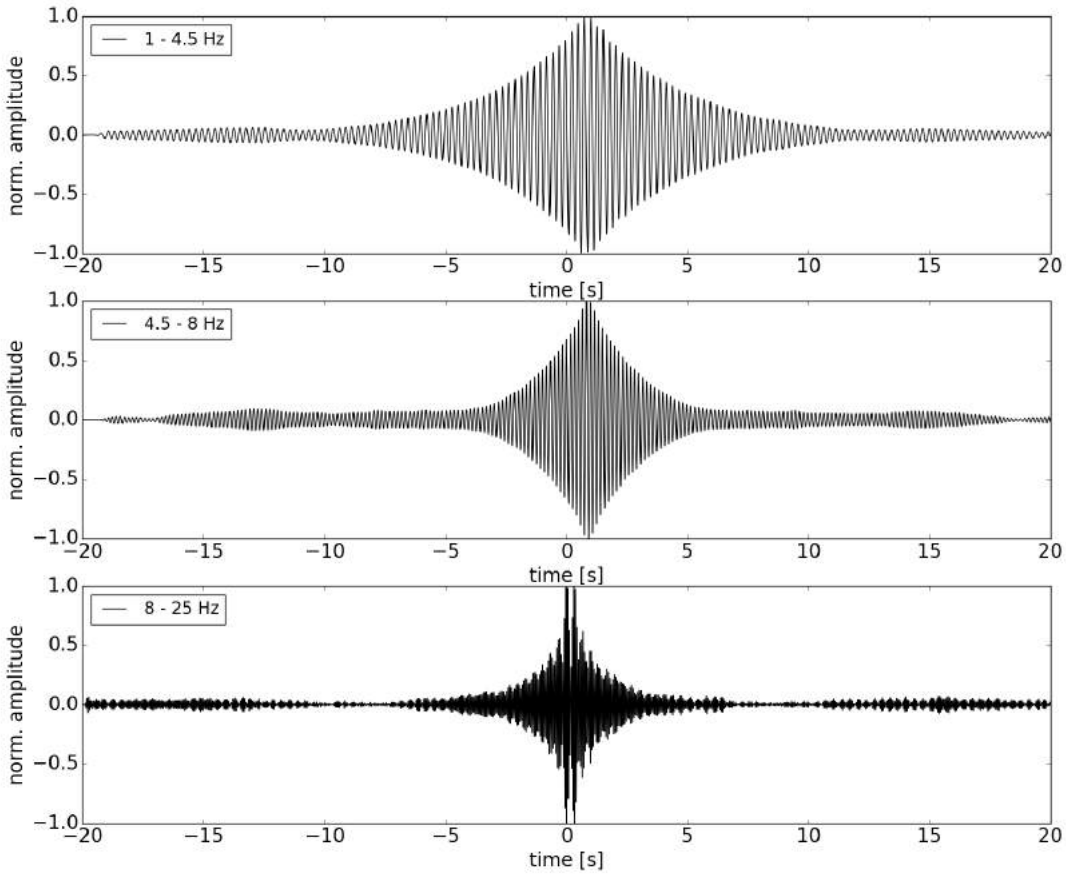

Figure 4.8: Investigated frequency bands from receiver 3 and 23 for a prestressing force of 462 kN. All of the functions show a maximum in the causal part which can be related to the position of the strongest noise source.

The stretching coefficient ε was chosen between -0.3 and 0.3 with an increment of 0.0001. This resulted in 6000 traces, 3000 of which were stretched versions of the actual signal and 3000 were compressed versions. If a signal needs to be stretched it means that the velocity is getting smaller. Conversely, a compressed signal indicates an increase in velocity. The small interval selected allows a detection of velocity changes of up to 0.1%. The high boundaries of the stretching coefficients were chosen after looking at the waveforms of the CCF at 462 kN and 1 kN. Velocity changes around 28% could roughly be estimated.

Another decision which had to be made before using the algorithm is the choice of the reference signal. The initial state with a prestressing force of 462 kN was selected. By comparing this function with all the other five functions belonging to lower prestressing forces, the overall trend of the relative velocity change could be observed. However, it should be noted that this would give a wrong impression. Instead of the supposed decrease in velocity due to the opening of cracks, an increase would be visible. The results would show the velocity change while raising the prestressing force.
To avoid this, the initial state of 462 kN was taken as the actual signal which was stressed and compressed. All other CCFs were left unchanged and were used as reference.

4.5.1 Time window length estimation

One of the most important parameters to choose is the time window length in which the stretching method is applied to the data. The time window defines the part of the CCF that is stretched or compressed to fit best to the same part of the reference function.
To get reliable results, attention must be paid to some aspects. On the one hand, the time window has to be in the late part of the CCF to avoid the influence of direct surface waves. Coda waves shall be used due to the previously mentioned sensitivity to changes in the structural properties. On the other hand, the time window should not be too large because it must not contain any noise. The signal still has to be present.
In addition to complying with these conditions, there were also large variations in the prestressing force that made the choice difficult. Using the decay of amplitude of the CCFs at 462 kN as indicator for the window length failed. At least one of the other five CCFs resulted in bad correlation. This was caused by cycle skipping which happened at different times for all prestressing forces. Cycle skipping occurs if the algorithm matches the wiggles of the current signal with the wrong ones of the reference. If this happens an incorrect stretching coefficient and therefore a false velocity change will be computed [Mikesell et al., 2015].

The aim was to find one time window length for every frequency band separately in which we see a high coherence between signal and reference for all prestressing forces. To accomplish this, the frequency bands were examined independently but using the same procedure. Moreover, the decision of a start and end time, varying with changing receiver pairs was made to react to the different distances between the sensors. However, the same window length was chosen for all receiver pairs and prestressing forces in order to make the results comparable.

First, the start times had to be determined. Therefore, the maxima of the CCFs were used as an indicator. All of them were in the causal part of the CCF. Their locations indicate the arrival times of the direct waves. To avoid this influence on the results, the central frequencies of every frequency band were taken into account. One period of the corresponding central frequency was added to the direct wave arrival time. This was done for each of the different receiver pairs. In order to get reasonable start times that work well for all prestressing forces, start times for all the receiver pairs were calculated separately. Because direct waves should always be neglected, the latest start times were chosen, resulting in 253 start times per frequency band.
After having estimated the start times, appropriate end times had to be found. This was done by applying the stretching algorithm in a time window with varying length. Inside this, the cross-correlation coefficient and the relative velocity change was calculated. While the start time was fixed, the end time was moved back sample per sample, e.g. the window widened by 0.004 s with each iteration step. Due to computational reasons, only the randomly picked CCF between receiver four and eight was used for this investigation. Figure 4.9 shows exemplary the results when comparing the CCF from 462 kN with the one from 300 kN, starting at 2.67 s. However, the comparison was made for all of the six CCFs of the selected receiver pair. Several maxima with high correlation can be found. Additionally, cycle skipping can be seen at points where the relative velocity change $\frac{dv}{v}$ suddenly drops off. To find the best end time for all prestressing forces, all times where local maxima can be observed were noted. Then, the corresponding window length was calculated and tested for all other prestressing forces. The length that gave the highest correlation for all on average was adopted.
The ultimately chosen time windows can be seen in Fig. 4.10 for all frequency bands. The red lines indicate the start and end times. Notable is the increase in length with an increase in frequency. This is due to the long lasting reverberations for lower frequencies. In addition, all of the estimated time windows are located in the signal part and therefore hold the previously mentioned condition of not containing any noise.

The window lengths used for the stretching method were 11.556 s ($1 - 4.5$ Hz), 7.124 s ($4.5 - 8$ Hz) and 5.864 s ($8 - 25$ Hz). All start and end time can also be extracted from table C.1 in appendix A.

4.6 Results

This section takes a look at the estimated relative velocity changes when applying the stretching method on the passive noise measurements for changing prestressing forces. To get an idea of the general trend, the resulting velocity changes were averaged over all receiver pairs. Combinations with a cross-correlation coefficient lower than 0.6 were neglected. This threshold was chosen to exclude measurements with bad correlation in order to get suitable results. On the one hand a preferably high amount of receiver pairs should be used, on the other hand the overall trend should not be influenced by bad results. The selected value of 0.6 was a good compromise.
In general, all three frequency bands show an overall decreasing trend (Fig. 4.11). This means that the velocity decreases while reducing the prestressing force. Nevertheless, striking differences can be seen between the bands. The exact values for $\frac{dv}{v}$ and the be-

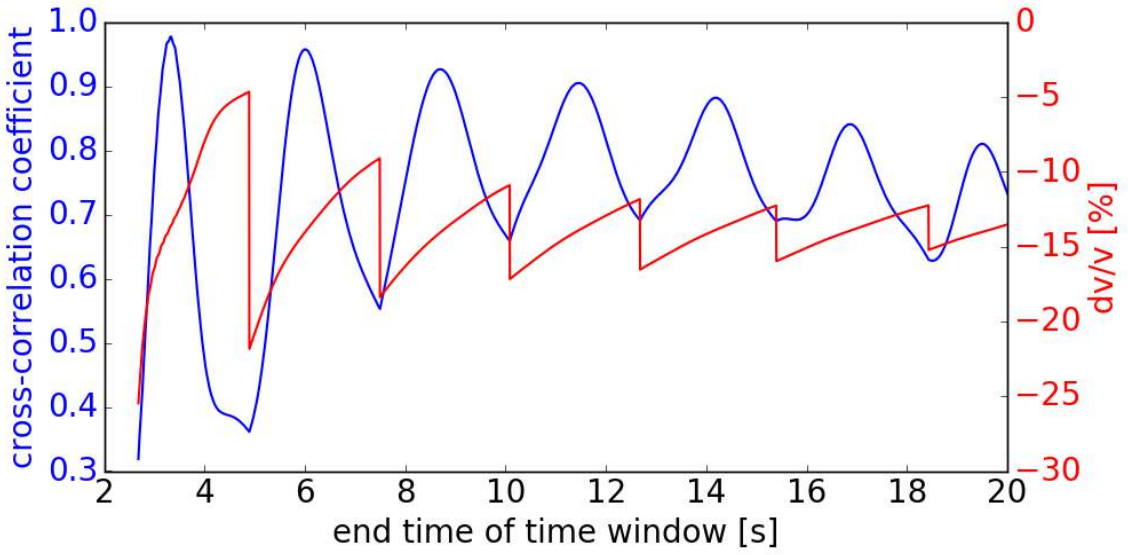

Figure 4.9: Window size estimation. Here, the stretching method was applied on the CCF between sensor 4 and 8 measured at a prestressing force of 300 kN. The frequency band from $4.5 - 8$ Hz was used. The cross-correlation coefficient as well as the relative velocity change varied strongly due to cycle skipping.

longing correlation coefficients are given in table 4.2.
For frequencies between 1 and 4.5 Hz the velocity change drops fast until 203 kN down to a value of -26.4%. Afterwards, the velocity slightly increases. Thereby the correlation gives high values for all prestresses. The lowest one can be found for 300 kN with around 0.72.
The frequency band from 4.5 to 8 Hz shows more or less the same behavior. In this case the graph decreases since a prestressing force of 101 kN is reached. By reducing the prestress again about 100 kN the velocity change increases by 0.16%. Additionally, a rather low correlation of 0.68 can be found around 203 kN.
Compared to the other two bands, high frequencies show larger variations and lower correlation coefficients. Similar to the lowest frequency band, the velocity change decreases for the first three prestressing changes. Then a high increase can be observed before the graph again drops off to -24.46%.
Taking the courses of all three graphs into account, the following can be summarized: The velocity strongly decreased for a prestress reduction to about 259 kN. A possible explanation for this is the forming or widening of cracks. This would lead to an increased spread of the seismic waves in air. In a previous study by Mierschke [2018], values ranging from 3.5 to 3.8 $\frac{\text{km}}{\text{s}}$ were found as velocities for guided P-waves traveling in this concrete structure. Because the velocity of seismic waves in air ($\approx 0.3 \frac{\text{km}}{\text{s}}$) is much lower, a high decrease in velocity can be assumed. What happened after the prestress was further reduced is more difficult to understand. During the measurement, however, it could be observed that the bridge sagged visibly when the prestressing force was completely removed.

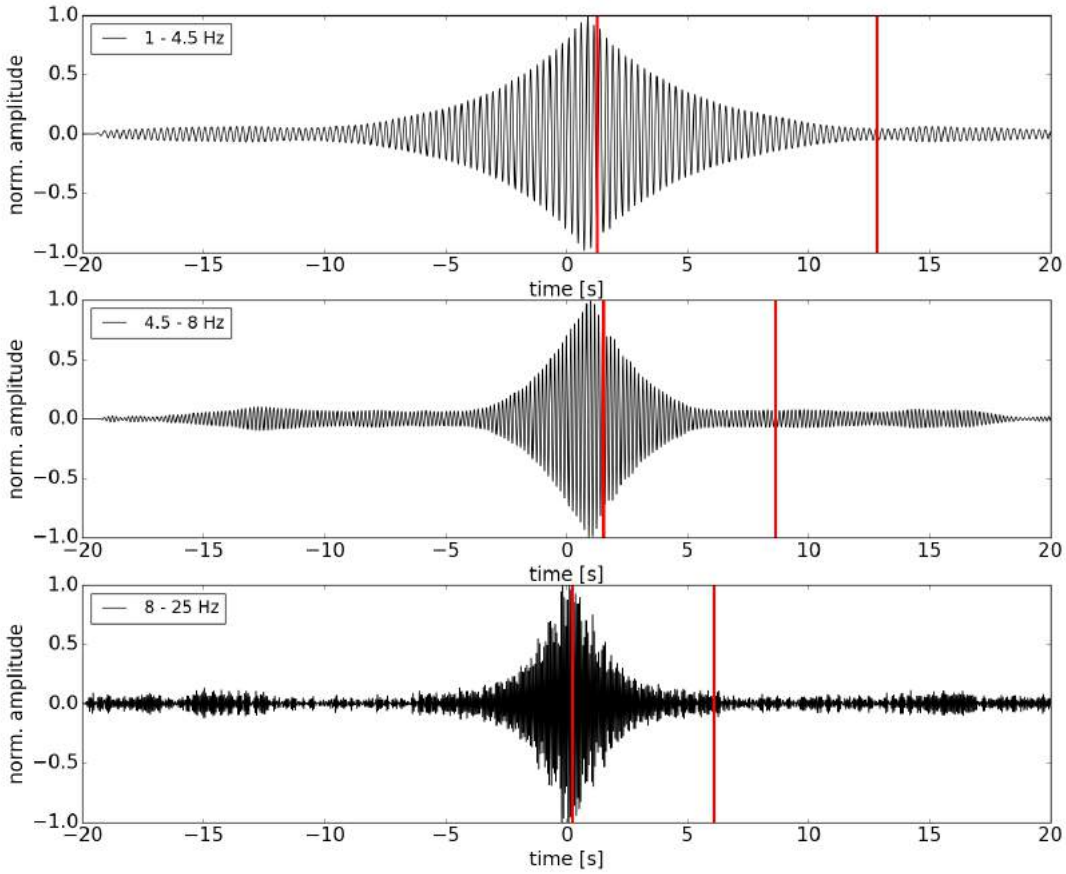

Figure 4.10: Estimated time windows for all frequency bands. The red lines indicate the start and end times exemplary shown for the signal at 462 kN for the receiver pair 4/8.

+figure showing cc values vs prestress.

prestressing force	frequency band					
	1 - 4.5 Hz		4.5 - 8 Hz		8 - 25 Hz	
	cross-corr. coeff.	dv/v	cross-corr. coeff.	dv/v	cross-corr. coeff.	dv/v
462 kN	1	0 %	1	0 %	1	0 %
401 kN	0.92	- 4.03 %	0.94	- 4.18 %	0.83	- 2 %
300 kN	0.72	- 13.31 %	0.89	- 13.83 %	0.82	- 9.18 %
203 kN	0.84	- 26.38 %	0.68	- 21.42 %	0.72	- 17.21 %
101 kN	0.9	- 25.63 %	0.84	- 26.67 %	0.72	- 14.03 %
1 kN	0.77	- 25.30 %	0.84	- 26.51 %	0.77	- 24.46 %

Table 4.2: Relative velocity changes and belonging cross-correlation coefficients of the passive measurements. All frequency bands showed the same trend.

One way to get more information about the processes inside the structure is to look at the velocity change along the structure. While the detection of damage within a structure is more or less feasible today, the localization is still a challenge.
Now, only the receiver combinations with an inter-distance of two meters are considered. While starting at the northern side of the structure, receiver pair 1/3, 3/5, 5/7 etc. were used. The correlation coefficients obtained before were highest for the frequency band between 1 and 4.5 Hz. Therefore, only this band was used for the investigation over distance. Figure 4.12 shows the results with all applied prestressing forces plotted in different colors. On the left side the cross-correlation coefficients are displayed. The right side shows the relative velocity changes.
When looking at the relative velocity changes, the first thing that stands out is the similarity of the colored curves. For all of them the velocity change stays constant along the structure. That means, the northern part of the structure (receiver no. 1 - 11) behaves in the same way as the southern part (receiver no. 13 - 24). However, a striking feature can be observed between sensor 11 and 13. They are located on the left and right side of the pillar (see Fig. 3.6). There, the velocity change falls off while this drop gets higher with lower prestressing force.
When releasing the prestressing force one assumes that most of the cracks would form at positions where the strongest curvature can be found. Due to bending this would be in the middle of each structure half and at the pillar's location. However, the decrease in velocity can only be observed here at one place. This may indicate where the greatest damage has occurred.

or local strain/deformation → μ & ε changed.

In principle, the results show that the two lower frequency bands are more stable than the one from 8 to 25 Hz when estimating the relative velocity change. Nevertheless, all three frequency bands seem to be suitable for the approach. To confirm this, the active measurements were processed in the same way described in chapter 5.

overall: cracks/damage not the only possible reason for dv/v; changed elastic parameters due to changed stress can also contribute dv/v. Take this into account in interpretation!

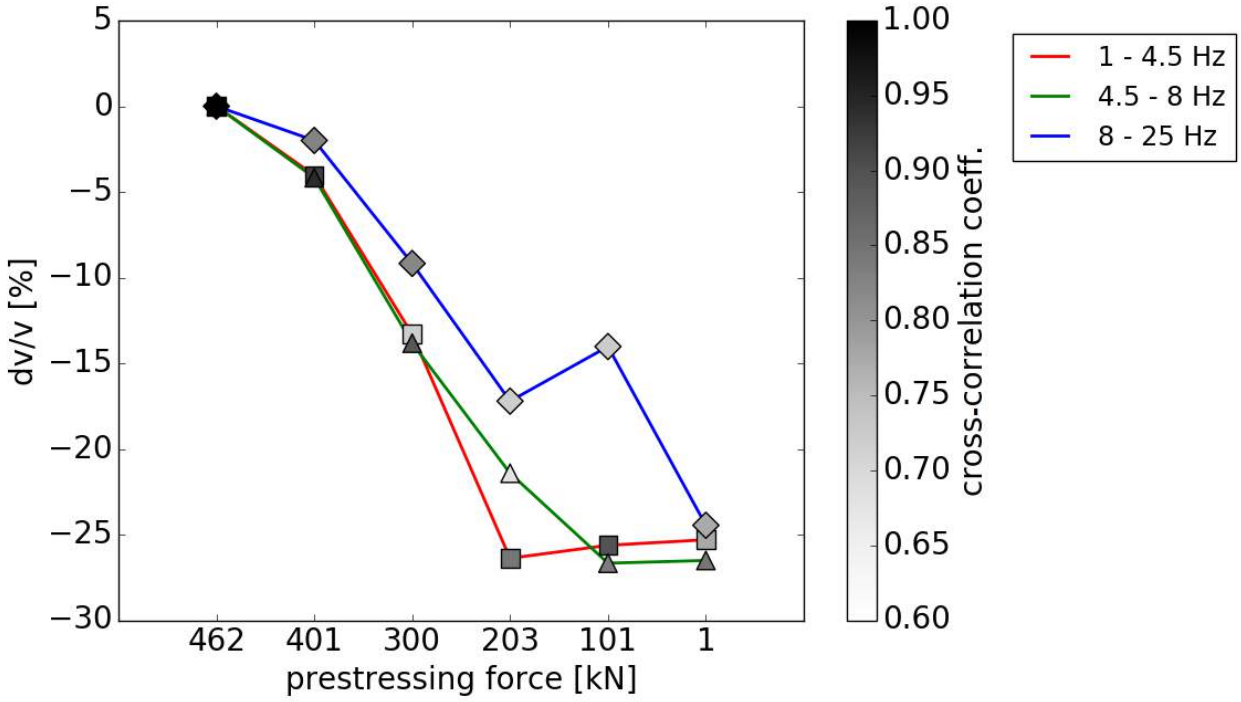

Figure 4.11: Results of the applied stretching method on the passive noise measurements. The relative velocity change is shown as well as the cross correlation-coefficients for all three frequency bands. In general, the velocity decreased when the prestressing force was reduced.

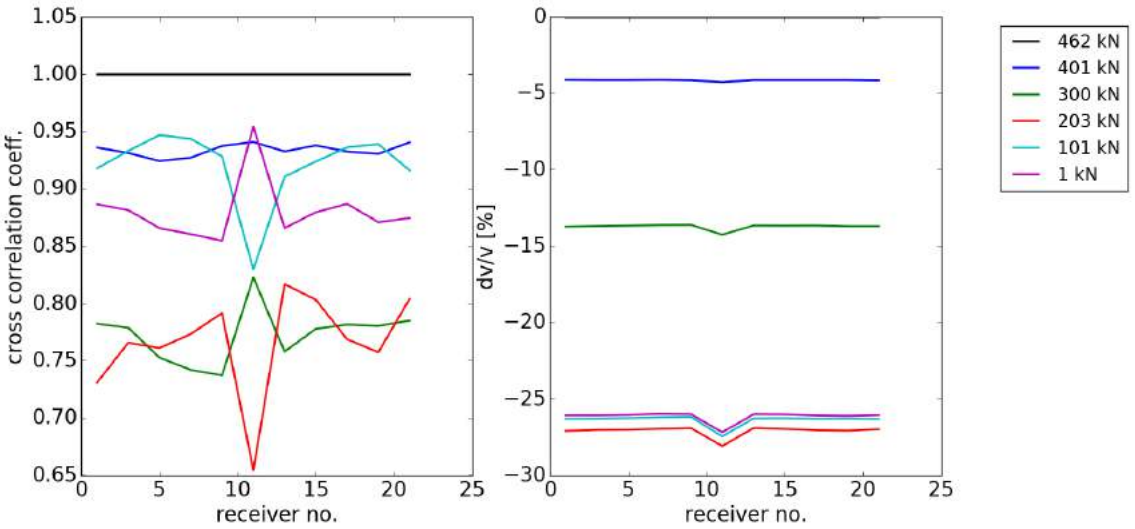

Figure 4.12: Relative velocity change and cross-correlation coefficients along the structure with an inter distance of 2 m between the receivers ($1 - 4.5$ Hz). A decrease in velocity change can be seen at the middle pillar's position.

5 Release of prestressing force - active data

5.1 Raw data

In addition to passive data, active data was also measured during the experiment. As described in section 3.3 hammer-blow seismic was carried out between sensor 20 and 21 for every used prestress.

A time-distance plot should give a first impression of the recorded signals. An exemplary blow at the initial state of 462 kN is displayed in Fig. 5.1. Vibrations can be easily observed at least 2 seconds long. By zooming into the plot it can be seen that sensor 20 registered the first arrival. This was expected due to the proximity to the source of the blow.
Additionally, some interesting aspects become apparent. Noticeable is the signal received at sensor 12 which was placed on the ground instead of on top of the concrete structure. It also recorded the seismic waves emitted by the hammer blow, even if the signal decays faster. Another striking behavior can be seen for sensor 24 and both of the sensors located in the middle of the structure halves, 6 and 18. While all of the other receivers showed similar waveforms, the signal at sensor 24 looks more like the signal received at sensor 12. This can probably be attributed to a bad coupling or instrument problems. Noise previously recorded by this sensor also resulted in bad correlation with other sensors.
The signals recorded at sensors 6 and 18 show a longer wavelength than the rest of the sensors. A possible explanation could be their location. Because of preciously conducted experiments, the structure was already slightly damaged at the start of the measurement. The middle of the structure halves is where most of the existing cracks are expected due to bending.

With the help of the spectrogram, conclusions can be drawn about the generated frequencies. Figure 5.2 shows both the spectrogram as well as the amplitude spectrum. In the spectrogram there are several features visible which could be seen before in the spectrogram of the noise records in Fig. 4.1. For example the continuous signals below 25 Hz. The hammer blow can be identified easily around 24 s by the vertical line which shows high energy. This high energy is spread over the entire frequency range.
The amplitude spectrum looks almost the same as in Fig. 4.2. Three striking peaks can be seen around 3 Hz, 7 Hz and 16 Hz. Nevertheless, the high amplitudes have to be noticed. For the noise measurements the dominant frequency was around 4 Hz, whereas here it can be found around 16 Hz. Additionally, its amplitude is approximately 17 times higher. Moreover, the frequency content is much broader compared to the amplitude spectrum of the noise measurements. Also, high frequencies appeared with high energy, even if they were neglected for further processing for comparison.

After the frequency range was investigated, the active signals can be processed appropriately.

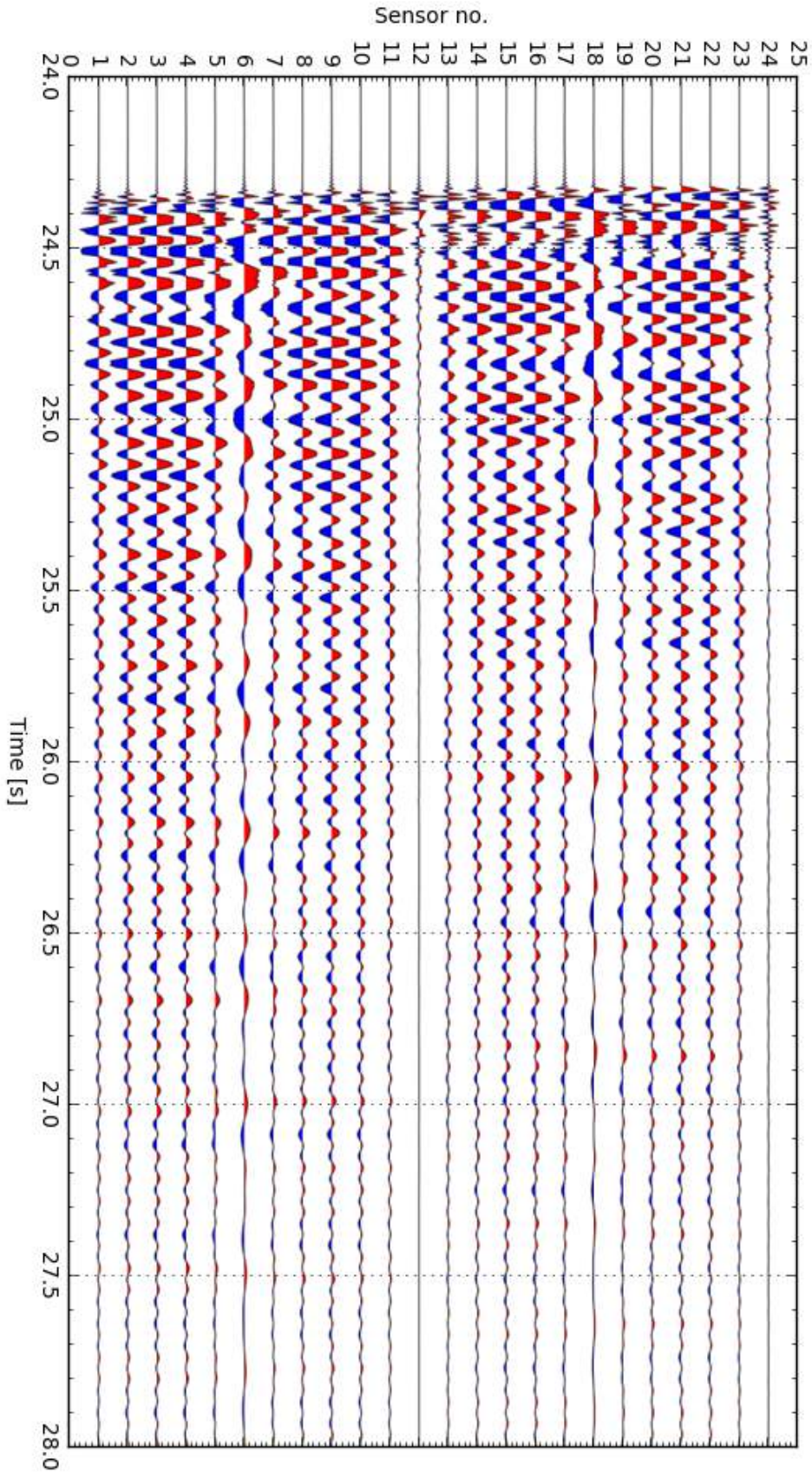

Figure 5.1: Time-distance plot of a hammer blow induced raw signal for a prestressing force of 462kN. When comparing the waveform, differences between the records for some sensors can be found.

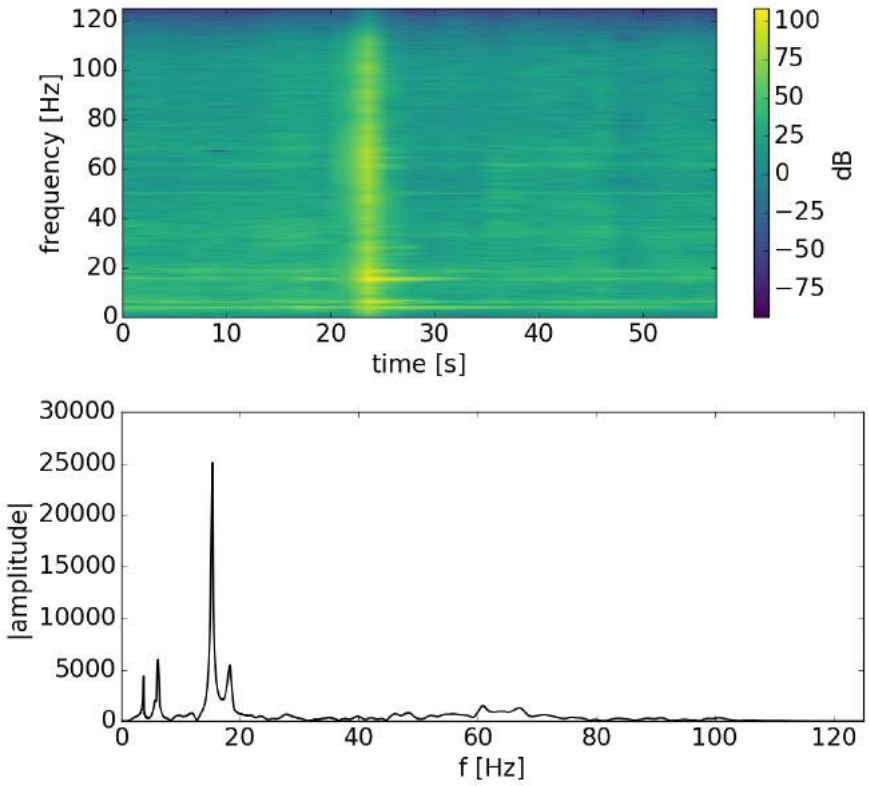

Figure 5.2: a) Spectrogram and b) amplitude spectrum of a hammer blow induced raw signal for a prestressing force of 462 kN. The hammer blow can be clearly identified at a time of 24 s.

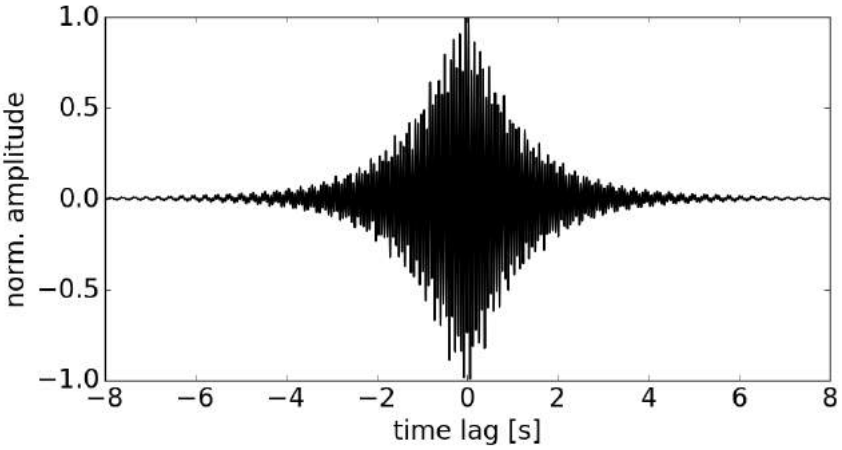

Figure 5.3: Example of a cross-correlation function estimated from active measurements. Receiver 4 was cross-correlated with receiver 8. The function clearly decreased to a stable noise level.

active signals could also be used without xcoff first (since they are a sort of "greens function" already..)

5.2 Processing

The active measurements should serve as a confirmation for the results estimated by the noise measurements. Because of this, they were processed in the same way.

In order to get the same frequency range, the active dataset was filtered between 1 and 25 Hz. Afterwards, the signals were visually inspected. Because of a data gap due to storage time, not all of the ten recorded blasts were suitable for further processing. A continuously recorded time span of 21 seconds, starting one second before the first arrival was used as condition. In the end, there were four blasts for every used prestressing force left, holding the restrictions.
These were cross-correlated by using a shift length of 2000 samples, resulting in CCFs with a time interval of ± 8 s. By stacking them, a higher SNR could be achieved. Fortunately, the CCFs converge to a stable noise level even if they sample only four minutes instead of 20 (Fig. 5.3). This allowed the assumption that the stretching method will also give reliable results also for the active measurements which can then be used for a comparison.

In order to apply the technique, the same frequency bands were selected first. Also the procedure to find an appropriate time window was also carried out again. All start and end times can be extracted from table C.1 in appendix A. The window length for frequencies between 1 and 4.5 Hz was 6.08 s. For frequencies between 4.5 and 8 Hz it was 4.344 s long and for frequencies between 8 and 25 Hz the length was 3.636 s.

A first look at the relative velocity changes shows that the results seem to be very similar to the previous ones. While the prestressing force is reduced, the velocity decreases around -27.44% on average. A detailed comparison of the results which were determined using the active or passive data can be found in chapter 7.1.

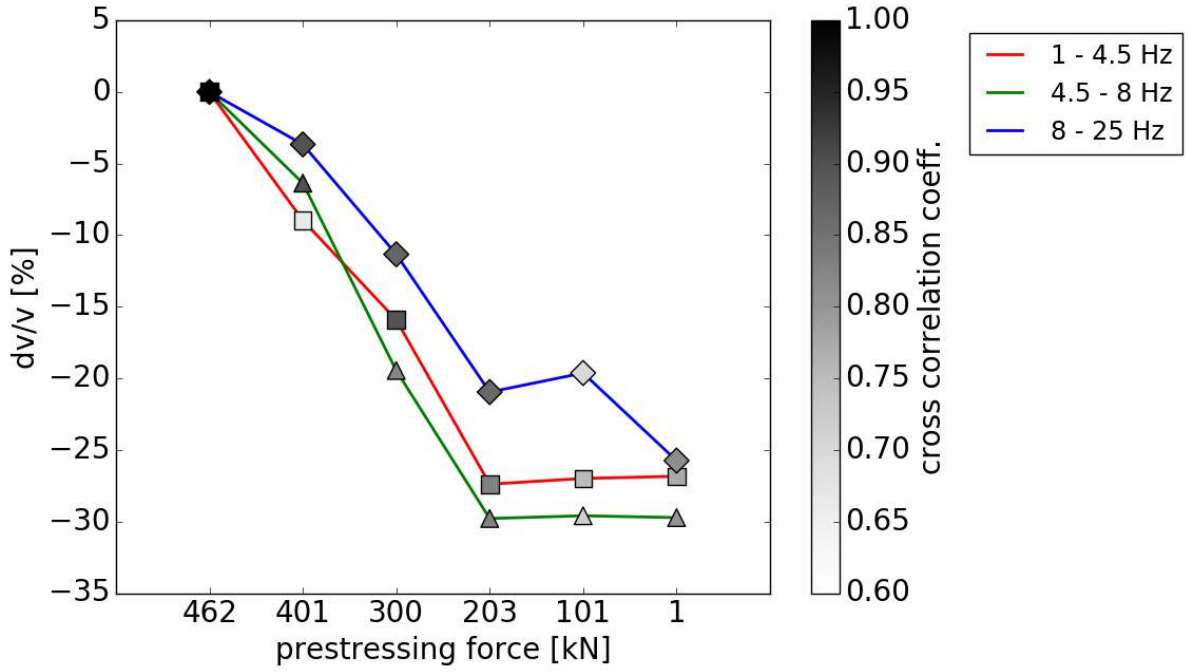

Figure 5.4: Results of the applied stretching method on the active measurements. The relative velocity change is shown as well as the cross correlation-coefficients for all three frequency bands. In general, the same trend as for the passive measurements can be seen.

6 Influence of temperature

6.1 Processing of data

While the seismic velocity is influenced by the change in the prestressing force, it is also highly affected by temperature variations. Higher temperatures lead to a slower propagation of seismic waves in the medium. Accordingly, the travel time variation increases, corresponding to the linear relation between relative velocity changes and relative travel time variations (see eq. 4). This behavior was shown before (e.g. Salvermoser [2014]).
Because of this effect, the influence of the temperature has to be removed from the previous examined velocity changes. Only then, changes in the seismic velocity can be traced back to possible damages in the medium. However, it should be noted that other factors that have not been taken into account yet can further influence the velocity of the seismic waves.

Two months of ambient noise data was available to determine a velocity variation rate per degree Centigrade. In general, the data shows the same frequency content as the spectrum of the raw signals in Fig. 4.2. Therefore, it was processed in the same way described in detail in sections 4.2 and 4.3. The CCFs were stacked hourly due to the resolution of the temperature data sets which shall be used for comparison later on.
In contrast to the previous approach of using the initial state as reference for the stretching method, another function is chosen here. Because the expected variations of the velocity are rather low, the respective function should be comparable. Therefore, all determined CCFs were stacked and normalized to get an average cross-correlation function for the whole time span. This one serves as reference function when applying the stretching method.
Nevertheless, the stretching method has to be applied in narrow frequency bands separately in order to get reliable velocity changes with preferably high correlation coefficients. The natural frequencies were used as a guide to make sure that every CCF contains enough signal. Generally, the noise level at the site is rather low. While the previous estimated low frequency band ($1 - 4.5\,\mathrm{Hz}$) and the middle one ($4.5 - 8\,\mathrm{Hz}$) appear to be suitable, the band including higher frequency band must be adjusted.
Because there were several smaller peaks varying inside the frequency range of 8 to 25 Hz the band was selected more narrowly. In order to definitely include the natural frequency around 15 Hz, the continued investigation was limited to frequencies between 12 and 16 Hz.

Again, each frequency band needed its own appropriate time window. For the estimation, the reference function served as a guide. The start times were selected using the same approach described in detail in section 4.5.1. That means, every receiver pair got a different start time, according to the position of its maximum.
To determine the corresponding end times, the envelope was calculated for every receiver pair of the reference function. For this, the ObsPy function 'envelope' was used which is included in the signal processing routines. Then, the end times were selected by using the decrease of the envelope's amplitude. The time when the amplitude decreased by 75%, corresponding to its maximum, was chosen as the respective end time.

With this method some of the receiver pairs ended up with time windows of a length of about 2 s. To avoid these too small time windows, a minimum length was set: According to its central frequency, the window must contain at least three periods of the belonging central frequency.
By using the estimated time windows, the stretching method could be applied afterwards. Due to computational time, the stretching coefficient was adjusted. Because the prestressing force was not changed in the investigated time span, limits of -0.1 and 0.1 should be sufficient to resolve the relative velocity changes. The selected limits correspond to a maximum stretching/compressing of 10%.

6.2 Results

The relative velocity changes were calculated for the period from the 19th of March to the 25th of May 2019 for each of the three previously selected frequency bands. The mean travel time variations $\frac{dt}{t}$ for the frequency band from 1 to 4.5 Hz are displayed in Fig. 6.1 together with the corresponding cross-correlation coefficients.

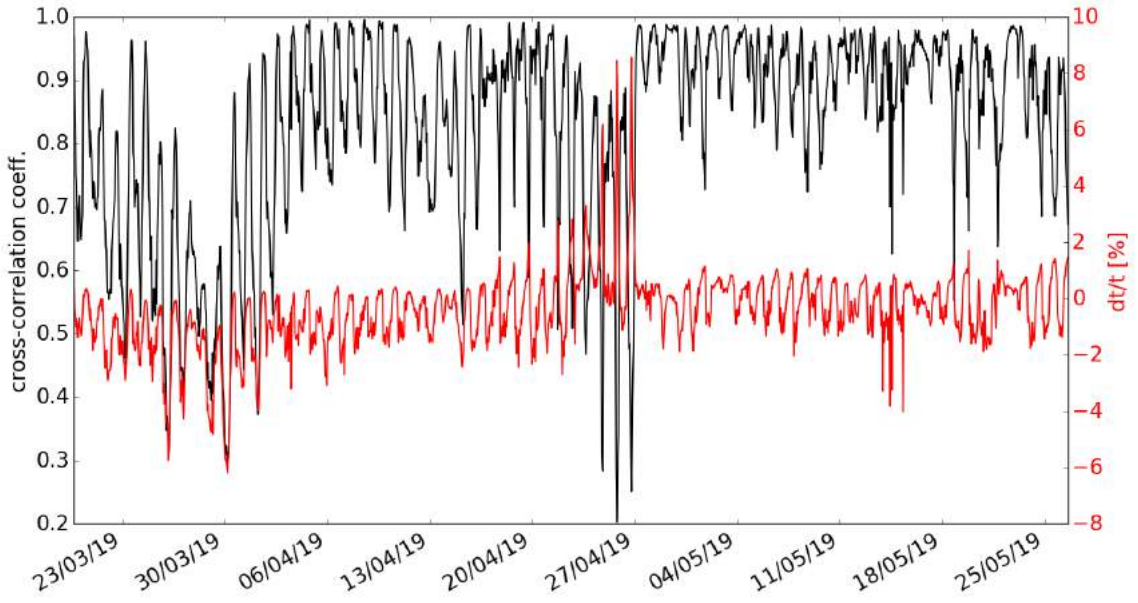

Figure 6.1: Travel time variations and belonging cross-correlation coefficients (1-4.5 Hz). Two periods (27/03 - 01/04 and 24/04 - 27/04) with low cross-correlation coefficients can be identified.

It can be seen that the cross-correlation coefficients are almost above 0.6 for the whole period. Nevertheless, there are two time spans in which they drop off rapidly. One is roughly between the 27th of March and the 1st of April and the other one is from the 24th of April to the 27th of April. During these times, something must have influenced the measurement. The first drop can possibly be explained by strong rain events happening in exactly this time span (see Fig. 6.2). After the precipitation the structure appears to dry, with the coefficients slowly increasing again.

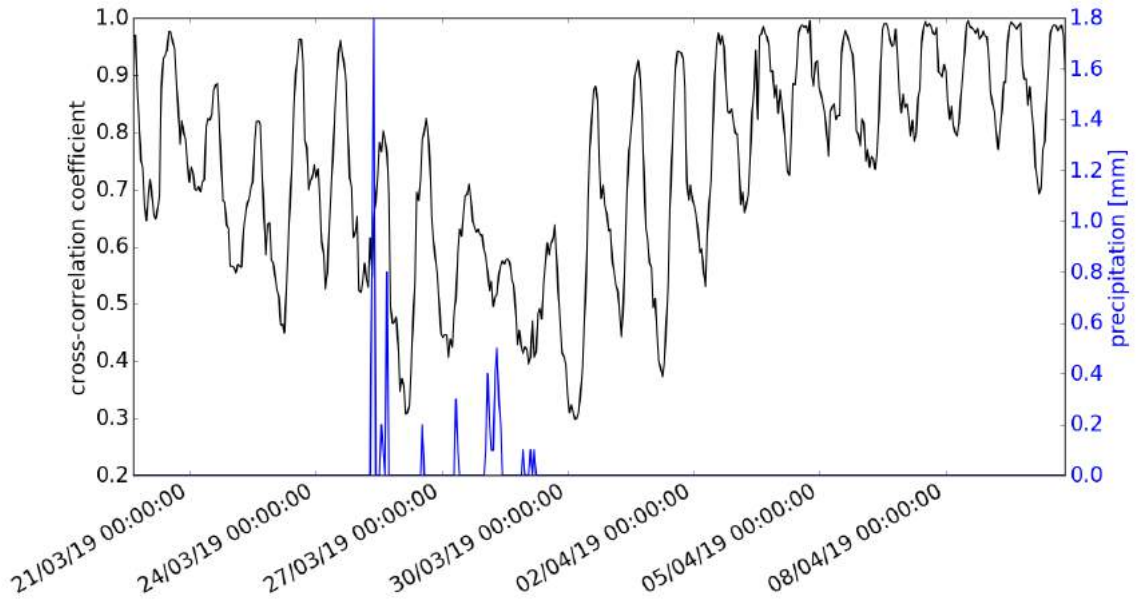

Figure 6.2: Drop of the cross-correlation coefficients (1-4.5 Hz). A connection with the precipitation (blue curve, measured in Baruth) is conceivable.

For the second period there is another reason for the deteriorating correlation. Most likely, the loss of coupling can be seen here. Due to environmental influences, the plaster has started to break and dissolve over time, resulting in lower correlation. Therefore, the geophones needed to be reattached to the structure. After this reattachment, it can be seen that the correlation coefficients are immediately larger than before.

In addition to the coefficients, one should also keep an eye on the travel time variations. They clearly show a periodic behavior which can be attributed to the daily temperature profile. In comparison to the results obtained by the changing prestressing force, these values are significantly lower. Most of the changes lie between -2% and +2%. These values are a magnitude smaller than the results obtained in section 4.6. This shows that the loss of prestress has a clearly higher influence on the relative velocity changes than the temperature variations.
By looking at the travel time variations and the corresponding cross-correlation coefficients for the frequencies between 4.5 and 8 Hz, or rather between 12 and 16 Hz, the same aspects become visible (see Fig. D.1 and D.2).

6.3 Temperature reduction

In order to remove the influence of the temperature on the estimated relative velocity changes, a temperature reduction had to be applied. Due to the fact that the temperature is linearly related to $\frac{dt}{t}$, a linear regression model can therefore be used [Salvermoser, 2014].
In a first processing step, the correlation between the relative travel time variations $\frac{dt}{t}$ and the temperature changes was calculated for the whole measurement period of two months. Here, both the air temperature and the soil temperature data sets were considered.

For all of the three frequency bands there was a better correlation with the soil temperatures (see table 6.3). Because of that, only the temperatures measured in a depth of 5 cm were used to determine the temperature effect. Nevertheless, it should be noted that the best coherence was also just around 0.624. The corresponding frequency band was the one from 1 to 4.5 Hz. Therefore, this band was used for further processing. In Fig. 6.1 the belonging travel time variations are displayed together with the selected temperature data set. They were compared in order to identify a possible temporal delay. Due to the resolution of the data, the smallest identifiable shift would be one hour. However, it turned out that in general there seemed to be no time shift between them.

In a next step, a linear regression is carried out, determining the two parameters a and b. The mean travel time variation rate per degree Centigrade is given by a whereby b is a non-dimensional constant with no physical meaning [Salvermoser, 2014]. The resulting travel time variations due to the temperature deviations $T(t)$ are then given by:

$$[\frac{dt}{t}(t)]_{calc} = a \cdot T(t) + b \tag{8}$$

Using the entire time span gave the following values: $a = 0.134 \frac{\%}{^\circ C}$ and $b = -2.236$. The belonging linear function is shown in Fig. 6.4 c). Here, one can also clearly see the linear relation between the temperature and the travel time variations fitted by the red curve.

Finally, the temperature effect can be removed. The measured travel time variations can be seen in Fig. 6.4 b) together with the calculated new ones. The measurement was corrected by subtracting the calculated values $[\frac{dt}{t}(t)]_{calc}$.The resulting residuals which are shown in Fig. 6.4 a) were rather high which led to the assumption that the measured velocity changes were not only influenced by the temperature. Another possible explanation could be the time span used for the parameter estimation. Both periods mentioned before, showing low cross-correlation coefficients, were also considered.

For this reason, a better approximation of the temperature effect should be reached by using smaller time spans. The same process is carried out again, this time with the weekly measurements being considered separately. For each of them a possible temporal delay between the temperature and the $\frac{dt}{t}$-values as well as the corresponding correlation coefficients were calculated. They can be extracted from table 6.2. The determined parameters a and b are also shown here.
It should be noted that the week in which the sensors were reattached to the structure (23.04 - 30.04) gave the second highest correlation. Showing a time shift of 3 hours which differs from all the other values, the period did not seem suitable for the approach. Additionally, the measurements from the 14th of May until the 21st of May were also neglected due to the low correlation of 0.442.
When averaging over all the remaining time spans, a mean travel time variation rate of $0.145 \frac{\%}{^\circ C}$ resulted. This is equal to a velocity variation rate of $-0.145 \frac{\%}{^\circ C}$. This value does not differ significantly from the one estimated before when using the whole period. That means, a separate weekly investigation of the velocity variation is not needed in this case.

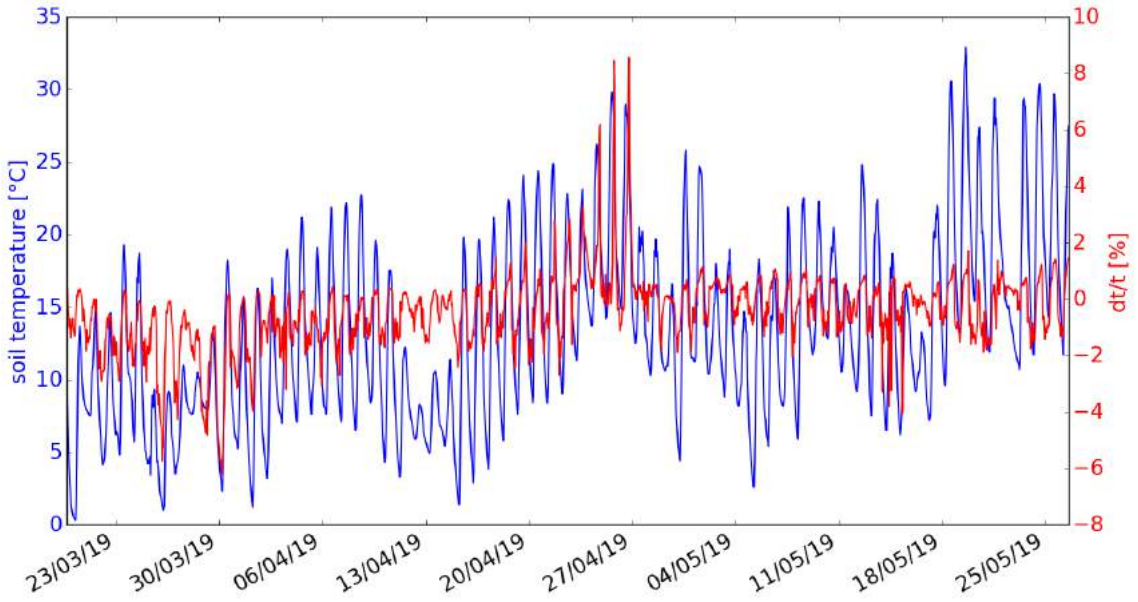

Figure 6.3: Travel time variations $\frac{dt}{t}$ for frequencies between 1 and 4.5 Hz and the soil temperatures measured in Baruth. These data sets were used to determine a mean velocity variation rate per degree Centigrade.

	CC	
frequency band	air temperature	soil temperature
1 - 4.5 Hz	0.569	0.624
4.5 - 8 Hz	0.431	0.531
12 - 16 Hz	0.393	0.436

Table 6.1: Correlation between the particular frequency bands and the temperature data sets.

Week	time shift [h]	CC	a [%/°C]	b
19.03 - 26.03	0	0.614	0.165	-2.668
26.03 - 02.04	0	0.646	0.255	-4.123
02.04 - 09.04	1	0.611	0.102	-2.244
09.04 - 16.04	1	0.714	0.115	-1.564
16.04 - 23.04	0	0.689	0.156	-2.466
23.04 - 30.04	-3	0.702	0.224	-3.063
30.04 - 07.05	1	0.657	0.094	-1.151
07.05 - 14.05	1	0.603	0.111	-1.887
14.05 - 21.05	0	0.442	0.054	-1.210
21.05 - 26.05	0	0.600	0.087	-1.554

Table 6.2: Results of the reduction of the temperature effect using time intervals of one week. The chosen frequencies were between 1 and 4.5 Hz while the temperature was measured in 5 cm depth.

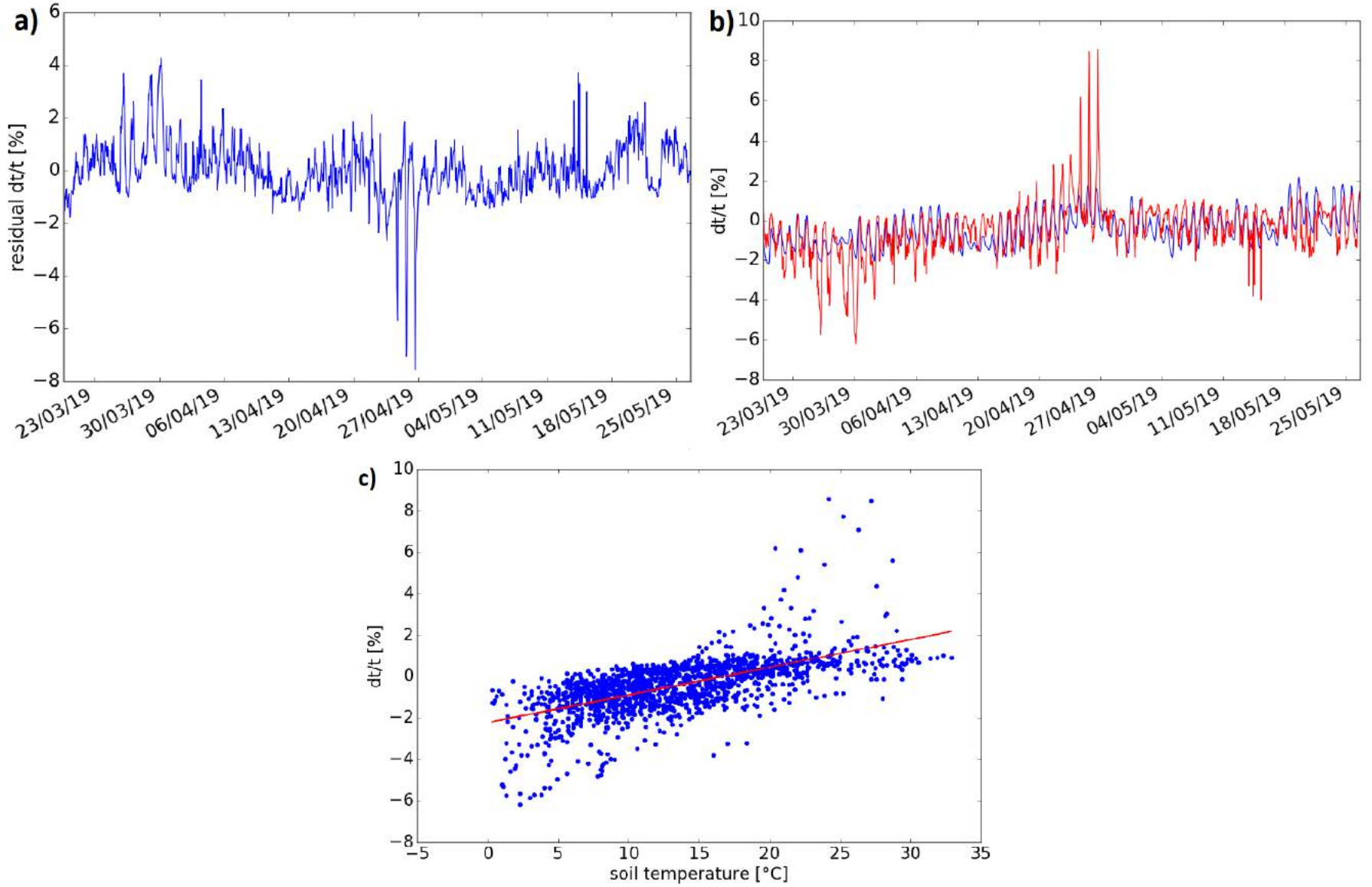

Figure 6.4: Results of the reduction of the temperature effect using the frequency band from 1 to 4.5 Hz and the soil temperatures measured in Baruth. a) Calculated residuals, b) Comparison of the travel time variations before and after the reduction, c) Result of the linear regression (red curve).

7 Discussion

7.1 Comparison between active and passive results

By applying the stretching method on the passive as well as on the active data set, a comparison between both results can be carried out. While the passive results were used to investigate the applicability of the passive image interferometry in this case, the active measurements should be used as a means of confirmation, i.e. as quality control.

To get a first impression if the results show any similarities they are displayed together in Fig. 7.1. The ambient noise measurements which are represented by the dashed lines clearly follow the trend of the active ones (solid lines) for all frequency bands. Even the rise of the highest frequency band for a prestressing force of 101 kN can be identified in both curves.
Nevertheless, a deviation can be found for frequencies between 4.5 and 8 Hz. For the passive measurements, the velocity decreased until a prestressing force of 203 kN was reached. In contrast, the velocity determined by the active measurements dropped even further. Additionally, the velocity changes resulting from the noise data set were slightly larger.
In general, there are no significant differences between the results. The order of magnitude is also the same. Therefore, it can be concluded that the active results confirm the passive ones.

In order to find the most valuable frequency band, the standard deviation was taken into account (see Fig. 7.2). It can be seen that the lowest frequency band is the most stable one, showing the lowest deviation for all applied prestressing forces. The large variations of the frequency band from 8 to 25 Hz can be explained by the chosen frequency range. Because it was selected twice as large as the other two, higher variations were not surprising. However, the jump for a prestressing force of 101 kN is still significant but should be treated as an artefact or outsider. It was not used for further interpretation.

Because the passive results also showed a slightly different behavior for both of the lower frequency bands in particular, the threshold of 0.6 was adapted. This was done to find the most reliable course of the graphs for damage interpretation. By choosing higher values, fewer CCFs were considered but the resulting velocity changes were expected to be more reliable.
When using a higher cross-correlation coefficient limit of 0.7 the middle frequency band approached the lower band (see Fig. 7.3). In addition to that, higher frequencies did not show such a high increase anymore. When using even higher thresholds, the frequency bands did not change further.

Based on the investigation here it can generally be said that the seismic velocity decreased strongly when reducing the prestressing force. With every reduction step, the velocity fell off more. As a prestressing force of 203 kN is reached, the velocity remains more or less stable.

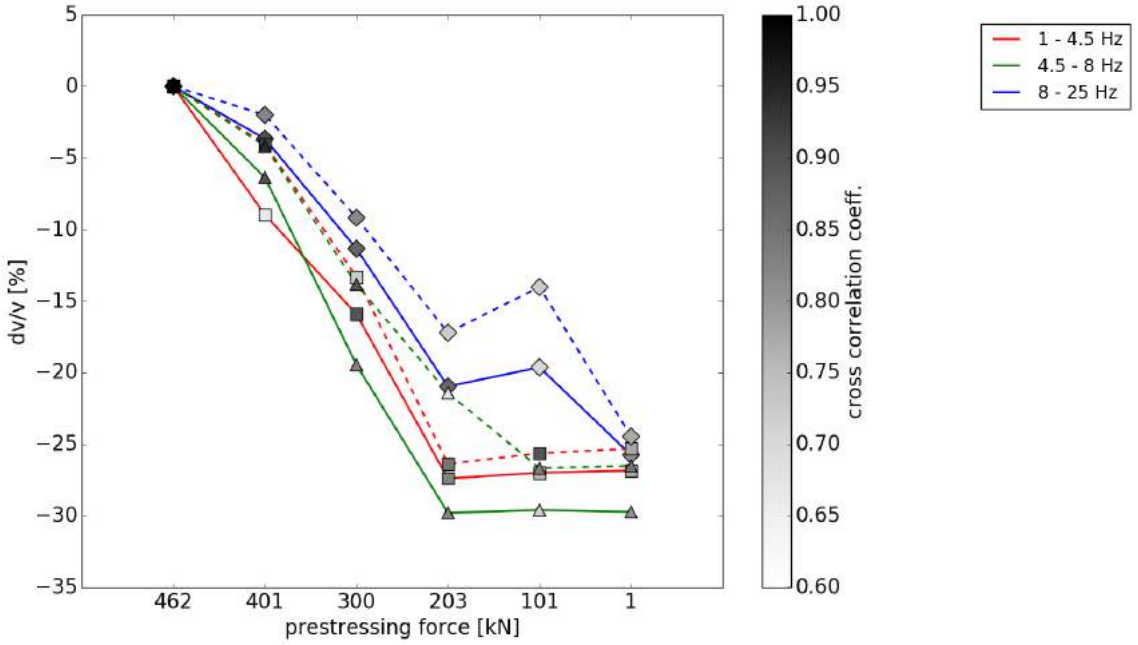

Figure 7.1: Comparison of the stretching results using passive measurements (dashed lines) and active measurements (solid lines). The order of magnitude is the same for all frequency bands.

This behavior is not expected. Studies where the stress on concrete was released showed small changing rates for the first reductions and increasing rates for further stress reduction (e.g. Stähler et al. [2011]). In this case, the velocity behaved contrary. It was striking that when looking at the variation of the eigenfrequency in Fig. 4.3 the same behavior was shown. Zhan et al. [2013] found that a variable frequency content can lead to a bias in the $\frac{dv}{v}$-values when applying the stretching method. They looked at the amplitude spectrum which showed a strong seasonal variation. Here, all frequency bands used, included one of the structure's eigenfrequency. Their standard deviation is 9% (1 - 4.5 Hz), 11% (4.5 - 8 Hz) and 8% (8 - 25 Hz), respectively.
Consequently, an influence due to the selected frequency bands cannot be excluded. In order to find out if the variation of eigenfrequencies has led to a $\frac{dv}{v}$-bias which is included in the determined stretching results, a synthetic test was carried out.

7.2 Synthetic test

The goal of the synthetic was to show if the variation of the eigenfrequencies leads to a bias in the stretching values. A harmonic signal y_{orig} with a frequency of 4.5 Hz was generated. To make the synthetic test comparable to the results previously obtained, the frequency was chosen in-between the lower eigenfrequencies.
Based on y_{orig} two more signals were generated. First, its frequency was shifted by different amounts producing the signal y_{shift}. The size of the changes was chosen so that they represented the variation of the natural frequencies. In a next step, the third signal was produced by stretching the shifted waveform y_{shift}.

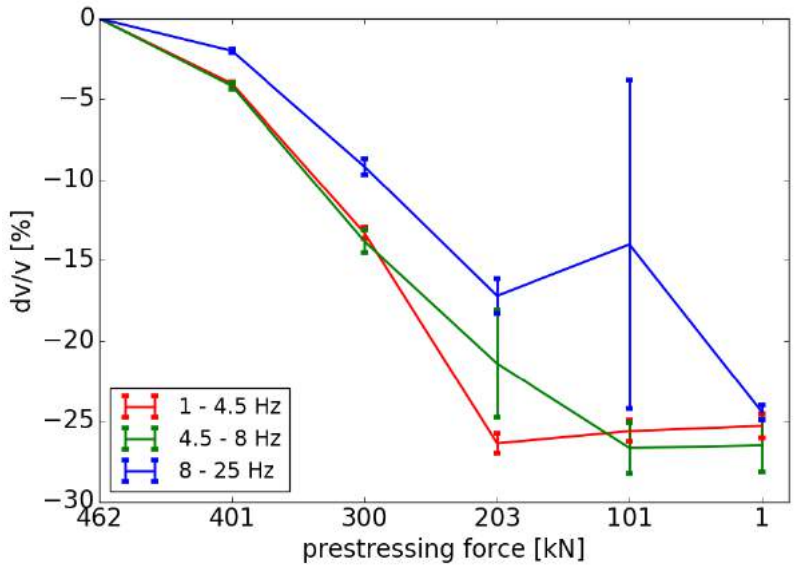

Figure 7.2: Standard deviation of the stretching results estimated by using the passive noise measurements. The lowest frequency band shows the smallest deviations.

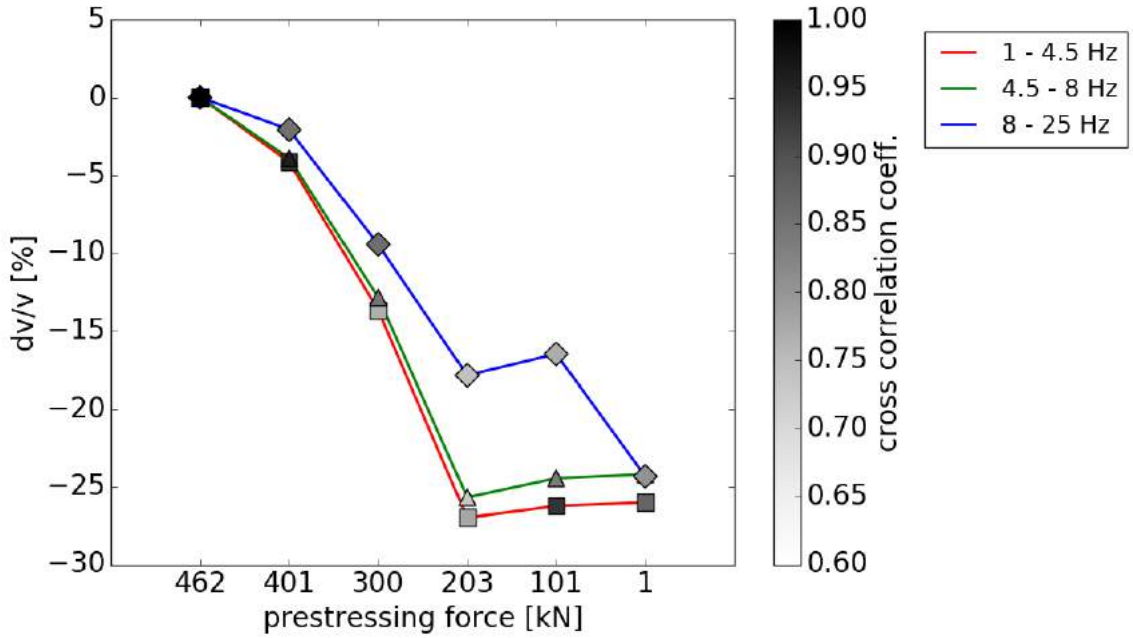

Figure 7.3: Stretching results of the passive measurements when using a threshold CC>0.7. The course of the frequency band from 4.5 to 8 Hz approached the lower band.

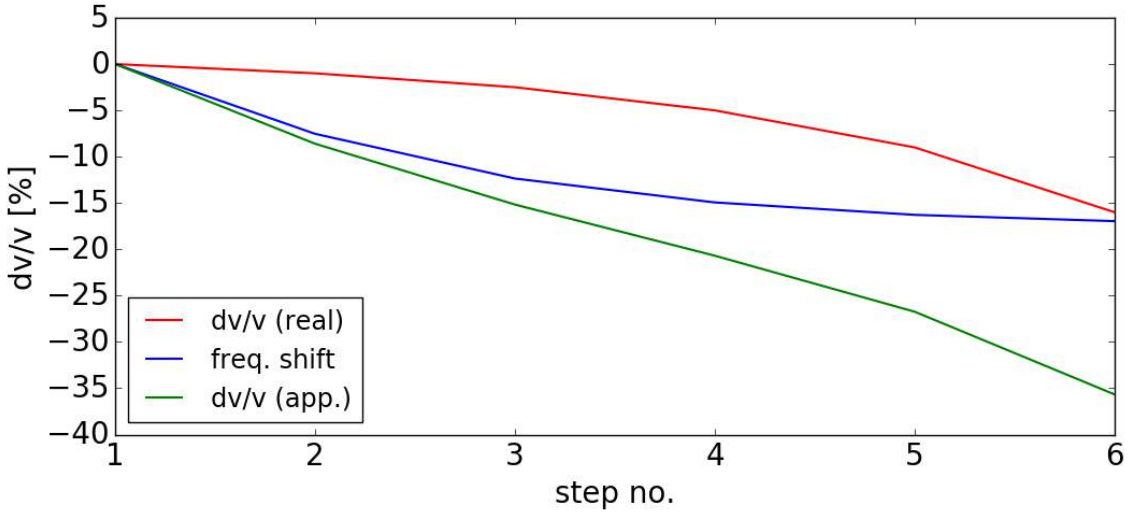

Figure 7.4: Stretching results of the synthetic test, representing a prestress reduction. The original signal was compared with the shifted one but showing velocity changes (blue curve). The original signal was also compared with the signal that was both shifted and stretched, giving an apparent velocity change (green curve). These values did not match the actual velocity changes (red curve).

The stretching was done to simulate a real velocity change. In order to approximate the velocity changes due to a prestress loss, the rate of change was increased for each step.

The frequency shift and the velocity change were done in six steps. These are intended to represent the stepwise reduction of the prestressing force. Figure 7.4 shows the results when applying the stretching algorithm to each of the signals.
First, the original signal y_{orig} was compared with the shifted one, y_{shift} (blue curve). Here, it can clearly be seen that the stretching algorithm gives a velocity change even if just the frequency is shifted. In addition, the stretching results correspond approximately to the chosen shifting values. The course resembles that of the variation of the eigenfrequencies. Next, the stretching method was applied to the signals that were both shifted and stretched in comparison with y_{orig} (green curve). The results here do not match the actual velocity changes (red curve). Instead, an apparent velocity change is displayed. While the course corresponds to the real velocity changes, the values however are too low.

Overall, the synthetic test indicated that a change in frequency definitely leads to a bias in the $\frac{dv}{v}$-values when using the stretching method. The general course of the determined graph is correct, but the values are not.
The problem which was also found by Zhan et al. [2013] is that the stretching affects the phase spectrum as well as the amplitude spectrum. While the velocity changes are included in the phase spectrum, the amplitude spectrum changes also due to the deviation of the natural frequencies. Ultimately, this leads to wrong changes, found by the stretching method. They consist of both frequency changes and actual velocity changes.

7.3 Removal of the velocity bias

Based on the synthetic test, the previously determined relative velocity changes are just apparent ones. In order to estimate the actual changes, the changes due to the variation of the eigenfrequencies had to be removed.
The stretching method is based on the assumption that the frequency content stays constant when only the velocity is changed. Therefore, the apparent velocities are way too high. The synthetic test proved that the apparent velocities are a sum of the changes due to the initial frequency shifts and the actual velocity changes. To remove the bias, the relative frequency changes estimated in section 4.1 can be used. In order to find out if these are suitable to remove the bias, the synthetic test was used again.
By subtracting the relative frequency shifts $\frac{df}{f}$ referring to the initial frequency of 4.5 Hz, the actual velocity changes could be approximated (see Fig. 7.5). Because the stretching also influences the amplitude spectrum, the frequency content was slightly changed again. For this reason the $\frac{df}{f}$-values are higher than the initially applied frequency shift, resulting in velocity changes that are too high.

To finally determine the actual velocity changes inside the BLEIB-structure, the relative frequency changes were subtracted from the stretching results. Here, a threshold of $CC > 0.7$ was chosen referring to the previous investigation.
The corrected relative velocity changes behaved similar to the synthetic test (Fig. 7.6). While the general course of the graphs did not change compared to Fig. 7.3, the values are clearly higher (see table 7.1). Up to a prestress of 203 kN all of the three frequency bands now roughly showed the behavior which was also found by Stähler et al. [2011]. With increasing rate of change the velocity decreased to a maximum of $-7.81\,\%$. Then, the higher frequency band showed a different course than the other two. Because the standard deviation was still much higher for these frequencies, the result of the lower frequencies were assumed to be more reliable (Fig. 7.7). Here, the velocity seemed to increase for prestresses below 203 kN. This is probably an artifact of the bias removal. One would assume that the velocity stayed constant or decreased to a lesser extent. An increase in velocity would theoretically mean a reduced spread in air and therefore the closing of cracks.
In relation to structural health monitoring the prestressing force of 203 kN could possibly be interpreted as a point where the structure should not be loaded further. Based on the behavior of the velocity change a potential collapse cannot be ruled out. Cracks seemed to not open or widen anymore.
When looking at the velocity changes along the structure, displayed in Fig. 7.8, there was no significant difference after the bias removal compared to Fig. 4.12. Nevertheless, a slight curve bend can be seen which probably is related to the formation of cracks. The bending can best be identified in the figure for a prestressing force of 203 kN.

To conclude, the bias removal was performed but required approximation. The exact velocity values should not be overly emphasized as they depend on the applied bias removal. However, the general course can be used as reference point for structural health monitoring. Additionally, the building of cracks in the middle of each structure half could be observed after the removal.

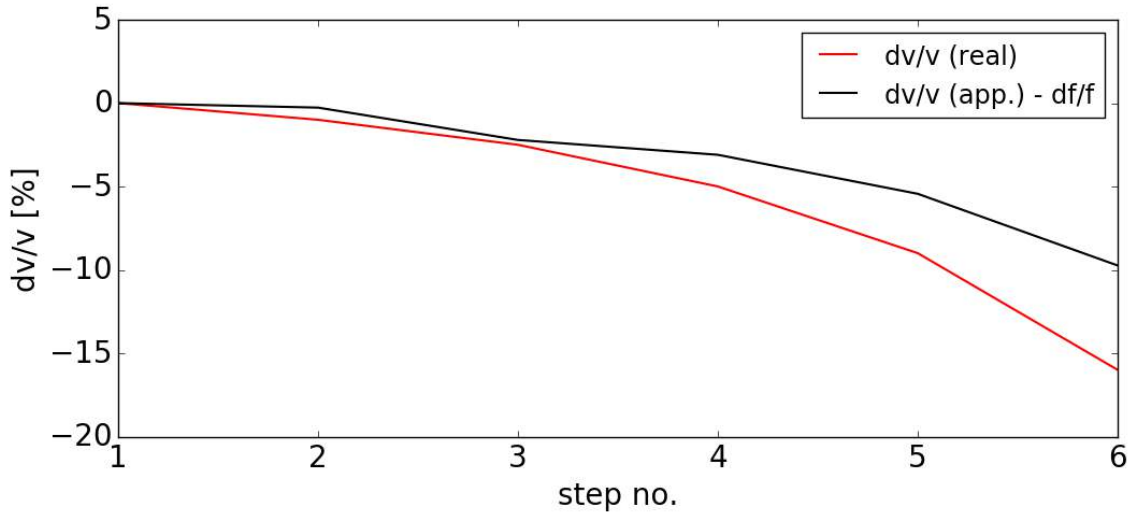

Figure 7.5: Removal of the bias. The actual velocity changes (red curve) are approximated by subtracting the relative frequency changes $\frac{df}{f}$ from the apparent velocity changes (solid black curve).

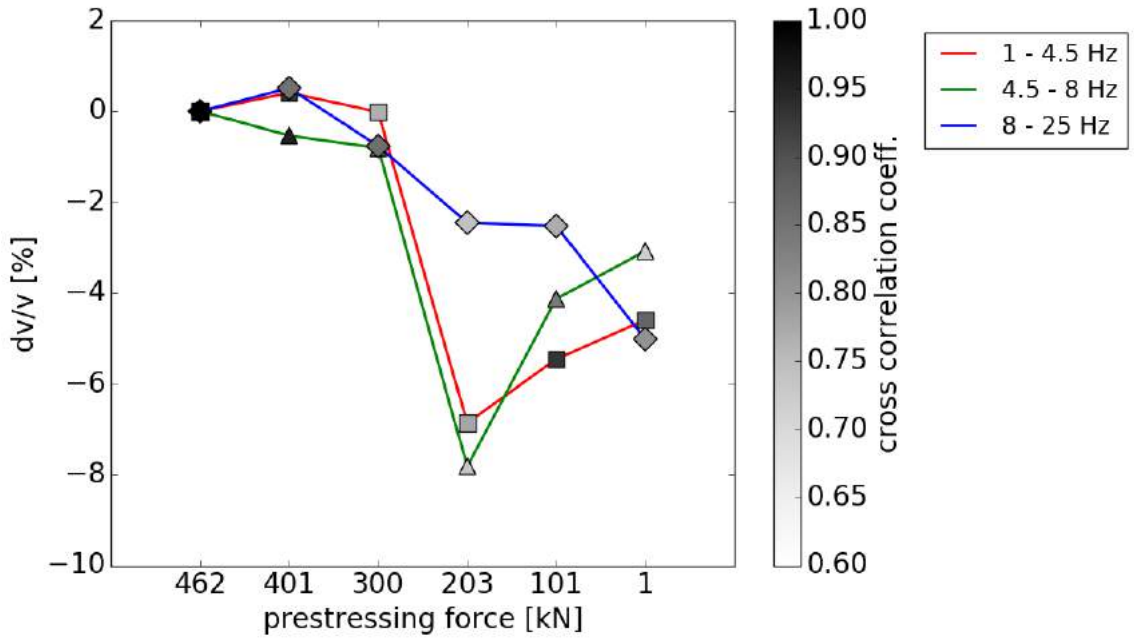

Figure 7.6: Corrected stretching results by subtracting the relative frequency shift. The general course did not change whereby the values are clearly higher.

prestressing force	frequency band					
	1 - 4.5 Hz		4.5 - 8 Hz		8 - 25 Hz	
	cross-corr. coeff.	dv/v	cross-corr. coeff.	dv/v	cross-corr. coeff.	dv/v
462 kN	1	0 %	1	0 %	1	0 %
401 kN	0.93	0.41 %	0.96	- 0.53 %	0.85	- 0.51 %
300 kN	0.77	- 0.02 %	0.85	- 0.80 %	0.86	- 0.76 %
203 kN	0.78	- 6.85 %	0.73	- 7.81 %	0.74	- 2.45 %
101 kN	0.93	- 5.46 %	0.84	- 4.12 %	0.77	- 2.53 %
1 kN	0.87	- 4.59 %	0.72	- 3.07 %	0.80	- 5.01 %

Table 7.1: Corrected stretching results by subtracting three quarters of the relative frequency shift. The correlation coefficients are slightly higher because a threshold of $CC > 0.7$ was used. Because of the bias removal, the velocity changes are clearly higher compared to the apparent velocities before.

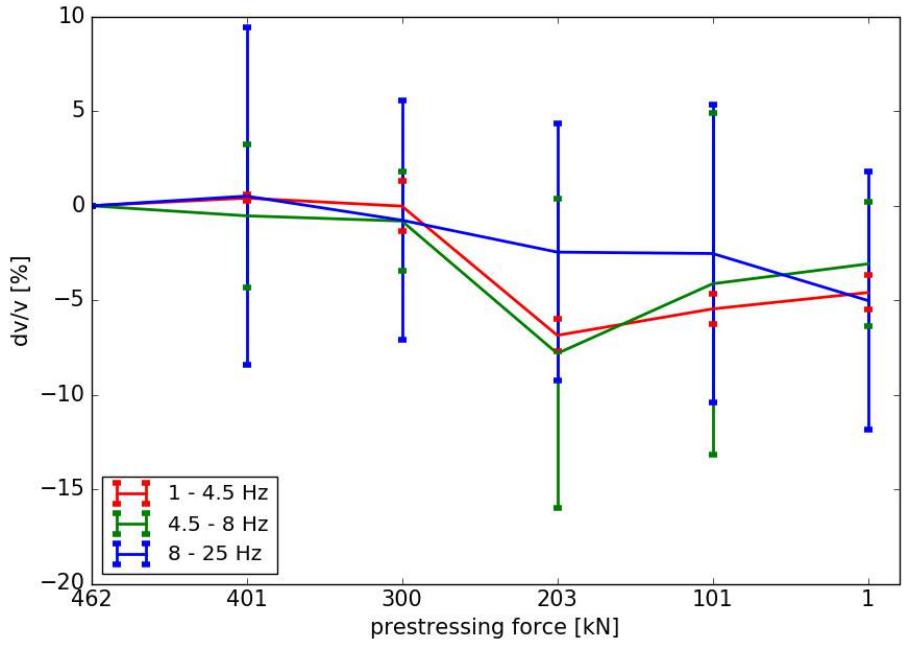

Figure 7.7: Standard deviation of the stretching results after the bias removal. The higher frequencies still shows the largest deviations, while the lowest frequency band is the most stable one.

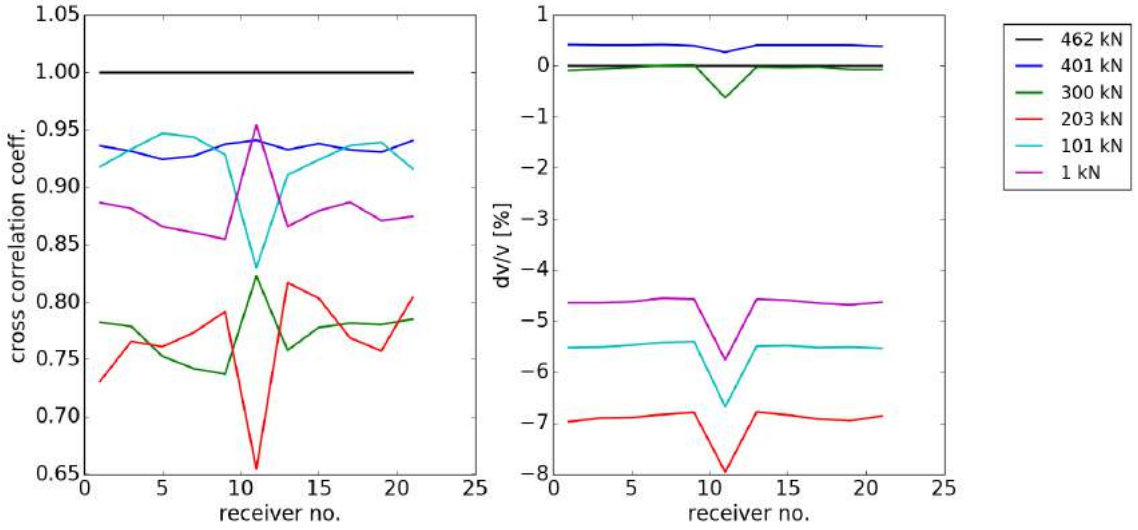

Figure 7.8: Relative velocity change along the structure after the bias removal. The pillar's location can be easily identified. Both structure halves behave similar.

7.4 Comparison of temperature results with previous studies

Several studies previously explored on the estimation of the temperature's influence on stretching results before. These studies also determined a velocity variation rate per degree. These values can be compared with the ones estimated in section 6.3. However, it must be taken into account that there are differences in the measurement objects or the used signals, to name just two examples. Because of that, deviations in the values were expected.
In this study, the variation rate determined for the whole period of two months was around $a = -0.134\,\frac{\%}{^\circ\mathrm{C}}$.

The four following mean variation rates can be found in other studies:

Salvermoser [2014]: $a = -0.064\,\frac{\%}{^\circ\mathrm{C}}$
Marten [2019]: $a = -0.138\,\frac{\%}{^\circ\mathrm{C}}$
Larose et al. [2006]: $a = -0.15\,\frac{\%}{^\circ\mathrm{C}}$
Niederleithinger and Wunderlich [2013]: $a = -0.06\,\frac{\%}{^\circ\mathrm{C}}$

Salvermoser [2014] and Marten [2019] investigated a concrete bridge located in Northern Bavaria using vibration signals. These were induced by cars crossing the structure. Whereas the variation rate determined by Marten [2019] fits very well with the variation rate estimated in this study, the rate determined by Salvermoser [2014] is too low. Their difference can be explained by the temperature data sets they used.
Whereas Salvermoser [2014] worked with air temperatures, Marten [2019] used temperatures measured in a box girder underneath the bridge's deck. The temperatures used in this study were measured in a depth of 5 cm below ground. Therefore, the data set is more comparable to the one used by Marten [2019] which possibly explains the greater similarity.

The value estimated by Larose et al. [2006] also fits well. Larose et al. [2006] investigated a concrete building was investigated by using a vibration source emitting frequencies between 20 to 2000 Hz. Again, the temperatures used were measured inside the concrete, showing fewer variations than the outside air temperatures.

Niederleithinger and Wunderlich [2013] did not examine a concrete structure, but a concrete sample. In small steps the concrete was exposed to a temperature increase from 0 to 50 °C, showing a velocity decrease of more than 3%. The resulting velocity variation rate is less than half the one determined in this study. The size of the measurement object can possibly explain the difference as well as again the fact that temperatures were measured outside of the concrete.

The synthetic test in the previous section showed that the shift of the eigenfrequency can lead to a bias in the $\frac{dv}{v}$-values. Because the here investigated frequency band also includes an eigenfrequency, this could perhaps explain the rather low correlation of 0.624. Other studies showed correlations above 0.9 (e.g. Marten [2019]). In order to exclude a possible bias the behavior of the first eigenfrequency during the measurement period was examined.
Figure 7.9 shows the temporal variation of the structure's first eigenfrequency. The standard deviation gave a value of approximately 0.07 Hz which is about 2%. It can be seen very well that the frequency remained stable after the reattachment on the 27th of April. By just using this time span a standard deviation around 0.03 Hz ($\approx$ 1%) was found.

The deviation was significantly lower than the one found by Zhan et al. [2013]. It was also just a tenth of the change that could be observed when the prestressing force was reduced. Because of this, there is no reason to assume that the variation of the natural frequency significantly influenced the stretching results.
To be safe, only the measurements after the reattachment can be considered. By averaging the last four variation rates given in table 6.2, a value of $-0.087\,\frac{\%}{°C}$ resulted. This one fits well with the velocity variation rates given in the study of Salvermoser [2014] and Niederleithinger and Wunderlich [2013]. However, there was still a low correlation between temperature and velocity changes. These can be possibly attributed to the distance between the BLEIB-structure and Baruth. Also, the difference in the heat conduction of soil and concrete due to temperature changes cannot be neglected.

Overall, it can be said that it was possible to determine a velocity variation rate per degree Centigrade. In order to decide which is the most valuable one, another temperature data set measured inside the structure is required. However, all values should be used carefully. A comparison with other studies showed that the location where the temperatures were measured is an important factor which influenced the variation rate a lot. The size of the measurement object or the coupling of the sensors can also influence the result.
Therefore, a variation rate determined for one specific concrete structure should not be used as a general assumption for other structures.

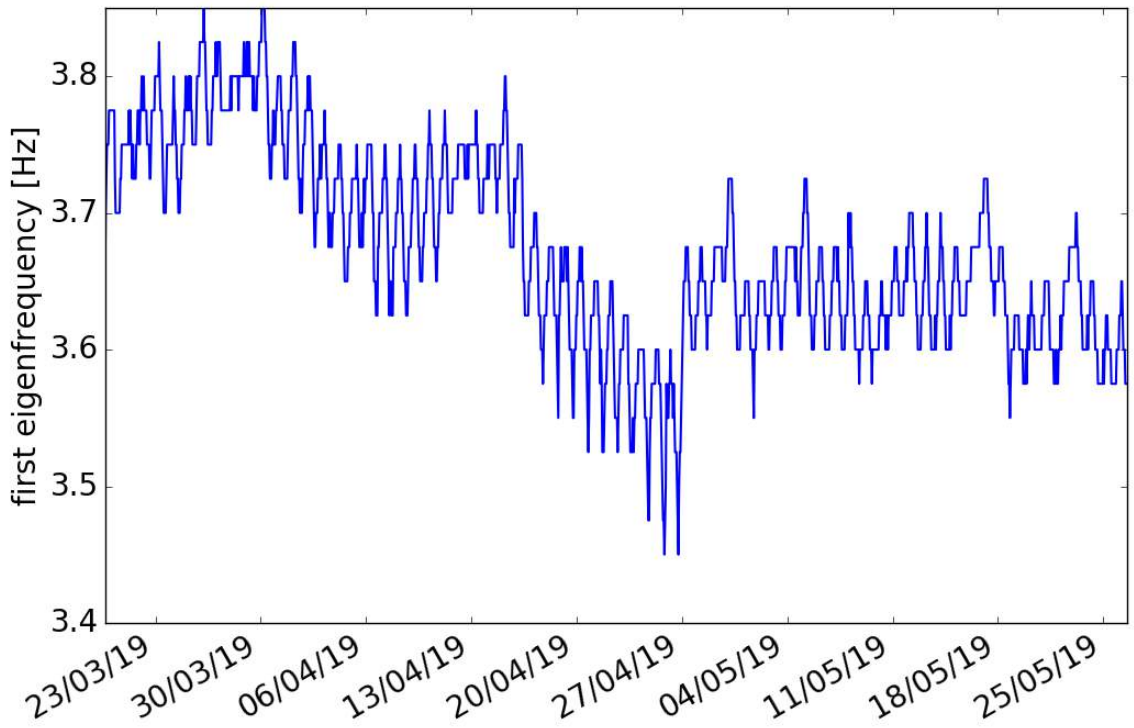

Figure 7.9: Temporal variations of the first eigenfrequency. After the reattachment on the 27th of April, the eigenfrequency stays more stable.

8 Conclusion and outlook

This thesis was carried out in order to investigate if the method of passive image interferometry is suitable to detect prestress changes in a prestressed concrete structure. For this purpose, a measurement was done on a test structure with a built-in pre-tensioning system. Ambient seismic noise was used as a source which was recorded by 24 geophones. The prestress was released in steps of 100 kN. To confirm the obtained results an active measurement was additionally carried out.

By using the stretching method, strong negative velocity changes were observed. Three frequency bands were investigated separately. The lowest one between 1 and 4.5 Hz was chosen to be the most suitable one, showing results with the lowest standard deviation.
Because the eigenfrequencies of the structure had to be used due to the low noise level, a bias superimposed the data. After the removal of the bias, the highest velocity change seen was around -7.81% for a prestress reduction of 259 kN. Related to the detection of damages, the opening of new cracks and the widening of existing ones is highly expected until this stage. For further reductions of the prestressing force, the velocity did not decrease further. A change of the breaking behavior can be suspected.
The localization of damages is still challenging in part due to the untraceable path of the scattered waves. The only statement that can be made is that most damage occurred at the most curved positions. This is where the middle pillar is located and in the middle of each structure half. A difference between both structure halves could not be found, i.e. the northern structure half behaved like the southern one.

In general, the velocity changes received by using the active data set confirmed the passive stretching results. For that reason, ambient noise can be treated as a sufficient source for monitoring tasks. Nevertheless, the investigation showed that a particularly low noise level should be avoided. Using the eigenfrequencies for PII is possible but can only give a rough estimation of the velocity changes.

Because the measurement was carried out in a very short time span, there was no need to reduce a temperature influence. For longer time spans, the temperature effect has to be removed from the estimated velocity changes. In case of this study, a velocity variation rate per degree Centigrade was determined. Because of the bad correlation with the temperature data measured in Baruth, two values resulted. Taking the whole period of two months into account, a variation rate of $-0.134\,\frac{\%}{^\circ\mathrm{C}}$ was determined. Using just the four weeks after the reattachment of the sensors a value of $-0.087\,\frac{\%}{^\circ\mathrm{C}}$ resulted. Both variation rates matched previous studies. In order to find the most suitable one, a temperature data set should be recorded inside the structure.

Overall, it can be concluded that PII can be used to monitor prestress loss in concrete structures. However, before it should be used for real monitoring tasks, some further investigations are advisable.
For further similar investigations on the BLEIB-structure, some adjustments should be made. First, an appropriate temperature data set is needed, preferably measured inside the structure. Additionally, the coupling of the sensors could be improved in order to

avoid a reattachment. Furthermore, the low noise level is a problem which has to be solved. However, for most of structures which could be investigated later on the noise level is probably sufficient. A deformation measurement could also be a helpful tool to better interpret the behavior after a prestress of 203 kN was applied.
Because the structure was rather small, a long term measurement carried out on a real-size pre-stressed concrete structure would also be interesting. A valuable feature would be cars crossing the structure, producing a stable noise level. However, a prestress system would be needed in order to observe its changes.

Appendices

A Measurement schedule 19th of March 2019

Time	prestress [kN]	Active	Passive	Comments	Filenumber
09:26	462			Start of Measurement	1
09:31 - 09:35	462	x		active measurement between sensor 20 and 21 (near 20)	6 - 9
09:51 - 10:11	462		x	20 min. ambient noise measurement	25 - 44
10:13				pretension is reduced to 401 kN	
10:20	401				52
10:24 - 10:32	401	x		active measurement	56 - 63
10:33 - 10:53	401		x	20 min. ambient noise measurement	65 - 84
11:00				pretension is reduced to 300 kN	
11:01	300				91
11:16 - 11:25	300	x		active measurement	105 - 113
11:26 - 11:46	300		x	20 min. ambient noise measurment	115 - 134
11:50 - 12:00	300	x		active measurement is repeated due to instrumental problems	137 - 146
12:02				pretension is reduced to 203 kN	
12:06	203				152
12:07 - 12:18	203	x		active measurement	153 - 163
12:20 - 12:40	203		x	20 min. ambient noise measurement	165 - 184
12:45				pretension is reduced to 101 kN	
12:50	101				193
12:51 - 13:02	101	x		active measurement	194 - 204
13:03 - 13:23	101		x	explosion around 13:08 (file 210)	205 - 224
13:24				pretension is reduced to 1 kN	
13:27	1				228
13:30 - 13:39	1	x		active measurement	230 - 239
13:40 - 14:00	1		x	20 min. ambient noise measurement	241 - 260
14:02 - 14:36	360-400			changing of pretension from 360 kN to 400 kN in steps of 10 kN	260 - 292
14:37 - 14:49	460	x		active measurement	293 - 305
14:55	460			end of measurement	310
15:02	454		x	start of long term measurement	1 (long term)

Table A.1: Measurement schedule on the 19th of March 2019.

B Natural frequency trend

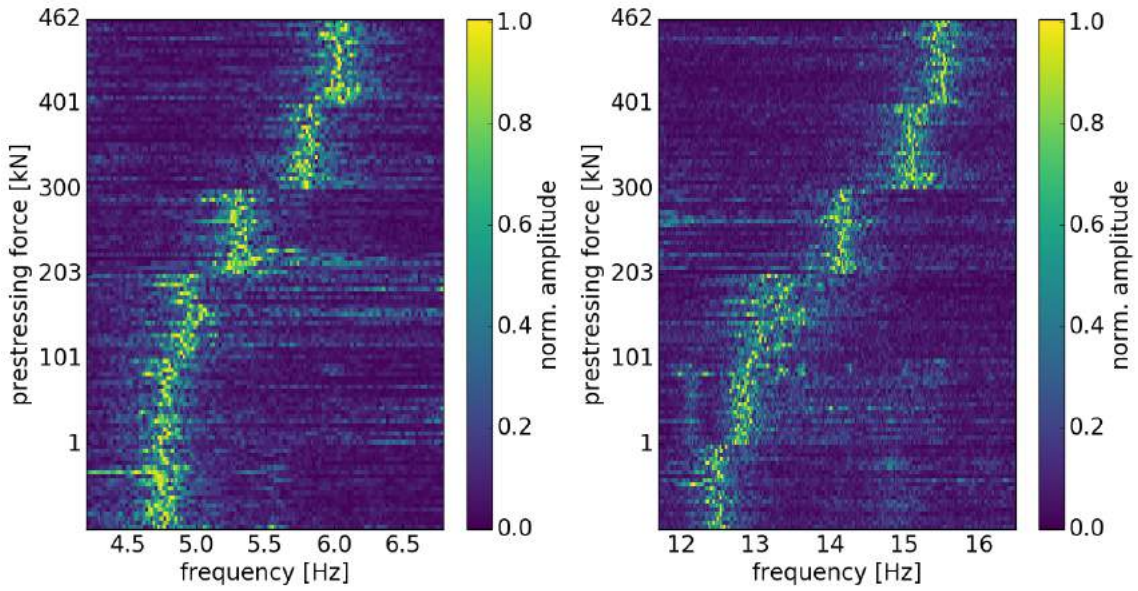

Figure B.1: Trend of the second natural frequency at 6.05 Hz (left) and the third natural frequency at 15.5 Hz (right) with decreasing prestressing force.

C Time windows used for stretching method

Receiver pair		Frequency band (start time [s] - end time [s])					
		passive measurements			active measurements		
		1 - 4.5 Hz	4.5 - 8 Hz	8 - 25 Hz	1 - 4.5 Hz	4.5 - 8 Hz	8 - 25 Hz
0	1	1.26 - 12.872	1.316 - 8.44	0.268 - 6.132	1.26 - 7.34	1.528 - 5.872	0.272 - 3.908
0	2	1.26 - 13.088	1.532 - 8.656	0.268 - 6.132	1.26 - 7.34	1.524 - 5.868	0.272 - 3.908
0	3	1.26 - 13.088	1.532 - 8.656	0.268 - 6.132	1.26 - 7.34	1.948 - 6.292	0.272 - 3.908
0	4	1.26 - 13.088	1.532 - 8.656	0.348 - 6.212	1.256 - 7.336	1.952 - 6.296	0.272 - 3.908
0	5	1.26 - 13.088	1.532 - 8.656	0.344 - 6.208	1.256 - 7.336	1.952 - 6.296	0.304 - 3.94
0	6	1.264 - 13.088	1.532 - 8.656	0.232 - 6.096	1.26 - 7.34	1.736 - 6.8	0.232 - 3.868
0	7	1.264 - 13.088	1.532 - 8.656	0.232 - 6.096	1.26 - 7.34	1.736 - 6.8	0.232 - 3.868
0	8	1.264 - 12.884	1.328 - 8.452	0.232 - 6.096	1.264 - 7.344	1.736 - 6.8	0.232 - 3.868
0	9	1.264 - 12.888	1.332 - 8.456	0.304 - 6.168	1.268 - 7.348	1.744 - 6.088	0.312 - 3.948
0	10	1.268 - 12.896	1.34 - 8.464	0.308 - 6.172	1.264 - 7.344	1.744 - 6.088	0.312 - 3.948
0	11	1.436 - 12.884	1.328 - 8.452	0.508 - 6.372	1.452 - 7.532	1.944 - 6.288	0.44 - 4.076
0	12	1.436 - 12.88	1.324 - 8.448	0.5 - 6.364	1.456 - 7.536	1.944 - 6.288	0.44 - 4.076
0	13	1.436 - 12.88	1.324 - 8.448	0.436 - 6.3	1.46 - 7.54	1.524 - 5.868	0.44 - 4.076
0	14	1.436 - 12.88	1.324 - 8.448	0.436 - 6.3	1.456 - 7.536	1.524 - 5.868	0.44 - 4.076
0	15	1.436 - 12.88	1.324 - 8.448	0.436 - 6.3	1.46 - 7.54	1.524 - 5.868	0.44 - 4.076
0	16	1.44 - 13.088	1.532 - 8.656	0.436 - 6.3	1.46 - 7.54	1.944 - 6.288	0.444 - 4.08
0	17	1.44 - 13.088	1.532 - 8.656	0.464 - 6.328	1.46 - 7.54	1.944 - 6.288	0.392 - 4.028
0	18	1.44 - 13.084	1.528 - 8.652	0.464 - 6.328	1.464 - 7.544	1.524 - 5.868	0.396 - 4.032
0	19	1.44 - 13.084	1.528 - 8.652	0.464 - 6.328	1.468 - 7.548	1.732 - 6.076	0.396 - 4.032
0	20	1.44 - 13.084	1.528 - 8.652	0.464 - 6.328	1.468 - 7.548	1.944 - 6.288	0.4 - 4.036
0	21	1.44 - 13.088	1.532 - 8.656	0.464 - 6.328	1.468 - 7.548	1.736 - 6.8	0.4 - 4.036
0	22	1.756 - 12.652	1.096 - 8.22	0.556 - 6.42	1.456 - 7.536	2.376 - 7.72	0.4 - 4.036
1	2	1.264 - 12.876	1.32 - 8.444	0.268 - 6.132	1.26 - 7.34	1.528 - 5.872	0.272 - 3.908
1	3	1.26 - 13.088	1.532 - 8.656	0.268 - 6.132	1.256 - 7.336	1.948 - 6.292	0.272 - 3.908
1	4	1.264 - 13.088	1.532 - 8.656	0.348 - 6.212	1.256 - 7.336	1.952 - 6.296	0.272 - 3.908
1	5	1.264 - 13.088	1.532 - 8.656	0.34 - 6.204	1.256 - 7.336	1.952 - 6.296	0.308 - 3.944
1	6	1.264 - 13.088	1.532 - 8.656	0.236 - 6.1	1.256 - 7.336	1.952 - 6.296	0.308 - 3.944
1	7	1.264 - 13.088	1.532 - 8.656	0.232 - 6.096	1.26 - 7.34	1.736 - 6.8	0.308 - 3.944
1	8	1.264 - 13.088	1.532 - 8.656	0.232 - 6.096	1.26 - 7.34	1.736 - 6.8	0.312 - 3.948
1	9	1.264 - 12.888	1.332 - 8.456	0.232 - 6.096	1.264 - 7.344	1.736 - 6.8	0.312 - 3.948
1	10	1.268 - 12.896	1.34 - 8.464	0.308 - 6.172	1.264 - 7.344	1.96 - 6.304	0.312 - 3.948
1	11	1.436 - 13.508	1.952 - 9.076	0.508 - 6.372	1.448 - 7.528	1.944 - 6.288	0.44 - 4.076
1	12	1.436 - 12.884	1.328 - 8.452	0.5 - 6.364	1.452 - 7.532	1.944 - 6.288	0.44 - 4.076
1	13	1.44 - 12.884	1.328 - 8.452	0.436 - 6.3	1.456 - 7.536	1.528 - 5.872	0.44 - 4.076
1	14	1.436 - 12.88	1.324 - 8.448	0.436 - 6.3	1.456 - 7.536	1.944 - 6.288	0.44 - 4.076
1	15	1.44 - 13.088	1.532 - 8.656	0.432 - 6.296	1.46 - 7.54	1.944 - 6.288	0.44 - 4.076
1	16	1.44 - 13.088	1.532 - 8.656	0.436 - 6.3	1.46 - 7.54	1.944 - 6.288	0.444 - 4.08
1	17	1.44 - 13.088	1.532 - 8.656	0.464 - 6.328	1.46 - 7.54	1.944 - 6.288	0.392 - 4.028
1	18	1.44 - 13.088	1.532 - 8.656	0.464 - 6.328	1.464 - 7.544	1.944 - 6.288	0.4 - 4.036
1	19	1.44 - 13.084	1.528 - 8.652	0.464 - 6.328	1.464 - 7.544	1.944 - 6.288	0.4 - 4.036
1	20	1.44 - 13.088	1.532 - 8.656	0.464 - 6.328	1.464 - 7.544	1.948 - 6.292	0.4 - 4.036
1	21	1.444 - 13.088	1.532 - 8.656	0.464 - 6.328	1.464 - 7.544	1.948 - 6.292	0.4 - 4.036
1	22	1.752 - 12.656	1.1 - 8.224	0.556 - 6.42	1.452 - 7.532	2.376 - 7.72	0.476 - 4.112
2	3	1.264 - 13.088	1.532 - 8.656	0.268 - 6.132	1.256 - 7.336	1.952 - 6.296	0.272 - 3.908
2	4	1.264 - 13.088	1.532 - 8.656	0.348 - 6.212	1.252 - 7.332	1.952 - 6.296	0.272 - 3.908
2	5	1.264 - 13.088	1.532 - 8.656	0.352 - 6.216	1.252 - 7.332	1.952 - 6.296	0.304 - 3.94
2	6	1.264 - 13.088	1.532 - 8.656	0.236 - 6.1	1.256 - 7.336	1.952 - 6.296	0.232 - 3.868
2	7	1.264 - 13.088	1.532 - 8.656	0.232 - 6.096	1.26 - 7.34	1.74 - 6.084	0.232 - 3.868
2	8	1.264 - 13.088	1.532 - 8.656	0.232 - 6.096	1.26 - 7.34	1.736 - 6.8	0.232 - 3.868
2	9	1.264 - 13.092	1.536 - 8.66	0.232 - 6.096	1.264 - 7.344	1.736 - 6.8	0.312 - 3.948
2	10	1.268 - 12.896	1.34 - 8.464	0.236 - 6.1	1.26 - 7.34	1.96 - 6.304	0.312 - 3.948
2	11	1.436 - 13.504	1.948 - 9.072	0.508 - 6.372	1.448 - 7.528	1.948 - 6.292	0.44 - 4.076
2	12	1.436 - 13.088	1.532 - 8.656	0.5 - 6.364	1.452 - 7.532	1.948 - 6.292	0.44 - 4.076
2	13	1.44 - 12.884	1.328 - 8.452	0.436 - 6.3	1.456 - 7.536	1.944 - 6.288	0.44 - 4.076
2	14	1.436 - 12.88	1.324 - 8.448	0.432 - 6.296	1.456 - 7.536	1.944 - 6.288	0.44 - 4.076
2	15	1.44 - 13.088	1.532 - 8.656	0.432 - 6.296	1.456 - 7.536	1.944 - 6.288	0.44 - 4.076
2	16	1.44 - 13.296	1.74 - 8.864	0.436 - 6.3	1.456 - 7.536	1.948 - 6.292	0.444 - 4.08

Table C.1: Used time windows for the stretching method.

2	17	1.44	-	13.088	1.532	-	8.656	0.464	-	6.328	1.456	-	7.536	1.948	-	6.292	0.312	-	3.948
2	18	1.44	-	13.088	1.532	-	8.656	0.464	-	6.328	1.46	-	7.54	1.944	-	6.288	0.4	-	4.036
2	19	1.44	-	13.088	1.532	-	8.656	0.464	-	6.328	1.464	-	7.544	1.944	-	6.288	0.4	-	4.036
2	20	1.44	-	13.088	1.532	-	8.656	0.464	-	6.328	1.464	-	7.544	1.948	-	6.292	0.48	-	4.116
2	21	1.444	-	13.088	1.532	-	8.656	0.464	-	6.328	1.46	-	7.54	2.16	-	6.504	0.48	-	4.116
2	22	1.752	-	12.66	1.104	-	8.228	0.556	-	6.42	1.448	-	7.528	2.376	-	7.72	0.476	-	4.112
3	4	1.264	-	13.088	1.532	-	8.656	0.268	-	6.132	1.256	-	7.336	1.952	-	6.296	0.272	-	3.908
3	5	1.264	-	13.088	1.532	-	8.656	0.352	-	6.216	1.252	-	7.332	1.952	-	6.296	0.304	-	3.94
3	6	1.264	-	13.092	1.536	-	8.66	0.56	-	6.424	1.256	-	7.336	1.952	-	6.296	0.308	-	3.944
3	7	1.264	-	13.508	1.952	-	9.076	0.232	-	6.096	1.26	-	7.34	1.736	-	6.8	0.308	-	3.944
3	8	1.264	-	13.508	1.952	-	9.076	0.232	-	6.096	1.264	-	7.344	1.736	-	6.8	0.232	-	3.868
3	9	1.268	-	13.092	1.536	-	8.66	0.232	-	6.096	1.264	-	7.344	1.736	-	6.8	0.312	-	3.948
3	10	1.268	-	13.308	1.752	-	8.876	0.232	-	6.096	1.264	-	7.344	1.96	-	6.304	0.312	-	3.948
3	11	1.436	-	13.3	1.744	-	8.868	0.508	-	6.372	1.448	-	7.528	1.944	-	6.288	0.44	-	4.076
3	12	1.436	-	13.296	1.74	-	8.864	0.5	-	6.364	1.452	-	7.532	1.944	-	6.288	0.44	-	4.076
3	13	1.44	-	13.296	1.74	-	8.864	0.432	-	6.296	1.456	-	7.536	1.94	-	6.284	0.44	-	4.076
3	14	1.44	-	13.084	1.528	-	8.652	0.432	-	6.296	1.456	-	7.536	1.94	-	6.284	0.44	-	4.076
3	15	1.44	-	13.088	1.532	-	8.656	0.432	-	6.296	1.46	-	7.54	1.944	-	6.288	0.44	-	4.076
3	16	1.44	-	13.296	1.74	-	8.864	0.436	-	6.3	1.46	-	7.54	1.944	-	6.288	0.444	-	4.08
3	17	1.44	-	13.296	1.74	-	8.864	0.536	-	6.4	1.46	-	7.54	1.944	-	6.288	0.312	-	3.948
3	18	1.44	-	13.088	1.532	-	8.656	0.464	-	6.328	1.464	-	7.544	1.944	-	6.288	0.4	-	4.036
3	19	1.44	-	13.088	1.532	-	8.656	0.464	-	6.328	1.464	-	7.544	1.944	-	6.288	0.396	-	4.032
3	20	1.44	-	13.088	1.532	-	8.656	0.464	-	6.328	1.464	-	7.544	1.944	-	6.288	0.4	-	4.036
3	21	1.444	-	13.088	1.532	-	8.656	0.464	-	6.328	1.464	-	7.544	1.948	-	6.292	0.4	-	4.036
3	22	1.752	-	12.66	1.104	-	8.228	0.556	-	6.42	1.452	-	7.532	2.376	-	7.72	0.4	-	4.036
4	5	1.26	-	13.088	1.532	-	8.656	0.564	-	6.428	1.256	-	7.336	1.948	-	6.292	0.304	-	3.94
4	6	1.264	-	13.088	1.532	-	8.656	0.448	-	6.312	1.26	-	7.34	1.736	-	6.8	0.228	-	3.864
4	7	1.264	-	13.088	1.532	-	8.656	0.436	-	6.3	1.26	-	7.34	1.736	-	6.8	0.228	-	3.864
4	8	1.264	-	13.088	1.532	-	8.656	0.232	-	6.096	1.264	-	7.344	1.732	-	6.076	0.228	-	3.864
4	9	1.264	-	13.092	1.536	-	8.66	0.232	-	6.096	1.268	-	7.348	1.736	-	6.8	0.228	-	3.864
4	10	1.268	-	13.308	1.752	-	8.876	0.3	-	6.164	1.264	-	7.344	1.744	-	6.088	0.312	-	3.948
4	11	1.436	-	13.3	1.744	-	8.868	0.508	-	6.372	1.452	-	7.532	1.94	-	6.284	0.356	-	3.992
4	12	1.436	-	13.296	1.74	-	8.864	0.5	-	6.364	1.456	-	7.536	1.944	-	6.288	0.356	-	3.992
4	13	1.44	-	13.296	1.74	-	8.864	0.5	-	6.364	1.456	-	7.536	1.94	-	6.284	0.356	-	3.992
4	14	1.436	-	13.084	1.528	-	8.652	0.5	-	6.364	1.456	-	7.536	1.728	-	6.072	0.356	-	3.992
4	15	1.44	-	13.088	1.532	-	8.656	0.5	-	6.364	1.46	-	7.54	1.728	-	6.072	0.36	-	3.996
4	16	1.44	-	13.296	1.74	-	8.864	0.696	-	6.56	1.46	-	7.54	1.94	-	6.284	0.444	-	4.08
4	17	1.44	-	13.292	1.736	-	8.68	0.536	-	6.4	1.46	-	7.54	1.944	-	6.288	0.312	-	3.948
4	18	1.44	-	13.088	1.532	-	8.656	0.536	-	6.4	1.464	-	7.544	1.728	-	6.072	0.312	-	3.948
4	19	1.44	-	13.088	1.532	-	8.656	0.536	-	6.4	1.468	-	7.548	1.728	-	6.072	0.396	-	4.032
4	20	1.44	-	13.088	1.532	-	8.656	0.536	-	6.4	1.468	-	7.548	1.732	-	6.076	0.396	-	4.032
4	21	1.444	-	13.088	1.532	-	8.656	0.536	-	6.4	1.468	-	7.548	1.944	-	6.288	0.396	-	4.032
4	22	1.752	-	12.66	1.104	-	8.228	0.556	-	6.42	1.46	-	7.54	2.372	-	6.716	0.396	-	4.032
5	6	1.264	-	13.092	1.536	-	8.66	0.268	-	6.132	1.26	-	7.34	1.736	-	6.8	0.272	-	3.908
5	7	1.264	-	13.092	1.536	-	8.66	0.268	-	6.132	1.264	-	7.344	1.736	-	6.8	0.272	-	3.908
5	8	1.264	-	13.088	1.532	-	8.656	0.268	-	6.132	1.264	-	7.344	1.736	-	6.8	0.272	-	3.908
5	9	1.268	-	13.304	1.748	-	8.872	0.268	-	6.132	1.268	-	7.348	1.736	-	6.8	0.272	-	3.908
5	10	1.268	-	13.308	1.752	-	8.876	0.272	-	6.136	1.268	-	7.348	1.744	-	6.088	0.276	-	3.912
5	11	1.436	-	13.3	1.744	-	8.868	0.46	-	6.324	1.452	-	7.532	1.944	-	6.288	0.404	-	4.04
5	12	1.436	-	13.6	1.944	-	9.068	0.496	-	6.36	1.456	-	7.536	1.944	-	6.288	0.068	-	3.704
5	13	1.44	-	13.304	1.748	-	8.872	0.496	-	6.36	1.46	-	7.54	1.728	-	6.072	0.312	-	3.948
5	14	1.44	-	13.3	1.744	-	8.868	0.496	-	6.36	1.456	-	7.536	1.728	-	6.072	0.064	-	3.7
5	15	1.44	-	13.3	1.744	-	8.868	0.496	-	6.36	1.46	-	7.54	1.728	-	6.072	0.064	-	3.7
5	16	1.44	-	13.296	1.74	-	8.864	0.52	-	6.384	1.46	-	7.54	1.944	-	6.288	0.324	-	3.96
5	17	1.44	-	13.296	1.74	-	8.864	0.52	-	6.384	1.46	-	7.54	1.944	-	6.288	0.356	-	3.992
5	18	1.44	-	13.296	1.74	-	8.864	0.496	-	6.36	1.464	-	7.544	1.732	-	6.076	0.44	-	4.076
5	19	1.44	-	13.088	1.532	-	8.656	0.436	-	6.3	1.468	-	7.548	1.728	-	6.072	0.44	-	4.076
5	20	1.44	-	13.088	1.532	-	8.656	0.5	-	6.364	1.468	-	7.548	1.732	-	6.076	0.44	-	4.076
5	21	1.444	-	13.088	1.532	-	8.656	0.436	-	6.3	1.468	-	7.548	1.948	-	6.292	0.44	-	4.076
5	22	1.756	-	12.664	1.108	-	8.232	0.444	-	6.308	1.46	-	7.54	2.376	-	7.72	0.368	-	4.004
6	7	1.264	-	13.088	1.532	-	8.656	0.268	-	6.132	1.26	-	7.34	1.948	-	6.292	0.272	-	3.908
6	8	1.264	-	13.088	1.532	-	8.656	0.268	-	6.132	1.264	-	7.344	1.736	-	6.8	0.272	-	3.908

Table C.1: Used time windows for the stretching method. (cont.)

6	9	1.264	-	13.092	1.536	-	8.66	0.268	-	6.132	1.264	-	7.344	1.948	-	6.292	0.272	-	3.908
6	10	1.268	-	13.308	1.752	-	8.876	0.272	-	6.136	1.264	-	7.344	1.956	-	6.8	0.272	-	3.908
6	11	1.436	-	13.716	2.16	-	9.284	0.468	-	6.332	1.448	-	7.528	2.156	-	6.8	0.4	-	4.036
6	12	1.436	-	13.084	1.528	-	8.652	0.464	-	6.328	1.452	-	7.532	2.156	-	6.8	0.4	-	4.036
6	13	1.436	-	13.088	1.532	-	8.656	0.464	-	6.328	1.456	-	7.536	1.94	-	6.284	0.396	-	4.032
6	14	1.436	-	13.084	1.528	-	8.652	0.464	-	6.328	1.456	-	7.536	1.94	-	6.284	0.064	-	3.7
6	15	1.44	-	13.084	1.528	-	8.652	0.464	-	6.328	1.456	-	7.536	1.944	-	6.288	0.064	-	3.7
6	16	1.44	-	13.296	1.74	-	8.864	0.464	-	6.328	1.456	-	7.536	1.944	-	6.288	0.408	-	4.044
6	17	1.44	-	13.296	1.74	-	8.864	0.512	-	6.376	1.46	-	7.54	1.944	-	6.288	0.356	-	3.992
6	18	1.44	-	13.296	1.74	-	8.864	0.436	-	6.3	1.464	-	7.544	1.944	-	6.288	0.44	-	4.076
6	19	1.44	-	13.296	1.74	-	8.864	0.436	-	6.3	1.464	-	7.544	1.944	-	6.288	0.44	-	4.076
6	20	1.44	-	13.296	1.74	-	8.864	0.436	-	6.3	1.464	-	7.544	1.944	-	6.288	0.44	-	4.076
6	21	1.44	-	13.088	1.532	-	8.656	0.436	-	6.3	1.464	-	7.544	1.948	-	6.292	0.44	-	4.076
6	22	1.752	-	12.668	1.112	-	8.236	0.6	-	6.464	1.456	-	7.536	2.588	-	6.932	0.44	-	4.076
7	8	1.264	-	13.092	1.536	-	8.66	0.268	-	6.132	1.26	-	7.34	1.948	-	6.292	0.272	-	3.908
7	9	1.264	-	12.876	1.32	-	8.444	0.268	-	6.132	1.264	-	7.344	1.948	-	6.292	0.272	-	3.908
7	10	1.268	-	13.1	1.544	-	8.668	0.272	-	6.136	1.264	-	7.344	1.956	-	6.3	0.272	-	3.908
7	11	1.436	-	13.716	2.16	-	9.284	0.468	-	6.332	1.448	-	7.528	2.368	-	6.712	0.4	-	4.036
7	12	1.436	-	13.084	1.528	-	8.652	0.464	-	6.328	1.448	-	7.528	2.156	-	6.5	0.4	-	4.036
7	13	1.436	-	13.088	1.532	-	8.656	0.464	-	6.328	1.456	-	7.536	1.944	-	6.288	0.4	-	4.036
7	14	1.436	-	13.084	1.528	-	8.652	0.464	-	6.328	1.452	-	7.532	1.944	-	6.288	0.396	-	4.032
7	15	1.436	-	13.084	1.528	-	8.652	0.464	-	6.328	1.456	-	7.536	1.944	-	6.288	0.064	-	3.7
7	16	1.436	-	13.088	1.532	-	8.656	0.464	-	6.328	1.456	-	7.536	2.156	-	6.5	0.408	-	4.044
7	17	1.44	-	13.296	1.74	-	8.864	0.512	-	6.376	1.456	-	7.536	2.156	-	6.5	0.356	-	3.992
7	18	1.44	-	13.296	1.74	-	8.864	0.432	-	6.296	1.46	-	7.54	1.944	-	6.288	0.44	-	4.076
7	19	1.436	-	13.296	1.74	-	8.864	0.432	-	6.296	1.46	-	7.54	1.944	-	6.288	0.44	-	4.076
7	20	1.436	-	13.084	1.528	-	8.652	0.436	-	6.3	1.464	-	7.544	1.944	-	6.288	0.44	-	4.076
7	21	1.44	-	13.088	1.532	-	8.656	0.436	-	6.3	1.46	-	7.54	2.16	-	6.504	0.44	-	4.076
7	22	1.756	-	12.876	1.32	-	8.444	0.596	-	6.46	1.448	-	7.528	2.588	-	6.932	0.44	-	4.076
8	9	1.268	-	12.872	1.316	-	8.44	0.268	-	6.132	1.264	-	7.344	1.952	-	6.296	0.272	-	3.908
8	10	1.268	-	12.696	1.14	-	8.264	0.268	-	6.132	1.26	-	7.34	1.956	-	6.3	0.272	-	3.908
8	11	1.436	-	13.284	1.728	-	8.852	0.468	-	6.332	1.444	-	7.524	2.368	-	6.712	0.4	-	4.036
8	12	1.436	-	13.084	1.528	-	8.652	0.464	-	6.328	1.448	-	7.528	2.156	-	6.5	0.4	-	4.036
8	13	1.436	-	13.088	1.532	-	8.656	0.464	-	6.328	1.452	-	7.532	2.156	-	6.5	0.4	-	4.036
8	14	1.436	-	13.084	1.528	-	8.652	0.464	-	6.328	1.452	-	7.532	2.156	-	6.5	0.392	-	4.028
8	15	1.44	-	13.084	1.528	-	8.652	0.464	-	6.328	1.456	-	7.536	2.156	-	6.5	0.064	-	3.7
8	16	1.436	-	13.084	1.528	-	8.652	0.496	-	6.36	1.452	-	7.532	2.156	-	6.5	0.404	-	4.04
8	17	1.44	-	13.292	1.736	-	8.68	0.512	-	6.376	1.456	-	7.536	2.156	-	6.5	0.352	-	3.988
8	18	1.44	-	13.296	1.74	-	8.864	0.432	-	6.296	1.46	-	7.54	1.944	-	6.288	0.436	-	4.072
8	19	1.436	-	13.084	1.528	-	8.652	0.432	-	6.296	1.46	-	7.54	1.944	-	6.288	0.44	-	4.076
8	20	1.436	-	13.292	1.736	-	8.68	0.432	-	6.296	1.46	-	7.54	2.156	-	6.5	0.44	-	4.076
8	21	1.44	-	13.296	1.74	-	8.864	0.436	-	6.3	1.46	-	7.54	2.16	-	6.504	0.44	-	4.076
8	22	1.756	-	13.296	1.74	-	8.864	0.596	-	6.46	1.444	-	7.524	2.588	-	6.932	0.44	-	4.076
9	10	1.268	-	12.7	1.144	-	8.268	0.268	-	6.132	1.26	-	7.34	2.164	-	6.508	0.272	-	3.908
9	11	1.104	-	13.088	1.532	-	8.656	0.468	-	6.332	1.444	-	7.524	2.148	-	6.492	0.4	-	4.036
9	12	1.432	-	13.084	1.528	-	8.652	0.464	-	6.328	1.444	-	7.524	2.156	-	6.5	0.396	-	4.032
9	13	1.436	-	13.084	1.528	-	8.652	0.464	-	6.328	1.452	-	7.532	2.152	-	6.496	0.4	-	4.036
9	14	1.432	-	13.084	1.528	-	8.652	0.464	-	6.328	1.448	-	7.528	2.152	-	6.496	0.392	-	4.028
9	15	1.436	-	13.084	1.528	-	8.652	0.464	-	6.328	1.452	-	7.532	2.156	-	6.5	0.392	-	4.028
9	16	1.436	-	13.084	1.528	-	8.652	0.464	-	6.328	1.452	-	7.532	2.156	-	6.5	0.404	-	4.04
9	17	1.436	-	13.292	1.736	-	8.68	0.512	-	6.376	1.452	-	7.532	2.156	-	6.5	0.352	-	3.988
9	18	1.436	-	13.292	1.736	-	8.68	0.432	-	6.296	1.456	-	7.536	2.156	-	6.5	0.436	-	4.072
9	19	1.436	-	13.292	1.736	-	8.68	0.432	-	6.296	1.46	-	7.54	2.156	-	6.5	0.436	-	4.072
9	20	1.436	-	13.292	1.736	-	8.68	0.432	-	6.296	1.46	-	7.54	2.156	-	6.5	0.44	-	4.076
9	21	1.436	-	12.88	1.324	-	8.448	0.436	-	6.3	1.456	-	7.536	2.16	-	6.504	0.44	-	4.076
9	22	1.632	-	13.292	1.736	-	8.68	0.6	-	6.464	1.44	-	7.52	1.928	-	6.272	0.436	-	4.072
10	11	1.1	-	12.848	1.292	-	8.416	0.468	-	6.332	1.444	-	7.524	1.724	-	6.068	0.396	-	4.032
10	12	1.432	-	13.084	1.528	-	8.652	0.464	-	6.328	1.448	-	7.528	2.364	-	6.708	0.396	-	4.032
10	13	1.432	-	13.8	1.524	-	8.648	0.464	-	6.328	1.452	-	7.532	1.724	-	6.068	0.4	-	4.036
10	14	1.432	-	13.8	1.524	-	8.648	0.464	-	6.328	1.448	-	7.528	1.724	-	6.068	0.392	-	4.028
10	15	1.432	-	13.708	2.152	-	9.276	0.464	-	6.328	1.452	-	7.532	1.724	-	6.068	0.064	-	3.7
10	16	1.432	-	13.92	2.364	-	9.488	0.464	-	6.328	1.452	-	7.532	1.728	-	6.072	0.404	-	4.04

Table C.1: Used time windows for the stretching method. (cont.)

10	17	1.432	-	13.92	2.364	-	9.488	0.512	-	6.376	1.452	-	7.532	2.152	-	6.496	0.352	-	3.988
10	18	1.432	-	13.496	1.94	-	9.064	0.504	-	6.368	1.456	-	7.536	1.94	-	6.284	0.356	-	3.992
10	19	1.432	-	13.496	1.94	-	9.064	0.5	-	6.364	1.46	-	7.54	1.936	-	6.28	0.436	-	4.072
10	20	1.432	-	13.496	1.94	-	9.064	0.5	-	6.364	1.46	-	7.54	2.152	-	6.496	0.436	-	4.072
10	21	1.432	-	12.876	1.32	-	8.444	0.504	-	6.368	1.46	-	7.54	1.94	-	6.284	0.44	-	4.076
10	22	1.628	-	12.892	1.336	-	8.46	0.596	-	6.46	1.448	-	7.528	2.156	-	6.5	0.436	-	4.072
11	12	1.264	-	12.7	1.144	-	8.268	0.268	-	6.132	1.264	-	7.344	1.304	-	5.648	0.268	-	3.904
11	13	1.264	-	12.864	1.308	-	8.432	0.268	-	6.132	1.268	-	7.348	1.124	-	5.468	0.272	-	3.908
11	14	1.264	-	12.864	1.308	-	8.432	0.268	-	6.132	1.264	-	7.344	1.124	-	5.468	0.272	-	3.908
11	15	1.264	-	13.504	1.948	-	9.072	0.268	-	6.132	1.268	-	7.348	1.124	-	5.468	0.272	-	3.908
11	16	1.264	-	13.508	1.952	-	9.076	0.268	-	6.132	1.264	-	7.344	1.528	-	5.872	0.272	-	3.908
11	17	1.264	-	12.656	1.1	-	8.224	0.232	-	6.096	1.268	-	7.348	1.528	-	5.872	0.228	-	3.864
11	18	1.264	-	12.656	1.1	-	8.224	0.232	-	6.096	1.272	-	7.352	1.524	-	5.868	0.228	-	3.864
11	19	1.26	-	13.292	1.736	-	8.68	0.232	-	6.096	1.276	-	7.356	1.52	-	5.864	0.308	-	3.944
11	20	1.264	-	13.292	1.736	-	8.68	0.232	-	6.096	1.276	-	7.356	1.524	-	5.868	0.308	-	3.944
11	21	1.264	-	13.296	1.74	-	8.864	0.3	-	6.164	1.272	-	7.352	1.74	-	6.084	0.312	-	3.948
11	22	1.272	-	12.752	1.196	-	8.32	0.396	-	6.26	1.256	-	7.336	1.332	-	5.676	0.308	-	3.944
12	13	1.264	-	12.872	1.316	-	8.32	0.268	-	6.132	1.264	-	7.344	1.524	-	5.868	0.272	-	3.908
12	14	1.264	-	12.872	1.316	-	8.44	0.268	-	6.132	1.264	-	7.344	1.524	-	5.868	0.272	-	3.908
12	15	1.264	-	12.876	1.32	-	8.444	0.268	-	6.132	1.264	-	7.344	1.524	-	5.868	0.272	-	3.908
12	16	1.264	-	13.088	1.532	-	8.656	0.268	-	6.132	1.264	-	7.344	1.528	-	5.872	0.272	-	3.908
12	17	1.264	-	13.088	1.532	-	8.656	0.376	-	6.24	1.264	-	7.344	1.528	-	5.872	0.228	-	3.864
12	18	1.264	-	13.508	1.952	-	9.076	0.232	-	6.096	1.268	-	7.348	1.524	-	5.868	0.232	-	3.868
12	19	1.264	-	13.508	1.952	-	9.076	0.232	-	6.096	1.268	-	7.348	1.524	-	5.868	0.232	-	3.868
12	20	1.264	-	13.088	1.532	-	8.656	0.232	-	6.096	1.272	-	7.352	1.524	-	5.868	0.232	-	3.868
12	21	1.264	-	13.296	1.74	-	8.864	0.232	-	6.096	1.268	-	7.348	1.74	-	6.084	0.312	-	3.948
12	22	1.276	-	12.908	1.352	-	8.476	0.4	-	6.264	1.256	-	7.336	1.956	-	6.3	0.308	-	3.944
13	14	1.26	-	12.876	1.32	-	8.444	0.268	-	6.132	1.26	-	7.34	1.528	-	5.872	0.268	-	3.904
13	15	1.264	-	13.088	1.532	-	8.656	0.268	-	6.132	1.26	-	7.34	1.532	-	5.876	0.272	-	3.908
13	16	1.264	-	13.088	1.532	-	8.656	0.268	-	6.132	1.26	-	7.34	1.948	-	6.292	0.272	-	3.908
13	17	1.264	-	13.088	1.532	-	8.656	0.436	-	6.1	1.26	-	7.34	1.952	-	6.296	0.228	-	3.864
13	18	1.264	-	13.508	1.952	-	9.076	0.232	-	6.096	1.264	-	7.344	1.528	-	5.872	0.228	-	3.864
13	19	1.26	-	13.508	1.952	-	9.076	0.232	-	6.096	1.264	-	7.344	1.528	-	5.872	0.228	-	3.864
13	20	1.26	-	13.088	1.532	-	8.656	0.232	-	6.096	1.264	-	7.344	1.532	-	5.876	0.232	-	3.868
13	21	1.264	-	13.296	1.72	-	8.864	0.232	-	6.096	1.264	-	7.344	1.744	-	6.088	0.308	-	3.944
13	22	1.276	-	12.632	1.076	-	8.2	0.396	-	6.26	1.916	-	7.996	1.744	-	6.088	0.308	-	3.944
14	15	1.264	-	13.088	1.532	-	8.656	0.268	-	6.132	1.26	-	7.34	1.74	-	6.084	0.272	-	3.908
14	16	1.264	-	13.088	1.532	-	8.656	0.268	-	6.132	1.26	-	7.34	1.952	-	6.296	0.272	-	3.908
14	17	1.264	-	13.088	1.532	-	8.656	0.448	-	6.312	1.26	-	7.34	1.952	-	6.296	0.552	-	4.188
14	18	1.264	-	13.088	1.532	-	8.656	0.232	-	6.096	1.264	-	7.344	1.74	-	6.084	0.308	-	3.944
14	19	1.264	-	13.088	1.532	-	8.656	0.232	-	6.096	1.264	-	7.344	1.74	-	6.084	0.308	-	3.944
14	20	1.264	-	13.088	1.532	-	8.656	0.232	-	6.096	1.264	-	7.344	1.74	-	6.084	0.308	-	3.944
14	21	1.264	-	13.092	1.536	-	8.66	0.236	-	6.1	1.264	-	7.344	1.744	-	6.088	0.308	-	3.944
14	22	1.276	-	12.636	1.8	-	8.204	0.4	-	6.264	1.916	-	7.996	2.384	-	6.728	0.308	-	3.944
15	16	1.26	-	13.088	1.532	-	8.656	0.268	-	6.132	1.256	-	7.336	1.948	-	6.292	0.272	-	3.908
15	17	1.26	-	13.088	1.532	-	8.656	0.448	-	6.312	1.256	-	7.336	1.948	-	6.292	0.56	-	4.196
15	18	1.264	-	13.088	1.532	-	8.656	0.56	-	6.424	1.26	-	7.34	1.528	-	5.872	0.308	-	3.944
15	19	1.26	-	13.088	1.532	-	8.656	0.236	-	6.1	1.26	-	7.34	1.736	-	6.8	0.308	-	3.944
15	20	1.26	-	13.088	1.532	-	8.656	0.236	-	6.1	1.26	-	7.34	1.74	-	6.084	0.308	-	3.944
15	21	1.264	-	13.088	1.532	-	8.656	0.236	-	6.1	1.26	-	7.34	1.74	-	6.084	0.308	-	3.944
15	22	1.276	-	12.64	1.084	-	8.208	0.4	-	6.264	1.916	-	7.996	2.38	-	6.724	0.304	-	3.94
16	17	1.26	-	13.088	1.532	-	8.656	0.556	-	6.42	1.256	-	7.336	1.528	-	5.872	0.56	-	4.196
16	18	1.264	-	13.088	1.532	-	8.656	0.448	-	6.312	1.26	-	7.34	1.524	-	5.868	0.304	-	3.94
16	19	1.26	-	13.088	1.532	-	8.656	0.344	-	6.208	1.264	-	7.344	1.524	-	5.868	0.304	-	3.94
16	20	1.264	-	13.088	1.532	-	8.656	0.344	-	6.208	1.264	-	7.344	1.736	-	6.8	0.304	-	3.94
16	21	1.264	-	13.088	1.532	-	8.656	0.344	-	6.208	1.26	-	7.34	1.74	-	6.084	0.304	-	3.94
16	22	1.28	-	12.648	1.092	-	8.216	0.396	-	6.24	1.248	-	7.328	2.38	-	6.724	0.304	-	3.94
17	18	1.26	-	13.088	1.532	-	8.656	0.268	-	6.132	1.26	-	7.34	1.524	-	5.868	0.272	-	3.908
17	19	1.26	-	13.088	1.532	-	8.656	0.268	-	6.132	1.26	-	7.34	1.524	-	5.868	0.272	-	3.908
17	20	1.26	-	13.088	1.532	-	8.656	0.268	-	6.132	1.26	-	7.34	1.736	-	6.8	0.272	-	3.908
17	21	1.264	-	13.088	1.532	-	8.656	0.272	-	6.136	1.26	-	7.34	1.74	-	6.084	0.272	-	3.908
17	22	1.28	-	12.652	1.096	-	8.22	0.44	-	6.304	1.248	-	7.328	2.38	-	6.724	0.272	-	3.908

Table C.1: Used time windows for the stretching method. (cont.)

18	19	1.26	-	13.088	1.532	-	8.656	0.268	-	6.132	1.256	-	7.336	1.736	-	6.8	0.272	-	3.908
18	20	1.26	-	13.088	1.532	-	8.656	0.268	-	6.132	1.256	-	7.336	1.736	-	6.8	0.272	-	3.908
18	21	1.264	-	13.088	1.532	-	8.656	0.268	-	6.132	1.256	-	7.336	1.952	-	6.296	0.272	-	3.908
18	22	1.276	-	12.668	1.112	-	8.236	0.44	-	6.304	1.92	-	8.0	2.38	-	6.724	0.268	-	3.904
19	20	1.264	-	13.088	1.532	-	8.656	0.268	-	6.132	1.256	-	7.336	1.952	-	6.296	0.272	-	3.908
19	21	1.264	-	13.092	1.536	-	8.66	0.268	-	6.132	1.256	-	7.336	1.952	-	6.296	0.272	-	3.908
19	22	1.276	-	12.68	1.124	-	8.248	0.36	-	6.224	1.92	-	8.0	2.38	-	6.724	0.268	-	3.904
20	21	1.264	-	13.092	1.536	-	8.66	0.268	-	6.132	1.256	-	7.336	1.952	-	6.296	0.268	-	3.908
20	22	1.272	-	12.692	1.136	-	8.26	0.348	-	6.212	1.912	-	7.992	2.38	-	6.724	0.348	-	3.904
21	22	1.268	-	12.7	1.144	-	8.268	0.348	-	6.212	1.236	-	7.316	2.164	-	6.508	0.348	-	3.904

Table C.1: Used time windows for the stretching method. (cont.)

D Stretching results of the long term measurements

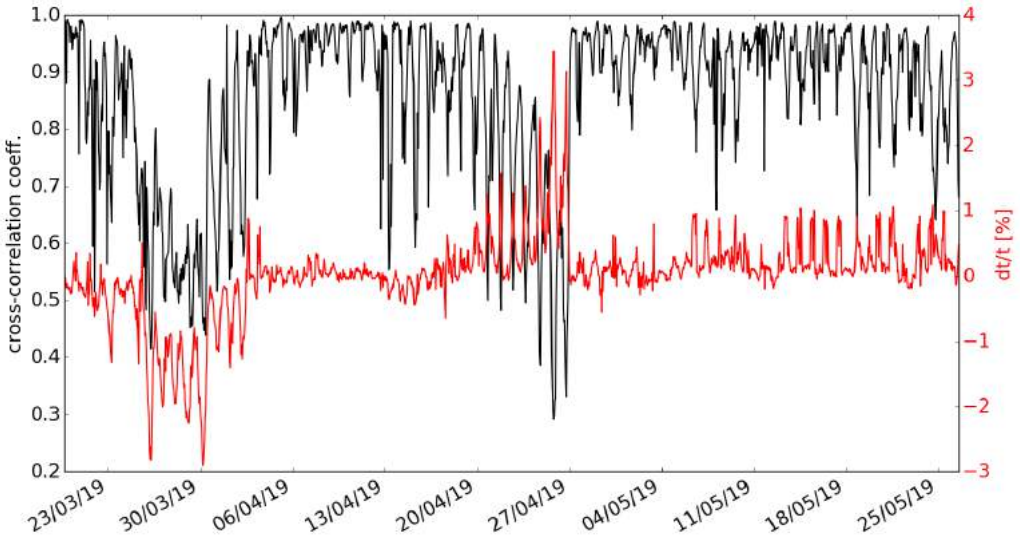

Figure D.1: Travel time variations and belonging cross-correlation coefficients (4.5 – 8 Hz).

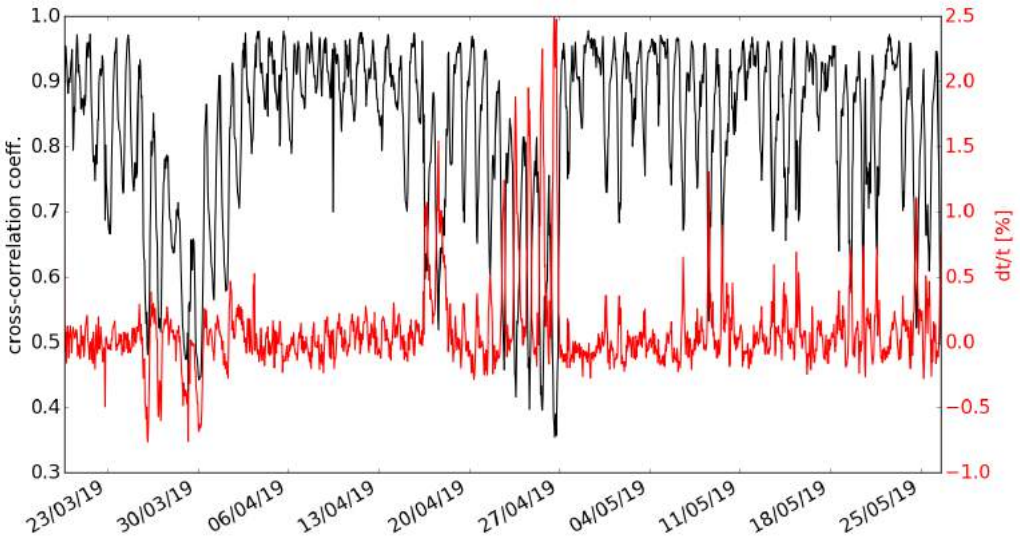

Figure D.2: Travel time variations and belonging cross-correlation coefficients (12 – 16 Hz).

References

Keiiti Aki and Bernard Chouet. Origin of coda waves: Source, attenuation, and scattering effects. *Journal of Geophysical Research*, 80(23):3322–3342, Oct 1975. doi: 10.1029/jb080i023p03322.

Ali Al-Ghalib and Fouad Mohammad. The use of modal parameters in structural health monitoring. *MATEC Web Conf.*, 162:04020, 2018. doi: 10.1051/matecconf/201816204020. URL https://doi.org/10.1051/matecconf/201816204020.

BaSt. Brückenstatistik 2019 - Brücken an Fernstraßen, September 2019. URL https://www.bast.de/BASt_2017/DE/Statistik/Bruecken/Brueckenstatistik.pdf?__blob=publicationFile\&v=13. Accessed on 2020-01-27.

G. D. Bensen, M. H. Ritzwoller, M. P. Barmin, A. L. Levshin, F. Lin, M. P. Moschetti, N. M. Shapiro, and Y. Yang. Processing seismic ambient noise data to obtain reliable broad-band surface wave dispersion measurements. *Geophysical Journal International*, 169(3):1239–1260, 2007. doi: 10.1111/j.1365-246x.2007.03374.x.

Marco Breccolotti. On the evaluation of prestress loss in prc beams by means of dynamic techniques. *International Journal of Concrete Structures and Materials*, 12(1):1, Jan 2018. ISSN 2234-1315. doi: 10.1186/s40069-018-0237-8. URL https://doi.org/10.1186/s40069-018-0237-8.

Paul Cupillard, Laurent Stehly, and Barbara Romanowicz. The one-bit noise correlation: a theory based on the concepts of coherent and incoherent noise. *Geophysical Journal International*, 184(3):1397–1414, 03 2011. ISSN 0956-540X. doi: 10.1111/j.1365-246X.2010.04923.x. URL https://doi.org/10.1111/j.1365-246X.2010.04923.x.

Spilios D. Fassois and Fotis P. Kopsaftopoulos. *Statistical Time Series Methods for Vibration Based Structural Health Monitoring*, pages 209–264. Springer Vienna, Vienna, 2013. ISBN 978-3-7091-1390-5. doi: 10.1007/978-3-7091-1390-5_4. URL https://doi.org/10.1007/978-3-7091-1390-5_4.

Celine Hadziioannou, Eric Larose, Coutant Olivier, Roux Philippe, and Campillo Michel. Stability of monitoring weak changes in multiply scattering media with ambient noise correlation: Laboratory experiments. *The Journal of the Acoustical Society of America*, 125(4):2654–2654, 2009. doi: 10.1121/1.4784159.

Matthew Haney, Kasper Wijk, Leiph Preston, and David Aldridge. Observation and modeling of source effects in coda wave interferometry at pavlof volcano. *Kasper van Wijk*, 28, 05 2009. doi: 10.1190/1.3124930.

Miguel Herraiz and A. Espinosa. Coda waves: A review. *Pure and Applied Geophysics*, 125:499–577, 07 1987. doi: 10.1007/BF00879572.

Byungmo Kim, Cheonhong Min, Hyungwoo Kim, Sugil Cho, Jaewon Oh, Seung-Hyun Ha, and Jin-hak Yi. Structural health monitoring with sensor data and cosine similarity for multi-damages. *Sensors*, 19(14):3047, Jul 2019. ISSN 1424-8220. doi: 10.3390/s19143047. URL http://dx.doi.org/10.3390/s19143047.

Eric Larose, Derode Arnaud, Michel Campillo, and Mathias Fink. Imaging from one-bit correlation of wide-band diffuse wavefield. *Journal of Applied Physics - J APPL PHYS*, 95, 06 2004. doi: 10.1063/1.1739529.

Eric Larose, Julien Rosny, Ludovic Margerin, Domitille Anache, Pierre Gouédard, Michel Campillo, and Bart Tiggelen. Observation of multiple scattering of khz vibrations in a concrete structure and application to monitoring weak changes. *Physical review. E, Statistical, nonlinear, and soft matter physics*, 73:016609, 02 2006. doi: 10.1103/PhysRevE.73.016609.

Le Li, Fenglin Niu, Qi-Fu Chen, Jinrong Su, and Jiabin He. Post-seismic velocity changes along the 2008 M7.9 Wenchuan earthquake rupture zone revealed by S coda of repeating events. *Geophysical Journal International*, 208(2):1237–1249, 12 2016. ISSN 0956-540X. doi: 10.1093/gji/ggw454. URL https://doi.org/10.1093/gji/ggw454.

Zhikun Liu, Jinli Huang, and Jiaojiao Li. Comparison of four techniques for estimating temporal change of seismic velocity with passive image interferometry. *Earthquake Science*, 23(5):511–518, 2010. doi: 10.1007/s11589-010-0749-z.

Oleg I. Lobkis and Richard L. Weaver. Coda-wave interferometry in finite solids: Recovery of *p*-to-*s* conversion rates in an elastodynamic billiard. *Phys. Rev. Lett.*, 90: 254302, Jun 2003. doi: 10.1103/PhysRevLett.90.254302. URL https://link.aps.org/doi/10.1103/PhysRevLett.90.254302.

Lorenz Marten. Use of vehicle induced vibrations for structural health monitoring on bridges. Master's thesis, University of Hamburg, 2019.

Vivien Mierschke. Untersuchung der Anwendbarkeit passiver Seismik für das Brückenmonitoring. Master's thesis, Technische Universität Berlin, 6 2018.

T. Dylan Mikesell, Alison E. Malcolm, Di Yang, and Matthew M. Haney. A comparison of methods to estimate seismic phase delays: numerical examples for coda wave interferometry. *Geophysical Journal International*, 202(1):347–360, 04 2015. ISSN 0956-540X. doi: 10.1093/gji/ggv138. URL https://doi.org/10.1093/gji/ggv138.

E. Niederleithinger and C. Wunderlich. Influence of small temperature variations on the ultrasonic velocity in concrete. *AIP Conference Proceedings*, 1511(1):390–397, 2013. doi: 10.1063/1.4789074. URL https://aip.scitation.org/doi/abs/10.1063/1.4789074.

N. Rajagoplan. *Prestressed Concrete*. Alpha Science International Ltd., 2003. ISBN 1842650734.

Johannes Salvermoser. Non-destructive testing of a civil structure using seismic signals. Master's thesis, Ludwig-Maximilians-University Munich, 8 2014.

C. Sens-Schönfelder and U. Wegler. Passive image interferometry and seasonal variations of seismic velocities at Merapi Volcano, Indonesia. *Geophysical Research Letters*, 33 (21), Jan 2006. doi: 10.1029/2006gl027797.

N. M. Shapiro and M. Campillo. Emergence of broadband rayleigh waves from correlations of the ambient seismic noise. *Geophysical Research Letters*, 31(7), 2004. doi: 10.1029/2004GL019491. URL https://agupubs.onlinelibrary.wiley.com/doi/abs/10.1029/2004GL019491.

Peter M. Shearer. *Introduction to Seismology*. Cambridge University Press, 2 edition, 2009. doi: 10.1017/CBO9780511841552.

Roel Snieder. Coda wave interferometry and the equilibration of energy in elastic media. *Phys. Rev. E*, 66:046615, Oct 2002. doi: 10.1103/PhysRevE.66.046615. URL https://link.aps.org/doi/10.1103/PhysRevE.66.046615.

Roel Snieder. The Theory of Coda Wave Interferometry. *Pure and Applied Geophysics*, 163(2-3):455–473, Aug 2006. doi: 10.1007/s00024-005-0026-6.

S. Sritharan and R. C. Fenwick. Creep and shrinkage effects in prestressed beams. *Magazine of Concrete Research*, 47(170):45–55, 1995. doi: 10.1680/macr.1995.47.170.45.

Simon Stähler, Christoph Sens-Schönfelder, and Ernst Niederleithinger. Monitoring stress changes in a concrete bridge with coda wave interferometry. *The Journal of the Acoustical Society of America*, 129:1945–52, 04 2011. doi: 10.1121/1.3553226.

Kees Wapenaar, Deyan Draganov, Roel Snieder, Xander Campman, and Arie Verdel. Tutorial on seismic interferometry: Part 1 — Basic principles and applicationsTutorial on interferometry: Part 1. *Geophysics*, 75(5):75A195–75A209, 09 2010. ISSN 0016-8033. doi: 10.1190/1.3457445. URL https://doi.org/10.1190/1.3457445.

Zhongwen Zhan, Victor C. Tsai, and Robert W. Clayton. Spurious velocity changes caused by temporal variations in ambient noise frequency content. *Geophysical Journal International*, 194(3):1574–1581, 05 2013. ISSN 0956-540X. doi: 10.1093/gji/ggt170. URL https://doi.org/10.1093/gji/ggt170.

Acknowledgments

I want to thank my supervisors, Prof. Dr. Céline Hadziioannou and PD Dr. rer. nat. Ernst Niederleithinger, for the support, advice and guidance they have given to me all this time.

I also would like to thank the BAM for making the measurement at the BLEIB-structure on their testing site possible. In particular, I would like to thank everyone who supported me during the measurement on site, be it the setup, the monitoring or the dismantling. It was a great help!

The seismological working group and my friends shall not remain unmentioned here. I want to thank them for the helpful criticism, the discussions and in particular the support when something did not work the way it should.

Finally, I want to thank my family for all their love and support in all the years of study.

Versicherung an Eides statt

Hiermit versichere ich an Eides statt, dass ich die vorliegende Arbeit im Studiengang M.Sc. Geophysik selbstständig verfasst und keine anderen als die angegebenen Hilfsmittel – insbesondere keine im Quellenverzeichnis nicht benannten Internet-Quellen – benutzt habe. Alle Stellen, die wörtlich oder sinngemäß aus Veröffentlichungen entnommen wurden, sind als solche kenntlich gemacht. Ich versichere weiterhin, dass ich die Arbeit vorher nicht in einem anderen Prüfungsverfahren eingereicht habe und die eingereichte schriftliche Fassung der auf dem elektronischen Speichermedium entspricht. Ich bin mit einer Veröffentlichung der Arbeit einverstanden.

Datum, Ort

Franziska Mehrkens